

Behavior of photocarrier in atomically thin two-dimensional
semiconducting materials for optoelectronics

by

Daichi Kozawa

© Copyright by Daichi Kozawa 2015
All Rights Reserved

Abstract

Behavior of photocarrier in atomically thin two-dimensional semiconducting materials
for optoelectronics
by
Daichi Kozawa

Advisor: Professor Kazunari Matsuda

Atomically thin two-dimensional semiconducting materials are new class of materials that can overcome the scaling limitation. The excellent optoelectronic properties of the materials have a large impact on recent nanotechnology. The extreme geometrical confinement and weak dielectric screening give the materials unique electronic and optical properties. The flexibility due to the atomically thin and elastic structure enables next generation of optoelectronics meeting the demand for wearable devices and other numerous applications.

Optoelectronic devices are now at a turning point since burgeoning demands of wearable devices has appeared, which is a new way to manage information using flexible light emitting diode and photovoltaic cell. In this technological phase, the key factor is their portability to be integrated in to everyday life not only a quest for their performance. This class of devices requires mechanical flexibility in the implemented materials. Nevertheless, conventional inorganic bulk materials are rigid and do not allow their implementation to the flexible devices. The concept of flexible optoelectronic device has a strong affinity with the atomically thin two-dimensional (2D) materials especially graphene oxide (GO) and transition metal dichalcogenides (TMDs) because of the good mechanical, electrical, optical properties and also solution-processability.

In optoelectronic devices, incident light controls carrier-transporting properties or electric field effect controls optical properties of the materials. The key factor is light-mater interaction to determine the nature of photoelectric conversion since

photoexcited carrier generation and excitation are the major process in the conversion. Understanding the static and transient behavior of the photocarriers will provide guiding principle of architectures of materials and devices. In this thesis, we focus on light-matter interaction in GO and 2D semiconducting TMDs. Both of the materials show the extraordinarily strong light absorption despite being atomically thin. TMDs can absorb sunlight as high as 5-10%, while graphene can absorb 2.3% light which is considered to be the comparable level to GO. The strong-light matter interaction provides these materials advantages for efficient optical response. It should be noted that these two materials possess contrasting properties in their tunability of optical properties. GO has excellent tunability of optical gap in a wide range by chemical modification of its structures, while TMDs have rigid optical gap. While the expected technological impacts of GO and TMDs are significant, the lack of accumulated knowledge associated with their photocarrier behavior is one of obstacles for their application. A challenge is clarifying the size-dependency of the optically active domains in GO on the luminescent properties. Also another challenge is investigating the behavior of photo-excited carriers with high energy far from the band edge of TMDs. The study in this thesis mainly deals with how photocarrier is generated and relaxed in the 2D materials. Investigation of the photocarrier behavior in the materials leads to major progress to achieve a new class of light-harvesting and -emitting devices.

The results based on static photoluminescence (PL) excitation spectroscopy, time-resolved PL spectroscopy, and first principle calculations reveal the behavior of photoexcited carriers in GO and TMDs. The behavior of photocarriers in GO is found to be determined by a zero-dimensional property within graphene nanodisc (GND) states. Smaller GND states that consist of a few aromatic rings behave like isolated molecules (or quasi-molecular states), while larger GND states with a diameter of sub-nanometer to a few nanometer behave like quantum dots with many body effects among carriers. In the larger GND states, a characteristic photocarrier dynamics has been revealed. Energy transfers among the GND states is found to be the major relation process and can cause decrease the luminescent efficiency. On the other hand, the behavior of photocarriers in TMDs is found to be determined by a two-dimensional property related with the energy band structure. Light absorption is enhanced in particular energy range because of the characteristic band structure called “band nesting”. We unravel the photocarrier

relaxation pathways, which is generated by a higher energy excitation corresponding to the band nesting. The photoexcited electron-hole pairs in the nesting region spontaneously separate in momentum space, relaxing towards immediate band extrema with opposite momentum. Another finding is an efficient hot carrier generation accompanied with the higher energy excitation in the nesting. The findings of characteristic photocarrier behaviors of GO and TMDs will provide a guideline for designing light-emitting and light-harvesting devices as well as progress of understanding fundamental optical properties of the atomically thin two-dimensional semiconductors.

Acknowledgements

First and foremost, I would like to express the deepest appreciation to my advisor, Professor Kazunari Matsuda, for his guidance and support during my PhD thesis research. He has allowed me to learn, make mistakes and develop the research. Without his supervision and constant help, this thesis would not have been possible. I also thank him for letting me study in Singapore. He has a great patience with that his project did not develop during my stay in Singapore.

It is a pressure to express my gratitude to Professor Goki Eda, another advisor when I stayed in National University of Singapore. I truly feel lucky to work with him. He has provided a great insight for the material sciences due to his scientific creativity and leadership. He had an especially large impact on my carrier.

I enjoyed exciting collaboration and discussion with Professors. Antonio H. Castro Neto, Ricardo M. Ribeiro, Drs. Alexandra Carvalho, Weijie Zhao, Minglin Toh and Ivan Verzhbitskiy from National University of Singapore, Professor Haibin Su and Dr. Zhu Xi from Nanyang Technological University, Professor Masao Ichida from Konan University. Rajeev Kumar made significant contributions to this thesis from National University of Singapore with his great patience and passion for science. Thanks to the member of Prof. Eda's group, I really enjoyed my stay in Singapore

I would also like exhibit a feeling of thankfulness for all of the current and former members of the group for all the help and having precious time with them. Professor Yuhei Miyauchi for sharing his great knowledge and insight into physics and nano-carbon materials. Dr. Shinichiro Mouri taught me sincere attitude towards science. I have had the pleasure to work with the students, Feijiu Wang, Munechiyo Iwamura, Naoto Fuyuno, Naoto Akizuki, Lizhong Zhou, Yuka Tsuboi, Yasunori Ogawa, Shun Aota, Takashi Nakamura, co-worker Mr. Kazushi Hiraoka, the member of Prof. Hinoki's group member and a new colleague, Dr. Koirala Sandhaya. Shiori Fujiwara and Reine Sakamoto kindly took care of administrative procedures with care.

I acknowledge Global COE program from Kyoto University and a research grant from Tokyo Institute of Technology for the financial support.

Finally, I would like to express my appreciation for my family for all their love and encouragement.

Daichi Kozawa

小澤 大知

Table of contents

Abstract	i
Acknowledgements	iv
Table of contents	vi
List of tables	ix
List of figures	ix
Chapter 1. Introduction	1
1.1. Background	1
1.2. Motivation	4
1.3. Chapter outline	5
Chapter 2. Fundamental properties of atomically thin layers	7
2.1. Quantum confinement of electrons	7
2.2. Atomic structures	9
2.2.1. Graphene and chemically derived graphene	9
2.2.2. Transition metal dichalcogenides.....	14
2.3. Fundamental electronic structures	16
2.3.1. Graphene and chemically derived graphene	16
2.3.2. Transition metal dichalcogenides.....	19
2.4. Theory of optical transitions.....	22
2.4.1. Optical transitions	22
2.4.2. Molecule.....	24
2.4.3. Semiconductors	25
2.5. Fundamental optical properties of atomically thin layers.....	29
2.5.1. Graphene and chemically derived graphene	29
2.5.2. Transition metal dichalcogenides.....	33
2.6. Fundamental electrical properties of atomically thin layers	35
2.6.1. Graphene and chemically derived graphene	35
2.6.2. Transition metal dichalcogenides.....	39
Chapter 3. Quasi-molecular blue and ultraviolet photoluminescence graphene	

oxide	41
3.1. Introduction	41
3.2. Sample preparations	43
3.3. Experimental methods	44
3.3.1. Light absorption measurements	44
3.3.2. PL and PLE measurements	45
3.3.3. Raman measurements.....	46
3.3.4. Time-resolved PL measurements	47
3.3.5. AFM measurements	47
3.4. Sample characterization	48
3.5. Observation of blue and UV PL	51
3.6. pH-dependent PL properties	55
3.7. Comparison with molecular fluorescent species	57
3.8. Oxidation level of the PL centers	61
3.9. PL lifetime of the PL centers	62
3.10. Chapter summary	64
Chapter 4. Excitonic photoluminescence from nanodisc states in graphene oxide	
65	
4.1. Introduction	65
4.2. Sample preparation	67
4.3. Experimental methods	68
4.4. Theoretical calculation methods	71
4.5. Optical transitions in the graphene nanodisc states	71
4.5.1. Typical PLE properties.....	71
4.5.2. Morphology	73
4.5.3. Calculation of optical transition energy	76
4.5.4. Effect of reduction.....	79
4.6. Dynamics of the carriers in the nanodisc states	81
4.6.1. Time-resolved PL measurements	81
4.6.2. Quantum dots array model	82
4.6.3. A numerical simulation for the energy transfer	84
4.7. The effect of protonation and deprotonation	86

4.7.1. PLE properties.....	86
4.7.2. Calculation of the protonation and deprotonation effects	88
4.8. Chapter summary.....	91
Chapter 5. Photocarrier relaxation pathway in two-dimensional semiconducting transition metal dichalcogenides	92
5.1. Introduction	92
5.2. Sample preparation	94
5.3. Optical measurements.....	95
5.4. Theoretical calculations	97
5.5. Characterization of the samples	98
5.6. Band nesting and optical response.....	101
5.7. Strong light absorption	104
5.8. Excitation power-dependent PL properties of monolayer WSe ₂	106
5.9. Effect of band nesting.....	107
5.10. Comparison of photoluminescence excitation properties with preparation methods.....	112
5.11. Carrier relaxation pathway.....	115
5.11.1. Energy landscape	115
5.11.2. Monte-Carlo simulation of photocarrier relaxation	119
5.12. Discussion on the relaxation pathways.....	122
5.13. Effective collection of hot carriers.....	124
5.14. Chapter summary	124
Chapter 6. Conclusions and outlook.....	126
6.1. Summary	126
6.2. Future outlook.....	128
Bibliography.....	131
Scientific contributions.....	147
Peer-reviewed articles.....	147
Review article	148
Conference contributions	148
International conference	148

Local conference.....	149
Awards	151
Appendix.....	153
Dynamics of photocarrier in MoS₂.....	153

List of tables

Table 5.1 Analytic behavior and schematic representation of JDOS near critical points for the 2D system.....	103
--	-----

List of figures

Figure 1.1 Electronic tip and schematic structure of graphene. Graphene oxide thin films on a plastic substrate.....	1
Figure 1.2 Structure of sp ² carbon allotropes; fullerene, carbon nanotube, and graphene.....	2
Figure 2.1 Schematic structures and DOS of bulk crystals, quantum wells, wires and dots.....	9
Figure 2.2 Honeycomb lattice of graphene. The Brillouin zone of graphene	10
Figure 2.3 Crystal structure of AB and AC stacking bilayer and trilayer graphene.	11
Figure 2.4 Chemical structure of GO sheet	13
Figure 2.5 Schematics of the structural polytypes for 2H, 3R and 1T phase.....	15
Figure 2.6 Side and top views of atomic structure of 2H-MoS ₂ with hexagonal lattice	16
Figure 2.7 The σ and π orbitals of carbon atom in sp ² honeycomb lattice	17
Figure 2.8 Energy dispersion for the π and π^* bands in graphene.....	18
Figure 2.9 Schematic illustration of hybridization of d and p orbitals in MX ₂	20
Figure 2.10 Band structures of bulk, quadrilayer, bilayer, and monolayer MoS ₂ ..	21

Figure 2.11 Brillouin zone of monolayer MX_2	22
Figure 2.12 Schematic illustration of absorption and luminescence process	23
Figure 2.13 Chemical structure, uncombined 2p orbitals and π orbitals of benzene molecule.....	25
Figure 2.14 Generation of an electron-hole pair accompanied with optical transition between valence and conduction bands of typical semiconductors	26
Figure 2.15 Schematic real-space image of electron and hole bound into excitons for the 3D bulk and 2D monolayer TMDs MX_2	28
Figure 2.16 DOS per unit cell as a function of energy	29
Figure 2.17 Absorption spectra of graphene	31
Figure 2.18 PLE intensity maps for GO	32
Figure 2.19 Band structure and DOS of monolayer MoS_2	33
Figure 2.20 PL spectra for monolayer and bilayer MoS_2	35
Figure 2.21 Scanning electron microscope image of graphene devices on a SiO_2/Si substrate.....	36
Figure 2.22 Photograph of thin film transistor device based on GO.....	37
Figure 2.23 Conductivity of thermally reduced GO as a function of sp^2 carbon fraction.....	38
Figure 2.24 Drain-source current of monolayer MoS_2 device as a function of gate voltage measured at room temperature with the back gate grounded	40
Figure 3.1 Schematic image of quasi-molecular luminescence species.....	42
Figure 3.2 Chemical structural formula and photographs of salicylic acid, phthalic acid, phenol, benzoic acid, and 1-naphthoic acid	43
Figure 3.3 Photograph and schematic optical alignment of the UV-vis spectrophotometer	44
Figure 3.4 Photograph and schematic optical alignment of the fluorescence spectrophotometer.	46
Figure 3.5 Photograph and schematic representation of the Raman spectroscopy.	47
Figure 3.6 Photograph of the AFM.	48
Figure 3.7 Photograph of the centrifuged GO and of as-purchased GO for reference.	49
Figure 3.8 AFM images of GOs with various magnifications	49
Figure 3.9 Typical Raman spectrum of GO.	50

Figure 3.10 Schematics of typical phonon scattering processes responsible for Raman modes in graphite.	51
Figure 3.11 Absorption and PLE spectra of GOs dispersed in aqueous solution...	52
Figure 3.12 Absorption spectra of GOs in the aqueous solution at various pH conditions.....	52
Figure 3.13 PLE intensity map of highly exfoliated GO.....	54
Figure 3.14 PLE intensity map of GQDs synthesized by oxidation of carbon fibers	54
Figure 3.15 PL spectra of P ₁ and P ₂ peaks in the GOs with various pH of the solvent.....	55
Figure 3.16 Chemical structures of benzene and naphthalene. Energy diagram of the quasi-molecular states.....	56
Figure 3.17 PL spectra of phenol, benzoic acid, salicylic acid, phthalic acid, and 1-naphthoic acid	58
Figure 3.18 PL and PLE properties of GOs before and after dialysis process	59
Figure 3.19 PL and PLE of GOs before and after the reduction process.	61
Figure 3.20 PL decay curves of P ₁ and P ₂ in the GOs.....	62
Figure 4.1 Schematic image of sp ² carbon clusters	67
Figure 4.2 Photograph of GO solutions for pH 3, 4, 7 and 12.	68
Figure 4.3 Schematic optical alignments and photograph of the time-resolved PL measurement.....	70
Figure 4.4 PL and PLE spectra of GO in aqueous solution.....	72
Figure 4.5 Optical microscopic and AFM image of GO	74
Figure 4.6 Aberration-corrected TEM image of a single sheet of suspended GO .	75
Figure 4.7 Schematic image of ensemble emission from the multiple GND states of GO.	76
Figure 4.8 Model structures for the GNDs with size scaling	77
Figure 4.9 Scaling relations for the <i>GW</i> bandgaps	78
Figure 4.10 Photograph of the reduced GO solution.....	80
Figure 4.11 PL and PLE of reduced and as-prepared GO	80
Figure 4.12 Time-resolved PL of GO in aqueous solution.....	82
Figure 4.13 Schematic illumination of the exciton in the QD array.....	83
Figure 4.14 PL and PLE of GO in various pH solvent.....	87

Figure 4.15 Absorption spectra of GO in various pH solvent.....	88
Figure 4.16 Atomic structure and absorption spectra for the hydrogen, hydroxyl and carboxyl terminated GNDs.....	89
Figure 4.17 Atomic structures and the absorption spectra for GNDs with deprotonation, neutral and protonation.....	90
Figure 5.1 Schematic PLE intensity map of 2D semiconducting TMDs.....	93
Figure 5.2 Typical optical microscope images of monolayer MoS ₂	94
Figure 5.3 Schematic diagram and photograph of the confocal optical system for PLE measurements.....	96
Figure 5.4 Schematic diagram of the apparatus for the reflection measurements..	97
Figure 5.5 Schematic illustration of typical Raman modes for the bulk MX ₂	99
Figure 5.6 AFM images and height profiles for monolayer MoS ₂	100
Figure 5.7 Energy band structures, DOS and optical conductivity of monolayer MoS ₂	101
Figure 5.8 Properties of monolayer MX ₂	105
Figure 5.9 Excitation power-dependent PL spectra of monolayer WSe ₂	107
Figure 5.10 PLE spectra of monolayer MX ₂	109
Figure 5.11 PLE spectra of bilayer MoS ₂	111
Figure 5.12 PLE spectra of bilayer WS ₂	112
Figure 5.13 PL and PLE spectra of monolayer MoS ₂	114
Figure 5.14 Calculated energy landscape and optical spectra for monolayer and bilayer MoS ₂	117
Figure 5.15 Calculated topology of the electron energy bands for monolayer WS ₂	118
Figure 5.16 Calculated end points of the relaxation paths of photoexcited carriers for monolayer MoS ₂	120
Figure 5.17 Excitation and relaxation pathways for photocarriers.....	123
Figure 6.1 Summary of the characteristic optical properties of the atomically thin 2D materials studied in this thesis.....	127

Chapter 1. Introduction

1.1. Background

Atomically thin quasi-two-dimensional semiconductors

Atomically thin quasi-two-dimensional (2D) semiconductors are new class of materials known for overcoming the scaling limitation of Moore's Law (Figure 1.1a).¹ The excellent optoelectronic properties of the 2D materials have an impact on state-of-the-art nanotechnology. The extreme geometrical confinement and weak dielectric screening of electrons give the materials unique electronic and optical properties.^{2, 3} The flexibility⁴ due to the atomically thin and elastic structure (Figure 1.1b) enables next generation of optoelectronics meeting the demand for wearable devices. The enthusiasm for the atomic layered materials was triggered by the realization of graphene from graphite, a carbon allotrope, by Geim and Novoselov.^{5, 6}

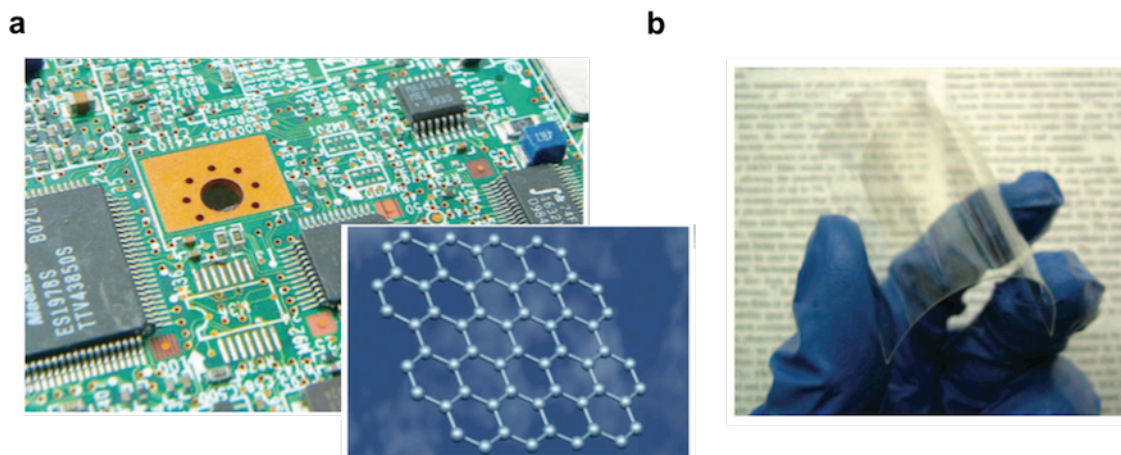


Figure 1.1 (a) Electronic tip and schematic structure of graphene. (Reproduced from Ref. ¹) (b) Graphene oxide thin films on a plastic substrate. (Taken from Ref. ⁷)

Carbon is one of the most important elements, because a main frame of organic materials consist mainly of carbon atoms. One of carbon allotropes is graphite and it has

an sp^2 -hybridized crystal structure with a honeycomb lattice. Interestingly, carbon can form all dimensionality of chemical structures from 0D to 3D with one atom thickness. Figure 1.2 shows atomic structures of sp^2 carbon allotropes; fullerene, carbon nanotube, and graphene. Discovery of fullerene (0D) in 1985,⁸ carbon nanotube (1D) in 1991,⁹ and graphene in 2004⁵ has triggered numerous studies in the fields of nano-carbon materials. Since the isolation of graphene from graphite, researchers have explored unique properties of other atomically thin layered materials such as chemically derived graphene, particularly graphene oxide (GO),¹⁰ silicene (or an atomically thin Si layer with thickness of single atom),¹¹ hexagonal boron nitride (h-BN),¹² black phosphorene ((or an atomically thin P layer with thickness of single atom)),¹³ and transition metal dichalcogenides (TMDs).¹⁴ The 2D atomically thin layered materials have triggered numerous researches because of their excellent physical and chemical properties, for example, high carrier mobility^{15, 16} and photoresponsivity¹⁷⁻¹⁹ making ideal for application of field effect transistors, photodetector, mechanical strength for composites,²⁰ high capacitance for energy storage,^{21, 22} and efficient photocatalytic properties²³ that have been studied by researchers for decades.

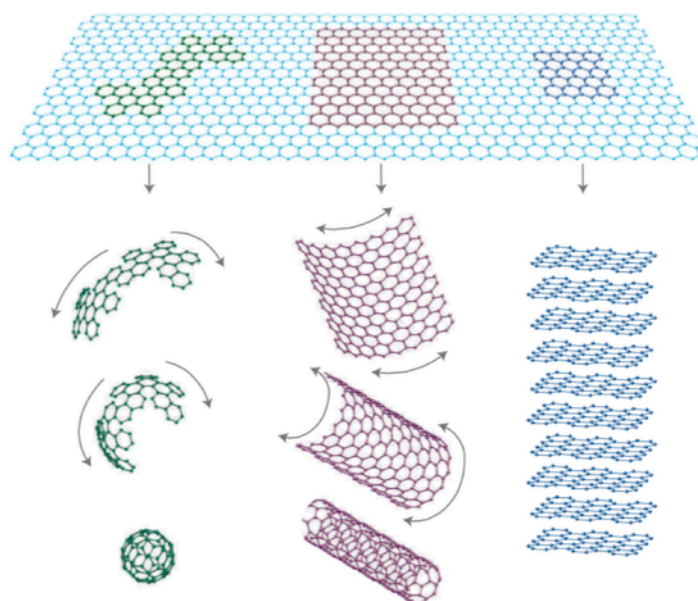


Figure 1.2 Structure of sp^2 carbon allotropes; fullerene, carbon nanotube, and graphene.

The figure was taken from Ref. ²⁴.

Chemically derived graphene (graphene oxide)

Graphene has attracted much attention because of its unique properties and numerous applications.²⁴⁻³⁰ However, graphene is a zero-bandgap material, which limits the study of the fundamental optical properties and optoelectronic applications in the visible light region.^{5,31} The possible methods for introducing the bandgap of graphene are the application of lateral strong electric field for bi-layer graphene, cutting graphene to create nanoribbons and quantum dots, and chemical treatments (functionalization).³²⁻³⁴ The chemical functionalization of graphene offers the modulation of the electronic structure. The theoretical studies on the model systems of chemically functionalized graphene predict an optical bandgap due to localization in the π -electron system.³⁵⁻³⁷ One of the most promising chemically functionalized products of graphene is GO. GO is a non-stoichiometric compound and has inhomogeneous structures. A large fraction of carbon is sp^3 hybridized and covalently bonded with oxygen, and the remaining carbon atoms form sp^2 hybridized clusters with various sizes,³⁸ which determine the optical and electronic properties of GO. Since the observation of broad photoluminescence (PL) in the visible³⁹ and near-infrared (NIR) region,^{40, 41} the PL properties of GO have been studied extensively.^{42, 43} Tunability of luminescent color by oxidation or reduction makes GO attractive especially for applications as light-emitting devices³¹ as well as PL labels in cells.^{40, 44}

Transition metal dichalcogenides

Quasi-two-dimensional (2D) properties of TMDs have long attracted a great deal of interest in fundamental research.⁴⁵ Since the successful isolation of graphene and

other atomically thin crystals from the layered bulk compounds, the interest in TMDs in their ultimate thickness regime has been renewed and provides discoveries of their unique properties.⁴⁶⁻⁴⁸ Recent findings on the novel optical properties of semiconducting 2D TMDs such as MoS₂ and WSe₂ include emerging band-gap PL,^{49, 50} controlled valley polarization,⁵¹⁻⁵³ strongly bound trions,^{54, 55} second harmonic generation,^{56, 57} strain-induced optical gap modulation,^{58, 59} and surface sensitive luminescence.⁶⁰⁻⁶² Along with the attractive electrical properties¹⁵ and recent progress in the materials synthesis,^{63, 64} these 2D TMDs show positive prospects for their applications in optoelectronic devices.^{65, 66}

1.2. Motivation

Exploding demands of new class of flexible and stretchable electronics^{67, 68} have appeared, which is a new way to manage information. The demands have been also expanded to optoelectronics such as flexible light emitting diode⁶⁹ and photovoltaic cell.⁷⁰ In this technological phase, the key factor is their portability not only a quest for their performance. This class of devices requires mechanical flexibility in the implemented materials. Nevertheless, conventional inorganic bulk materials are rigid and do not allow their implementation for the flexible devices. Although alternative flexible materials such as amorphous Si and organic semiconductors have been extensively developed,⁷¹ further improvement of carrier mobility is required to achieve faster operation. The concept of the flexible device possesses a strong affinity with the atomically thin 2D sheet especially GO and TMDs because of the excellent mechanical, electrical, optical properties and also solution-processability.^{7, 64, 72, 73}

In optoelectronic devices, incident light controls carrier-transporting properties or electric field controls optical properties of the materials. The key factor is light-mater

interaction to determine the nature of photoelectric conversion since photoexcited carrier generation and excitation are the major process in the conversion. In this thesis, we focus on the behavior of photocarrier in GO and 2D semiconducting TMDs. Both of the materials show the extraordinarily strong light absorption despite being atomically thin. TMDs can absorb sunlight as high as 5-10%,⁷⁴ while graphene can absorb 2.3% light,^{75, 76} which is considered to be the comparable level to GO.⁷⁷ The strong-light matter interaction provides these materials advantages for efficient optical response. It should be noted that these two materials possess contrasting properties in their tunability of optical properties. GO has excellent tunability of optical gap in a wide range by chemical modification of its structures,^{29, 78-80} while TMDs have rigid optical gap.^{49, 50}

While the expected technological impacts of GO and TMDs are significant, the lack of accumulated knowledge associated with the photocarrier behavior is an obstacle for their application. A challenge is clarifying the size-dependency of the optically active domains in GO on the luminescent mechanisms. Also another challenge is investigating the behavior of photo-excited carriers with high energy far from the band edge of TMDs. In this thesis, our primary aim is to explore generation and relaxation of photocarrier in GO and 2D semiconducting TMDs. Understanding the static and transient behavior of the photocarriers will provide guiding principle of architectures of the materials and optoelectronic devices.

1.3. Chapter outline

In the following Chapter 2, fundamental optical and electronic properties of GO and TMDs are introduced. In Chapter 3 we clarify the mechanisms of the blue and UV luminescence from highly exfoliated GO. In Chapter 4 we investigate the mechanisms

and dynamics of the NIR PL from GO. In Chapter 5, the mechanisms of photocarrier generation and relaxation in TMDs are discussed. As a summary of this thesis, conclusion and outlook including suggested future works are provided in Chapter 6.

Chapter 2. Fundamental properties of atomically thin layers

2.1. Quantum confinement of electrons

The structures that have sizes down to several tens nanometers may be considered as nanomaterials. Nanoscale structures of semiconductors exhibit unique optical properties depending on their size, which bulk solids do not show. This is called quantum confinement effect and directly modulates the energy level of electrons in semiconducting nanostructures.⁸¹ According to the Heisenberg uncertainty principle, if a particle confined to a region of length Δx , its momentum Δp_x is given by

$$\Delta p_x \sim \frac{\hbar}{\Delta x}, \quad (\text{Eq. 2.1})$$

where \hbar is associated with Planck's constant of h by $\hbar = h / 2\pi$. The confinement gives the particle an additional kinetic energy $E_{\text{confinement}}$ written by

$$E_{\text{confinement}} = \frac{(\Delta p_x)^2}{2m} \sim \frac{\hbar^2}{2m(\Delta x)^2}, \quad (\text{Eq. 2.2})$$

where m is the electron mass. This confinement energy is significant if this kinetic energy is larger than thermal energy $\frac{1}{2}k_B T$, where k_B is Boltzmann constant and T is the temperature. This condition is written by

$$\frac{\hbar^2}{2m(\Delta x)^2} > \frac{1}{2}k_B T \quad (\text{Eq. 2.3})$$

In a typical semiconductor, the confinement effect becomes prominent if Δx is smaller than 5nm at room temperature (= 300 K) with electron effective mass of $m_e^* \sim 0.1m_0$ (m_0 is the free electron mass). When the atomically thin sheet consists of single layer, the thickness is smaller than 1 nm and exhibit extraordinarily pronounced quantum

confinement effects of electrons.

Under the strong confined condition, electron and hole motion is limited and the number of degrees of freedom is given associated with the type of quantum confinement. Figure 2.1 shows low-dimensional quantum confined structures that are classified by their dimensionality or confined directions. The density of states (DOS) of 3D bulk semiconductors is proportional to $E^{1/2}$, and those of quantum wells (2D) shows step like function, while those of quantum wires (1D) and dots (0D) exhibit sharpening and divergence of DOS. The DOS of quantum wires is proportional to $E^{-1/2}$ and that of quantum dots is expressed by delta function. This divergence results in strong light-matter interactions at their resonant energy. These features of DOS can be detected by scanning tunneling spectroscopy as the differential conductance dI/dV .⁸² The quantum wells, mainly III-V compound semiconductors, are fabricated by molecular beam epitaxy or metal-organic chemical vapor deposition under controlling thickness with atomic precision. The quantum wells are often applied for laser because the low dimensional structure decreases threshold current of laser oscillation.⁸³ The quantum confinement effects allow the DOS to have a steep edge and concentrates electrons in the energy states at the edge that contribute the specific optical transitions. The efficiency of laser emission is further improved by using quantum wires or dots, which is associated with sharpening DOS with decreasing the dimensionality.

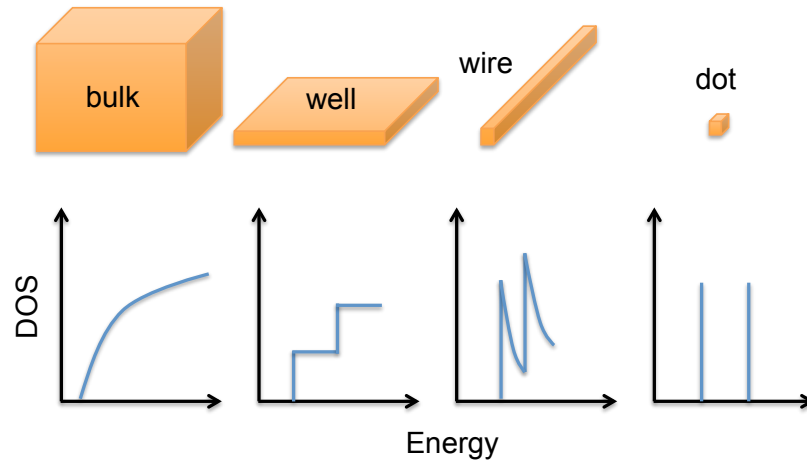


Figure 2.1 Schematic structures and DOS of bulk crystals, quantum wells, wires and dots.

2.2. Atomic structures

2.2.1. Graphene and chemically derived graphene

Graphene

Figure 2.2a shows an atomic structure of graphene, where A and B are the sublattices and \mathbf{a}_1 and \mathbf{a}_2 are unit vectors of graphene ($|\mathbf{a}_1| = |\mathbf{a}_2|$). Graphene consists of carbon atoms aligned with honeycomb structure in a single plane. This atomic structure can be defined by lattice vectors written as

$$\mathbf{a}_1 = \frac{a}{2}(3, \sqrt{3}), \quad \mathbf{a}_2 = \frac{a}{2}(3, -\sqrt{3}), \quad (\text{Eq. 2.4})$$

where $a = 1.42 \text{ \AA}$ is the carbon-carbon bond length (Figure 2.2a). Figure 2.2b shows a Brillouin zone of graphene, where the reciprocal-lattice vectors \mathbf{b}_1 and \mathbf{b}_2 are given by

$$\mathbf{b}_1 = \frac{2\pi}{3a}(1, \sqrt{3}), \quad \mathbf{b}_2 = \frac{2\pi}{3a}(1, -\sqrt{3}) \quad (\text{Eq. 2.5})$$

The thickness of a single atomic layer (or monolayer) graphene sheet is $\sim 3.4 \text{ \AA}$ ⁸⁴, which corresponds to interlayer distance of graphite. Highly symmetric points in momentum

space are named as K, K', M and Γ (Figure 2.2b). Particularly, K and K' points at the corners of the Brillouin zone are important for the physics and called Dirac points, which described in detail in Section 2.3.1.

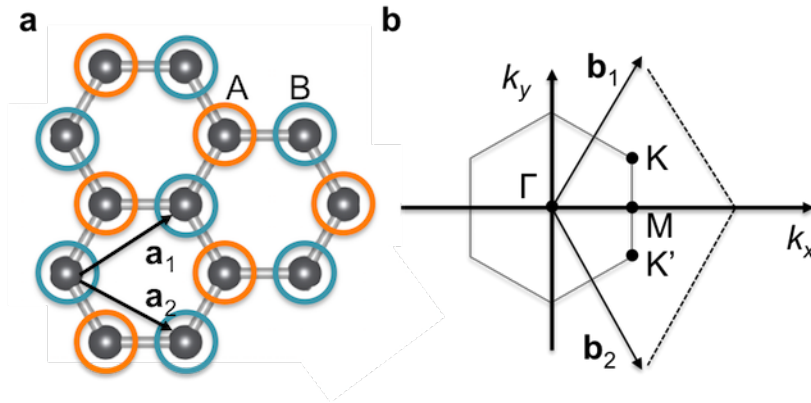


Figure 2.2 (a) Honeycomb lattice of graphene, where A and B highlighted by orange and blue circles are the sublattice. \mathbf{a}_1 and \mathbf{a}_2 are unit vectors of graphene. (b) The Brillouin zone of graphene, where highly symmetric points are named as K, K', M and Γ . \mathbf{k}_x and \mathbf{k}_y are momentum vector.

Stacking graphene layers

Figure 2.3a and b illustrate the crystal structures of bilayer graphene with different two stacking manners. Natural graphite forms AB layer stacking and the stacking manner in AB stacking results in the hybridization of the π orbitals in the out-of-plane direction. Stacked graphene, especially bilayer graphene, has been extensively studied to tune the bandgap because the stacking affects its electronic structures.^{34, 85} Bilayer graphene has two stacking manner referred as AB and AC stacking. The AC stacking differs from AB stacking by 60-degree rotation. An intrinsic van der Waals force is applied between layers. Figure 2.3c and d show crystal structures of (c) ABA and (d) ABC stacking trilayer graphene. The trilayer graphene can form ABA and ABC layer

stacking. In these trilayer graphene, first and second layers form AB layer stacking, but third layer has two kinds of stacking manner, putting atoms on B or C alignment as a third layer as shown in Figure 2.3c and d. The ABA and ABC layer stacking possess a different van der Waals interlayer coupling and exhibit a different response to electric field.⁸⁶

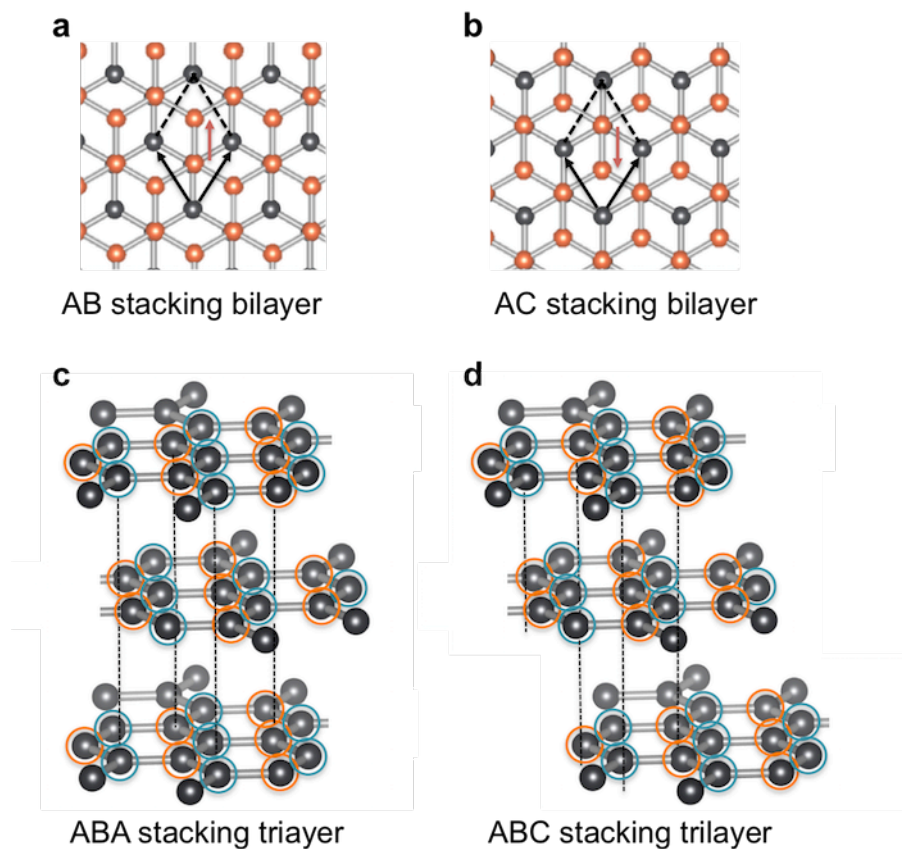


Figure 2.3 Crystal structure of (a) AB and (b) AC stacking bilayer graphene. The first layers are colored in grey and the second layers are colored in orange. The dashed diamonds show the unit cells and black arrows are the unit cell vectors. The red arrow indicates the geometrical shift of the second layer with respect to the first layer. Crystal structure of (c) ABA and (d) ABC stacking trilayer graphene. The orange circle and blue circles highlight the A and B sublattices of the graphene honeycomb structure.

Chemically derived graphene

Chemically derived graphene, particularly, graphene oxide (GO) had been discovered first as an exfoliation of graphite oxide by the Oxford chemist Benjamin Brodie in 1859.^{29,87} GO is a derivative of graphene by a chemical modification. In this thesis, we define GO as “graphene” oxide and not “graphite” oxide. Chemically derived graphene includes other derivatives of graphene such as fluorinated⁸⁸ or brominated⁸⁹ graphite. Functionalization of graphene dramatically alters the physical and chemical properties of graphene. Therefore, it is not appropriate to refer to GO simply as graphene.⁷⁷

GO is synthesized by modified Hummers method,^{90, 91} in which graphite is oxidized and exfoliated in a mixture of H₂SO₄ and KMnO₄ under irradiation of microwave. Figure 2.4a and b shows a chemical structure and atomic model of GO sheet, respectively. Several types of oxygen functional group are covalently bound to the basal plane and sheet edges of graphene sheet. These oxygen functional groups make GO hydrophilic and soluble in water, which can be helpful for solution-processing.^{72, 73} This character is contrasting in that the precursor graphite is hydrophobic. As-prepared GO shows an insulating behavior, while graphene and graphite show metallic behavior. A chemical reduction increases its conductivity up to semiconducting behavior. The functional groups in GO include mainly hydroxyl, epoxy and carboxyl groups.^{92, 93} The solubility of GO allows it to obtain a uniformly deposited thin film which has potential application of optoelectronics. The thickness of monolayer GO sheet is ~0.83 nm,⁹⁰ which is larger than plain graphene because of the oxygen functional groups.

High-resolution TEM image provides us insight into the morphology that largest portion of the layer is composed of clean well-crystallized graphene areas, where the

hexagonal lattice is remained (light gray color in Figure 2.4c). The average size of the well-crystallized areas is from 1 to 6 nm.^{38, 94} Remarkable amount of defects is observed within the crystallized areas (green color in Figure 2.4c).

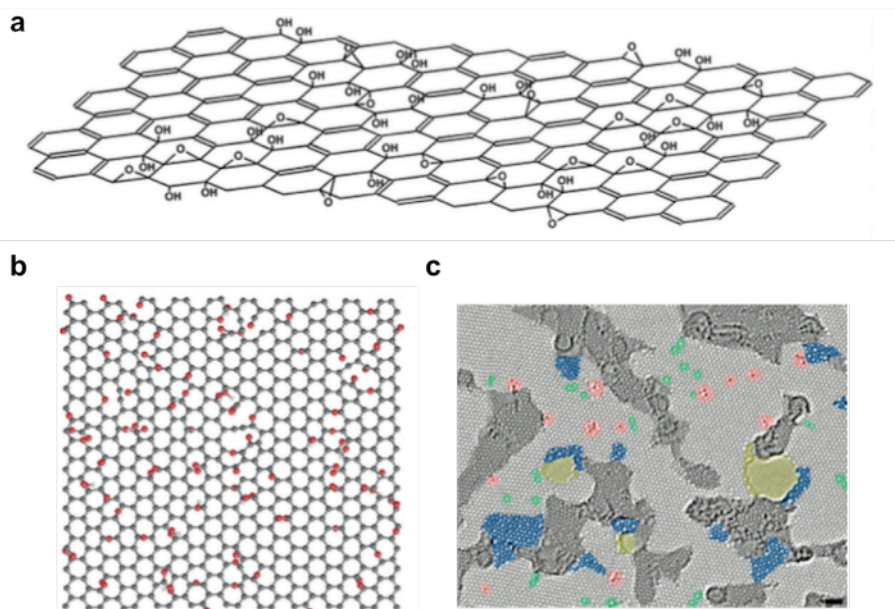


Figure 2.4 (a) Chemical structure of GO sheet according to the Lerf-Klinowski model (taken from Ref.⁹⁵). (b) Atomic model of morphology for single layer GO. Carbon, oxygen and hydrogen atoms are grey, red and white, respectively. (c) Atomic resolution, aberration-corrected high-resolution TEM image, with color added to highlight the different features. The defect free crystalline graphene area is displayed in the original light- gray color. Contaminated regions are shaded in dark gray. Blue regions are the disordered single-layer carbon networks, or extended topological defects, that identified as remnants of the oxidation-reduction process. Red areas highlight individual ad-atoms or substitutions. Green areas indicate isolated topological defects, that is, single bond rotations or dislocation cores. Holes and their edge reconstructions are colored in yellow. Scale bar corresponds to 1 nm. (Reproduced from Ref.⁹⁴).

2.2.2. Transition metal dichalcogenides

Many transition metal dichalcogenides (TMDs) are layer structure like graphite that leads to strong anisotropy in their electrical, chemical, mechanical and thermal properties.^{14, 96} Layered TMDs of MX_2 (M = Mo, W, Nb, Re, Ti, etc., X = S, Se, Te, etc.) have been extensively studied for last half a century.⁴⁵ Molybdenum disulfides (MoS_2) is one of the most typical layered TMDs and seen as a prototype of this system. In the layer structure, the thickness of each layer is typically 6-7 Å, which consists of hexagonally packed transition metal atoms sandwiched between two chalcogen atoms. The M-X bonds are covalently bound, whereas the layers are bound by weak van der Waals force, which allows us to cleavage the layers mechanically. Figure 2.5a shows schematics of the structural polytypes of MX_2 for 2H, 3R and 1T phase. The bulk crystal of MoS_2 has typically three different polytypes, which vary in stacking orders and metal atom coordination in contrast to graphite (see Section 2.2.1). 2H- MoS_2 has hexagonal symmetry, two layers per repeat unit and trigonal prismatic coordination. 3R- MoS_2 has rhombohedral symmetry, three layers per repeat unit, and trigonal prismatic coordination.⁹⁷ 1T- MoS_2 has tetragonal symmetry, one layer per repeat unit, octahedral coordination. Stable crystalline structures is 3R- MoS_2 polytype⁹⁸ and layered 2H- MoS_2 , while the 1T phase is metastable. Annealing at 300 °C can cause a phase transition from 1T- MoS_2 to 2H- MoS_2 .⁴⁸ Since 2H- MoS_2 is the most typical phase, we simply refer MX_2 as 2H- MX_2 in this thesis.

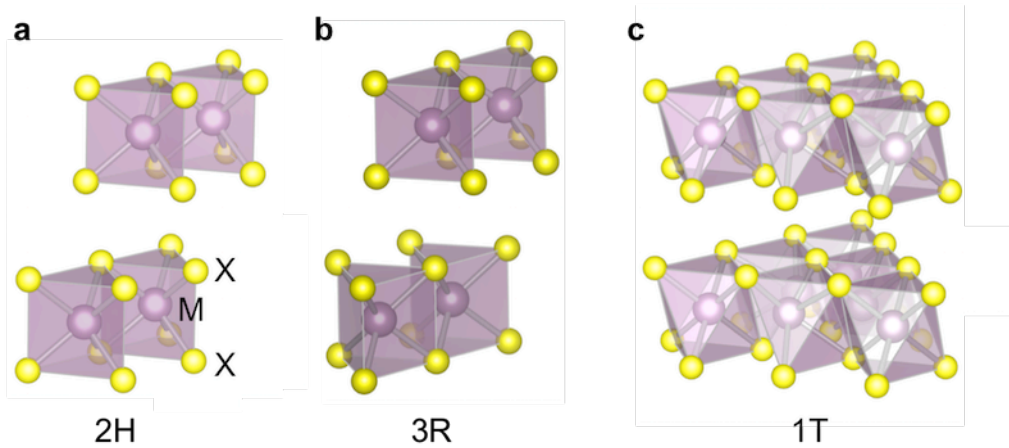


Figure 2.5 Schematics of the structural polytypes for 2H, 3R and 1T phase. The chalcogen atoms (X) are yellow and the metal atoms (M) are purple dots.

2H-MoS₂ is the subject matter of the present thesis. Figure 2.6a and b displays side and top views of atomic structure for 2H-MoS₂, respectively. Its atomic structure can be defined by lattice vectors written as

$$\mathbf{a}_1 = \frac{a}{2}(3, \sqrt{3}), \quad \mathbf{a}_2 = \frac{a}{2}(3, -\sqrt{3}) \quad (\text{Eq. 2.6})$$

where \mathbf{a}_1 and \mathbf{a}_2 are unit vectors of MoS₂ ($|\mathbf{a}_1| = |\mathbf{a}_2|$), and a is the line length of the unit vector. The c -axis is perpendicular to the plane of \mathbf{a}_1 and \mathbf{a}_2 , in which the layer stacks along this c -axis and the interlayer spacing is $\sim 6.5 \text{ \AA}$ ⁴⁶. This definition of c -axis is the same as that of graphene because both consist of honeycomb lattice structure. Figure 2.6c shows Brillouin zone of 2H-MoS₂ and highly symmetric points in momentum space are named as Γ , K, M, $\bar{\Gamma}$, \bar{K} , and \bar{M} . Since the band edge is at K or Γ point (see Figure 2.10), the K and Γ points are important for understanding the optical transition and carrier transport.

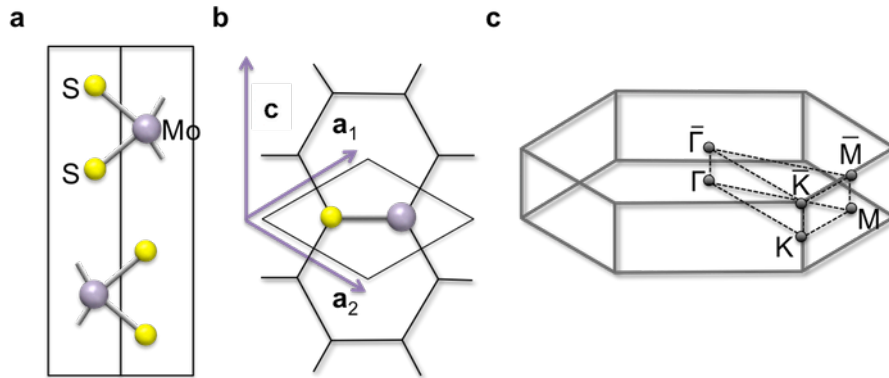


Figure 2.6 (a) Side and (b) top views of atomic structure of 2H-MoS₂ with hexagonal lattice. The unit cell is delineated. \mathbf{a}_1 , \mathbf{a}_2 and \mathbf{c} are unit vectors of MoS₂ ($|\mathbf{a}_1| = |\mathbf{a}_2|$). Honeycomb structure consisting of Mo (purple dots) and S₂ (yellow dots) located at the corners of hexagons is seen in the top view. (c) Corresponding Brillouin zone with symmetry directions. (Reproduced from Ref. ⁹⁹)

2.3. Fundamental electronic structures

2.3.1. Graphene and chemically derived graphene

sp^2 Hybridization

Isolated carbon atom has four valence electrons in 2s and 2p orbitals. When carbon atoms bind to each other, their 2s and 2p orbitals can mix with one another in sp^n ($n=1, 2, 3$) hybridized orbitals. Graphene has the sp^2 configuration. In the configuration, the orbitals for one 2s and two 2p orbitals mix to form three in-plane covalent bonds with 120° from each other, which is called σ bond as shown in Figure 2.7. Another valence electron is in the 2p_z orbital. The p_z electrons that remain perpendicular to the hexagonal network form delocalized π electron states as shown in Figure 2.7. The π electron states form valence and conduction energy bands nearby Fermi level, while the σ electron states are far from Fermi level, and not dominantly contribute to carrier transports and optical transitions.

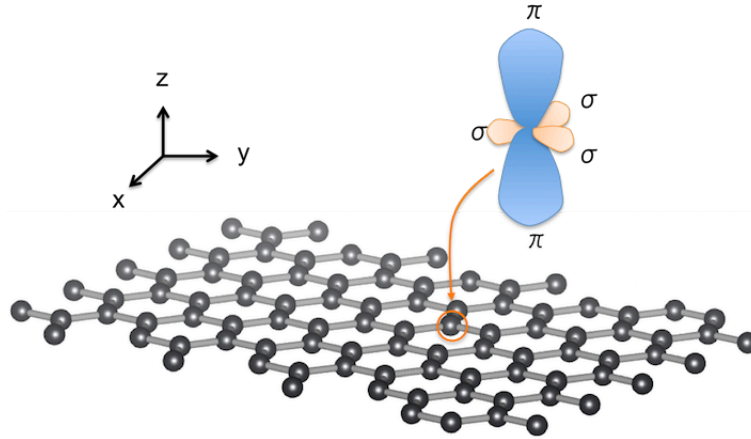


Figure 2.7 The σ and π orbitals of carbon atom in sp^2 honeycomb lattice. (Reproduced from Ref.¹⁰⁰)

Energy band structures

In a tight-binding approach, the energy dispersion of graphene is calculated by solving the eigenvalue problem for a Hamiltonian H and an overlap integral matrix S written by¹⁰¹

$$H = \begin{pmatrix} \varepsilon_{2p} & -\gamma_0 f(k) \\ -\gamma_0 f(k)^* & \varepsilon_{2p} \end{pmatrix} \text{ and } S = \begin{pmatrix} 1 & sf(k) \\ sf(k)^* & 1 \end{pmatrix}, \quad (\text{Eq. 2.7})$$

where ε_{2p} is the site energy of the 2p atomic orbital, γ_0 is the nearest neighbor C-C interaction energy, s is the overlap integral. The function $f(k)$ is given by

$$f(k) = e^{ik_x a / \sqrt{3}} + 2e^{-k_x a / 2\sqrt{3}} \cos \frac{k_y a}{2}, \quad (\text{Eq. 2.8})$$

where k_x and k_y are momentum along x and y axis. The solution of the secular equation

$$\det[H - ES] = 0 \quad (\text{Eq. 2.9})$$

provides energy dispersion of graphene expressed by

$$E^\pm(\mathbf{k}) = \frac{\varepsilon_{2p} \pm \gamma_0 \sqrt{|f(\mathbf{k})|^2}}{1 \mp s \sqrt{|f(\mathbf{k})|^2}}. \quad (\text{Eq. 2.10})$$

The plus and minus in this equation correspond to bonding (π) and anti-bonding (π^*)

state of the two atoms composing the unit cell, in which they yield valence and conduction bands. Figure 2.8 shows the full band structure of graphene and the zoom in of the energy bands close to one of the Dirac points. The linear energy dispersion nearby \mathbf{K} or \mathbf{K}' points are called Dirac cone (the inset of Figure 2.8). This energy dispersion near by Dirac point (\mathbf{K} or \mathbf{K}') can be expressed by

$$E_{\pm}(\mathbf{q}) \approx \pm \hbar v_F |\mathbf{q}|, \quad (\text{Eq. 2.11})$$

where the momentum $\mathbf{q} = \mathbf{k} - \mathbf{K}$ with $|\mathbf{q}| \ll |\mathbf{K}|$. In this region, electron transport is essentially governed by Dirac's (relativistic) equation.¹⁰² The charge carriers in graphene behave as massless Dirac fermions and enable us to access quantum electrodynamics.

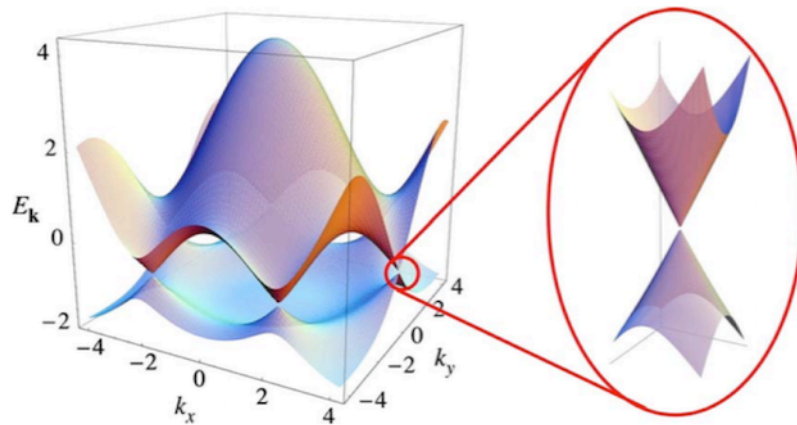


Figure 2.8 Energy dispersion (or energy of electron as a function of momentum) for the π and π^* bands in graphene. The inset shows the zoom in of the energy bands close to one of the Dirac points (at the \mathbf{K} or \mathbf{K}' points) (Taken from Ref. ¹⁰³).

Induction of energy gap to graphene by chemical modification

One of motivation to use chemically derived graphene is introduction of energy gap to graphene that is absence of energy gap. Application of graphene to logic circuits

has a fundamental limitation because of a modest on-off ratio in graphene based transistors. It originates from thermally excited carriers associated its zero gap. On the other hand, one can tune the energy gap of graphene oxide (GO), one of chemically derived graphene, and therefore controllably transform GO from an insulator to semiconductor and to a graphene-like semi-metal.³² The electronic conductivity is governed by the ratio of sp^2 and sp^3 fractions, where π -states from sp^2 carbon are conducting, while sp^3 -bonded carbons are insulating.

2.3.2. Transition metal dichalcogenides

Hybridization of d and p orbitals

Electronic character of d-orbital, that shares band edge of TMDs,¹⁰⁴ is determined based on ligand field theory. The theory describes the bonding and orbital arrangement of transition metal complexes like TMDs. The theory considers interaction between valence atomic orbitals and ligands, i.e., chalcogen atoms in TMDs to converge the interaction into appropriate energy. Figure 2.9 shows a schematic illustration of hybridization of d and p orbitals in MX_2 . The valence band maximum (VBM) states at K point mainly consist of $d_{x^2-y^2,xy}$ orbitals of transition metal M atoms and $p_{x,y}$ orbitals of chalcogen X atoms.^{105, 106} The conduction band minimum (CBM) at K point is contributed by d_{z^2} orbital of M and $p_{x,y}$ orbitals of X. The d and p orbitals hybridize significantly and result in formation of the covalent bond between M and X atoms. The orbitals of $d_{x^2-y^2,xy}$ and $p_{x,y}$ has a repulsion and push up the d orbitals by Δ_1 , forming the VBM, and push down the p orbital by Δ_1' . Similarly, The orbitals of d_{z^2} and $p_{x,y}$ push up the d orbitals by Δ_2 , forming the CBM, and push down the p orbitals by Δ_2' . The magnitude of the repulsion depends on the overlap integral of the d and p orbitals and the difference of their energy. Basically the larger overlap integral and the smaller difference of their energy lead to the larger repulsion. As a result, the Δ_2

is larger than Δ_1 in this system.

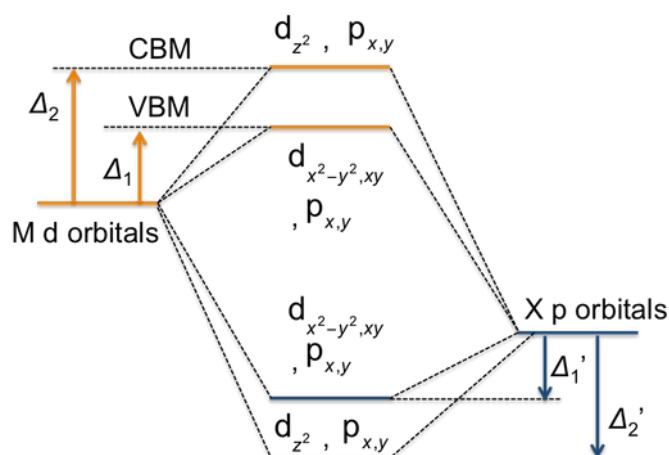


Figure 2.9 Schematic illustration of hybridization of d and p orbitals in MX_2 , displaying the origin of CBM and VBM. (Reproduced from Ref. ¹⁰⁵)

Energy band structures

The electronic band structures of monolayer MoS_2 changes significantly with respect to that of bulk crystals^{49, 107-109} as shown in Figure 2.10. The lowest energy transitions are in an indirect bandgap between Γ point of the conduction band and K point of the valence band for bulk to bilayer MoS_2 , while monolayer MoS_2 is characterized by a direct bandgap and the direct excitonic transitions occur at K point. As the number of layers decreases from bulk to monolayer, the fundamental indirect bandgap between Γ and K point increases. At the same time, the direct bandgap at the K point stays almost constant, that is, independent of the number of layers, i.e. thickness. The thickness dependent indirect bandgap near Γ point stems from the character of a linear combination of d orbitals on Mo atoms and antibonding p_z orbitals on S atoms. They have strong interlayer coupling. On the other hand, d orbitals, strongly localized at Mo atoms, have minimal interlayer coupling since the Mo atoms are in the middle of the S-Mo-S unit cell which compose conduction band states at the K point.⁴⁹

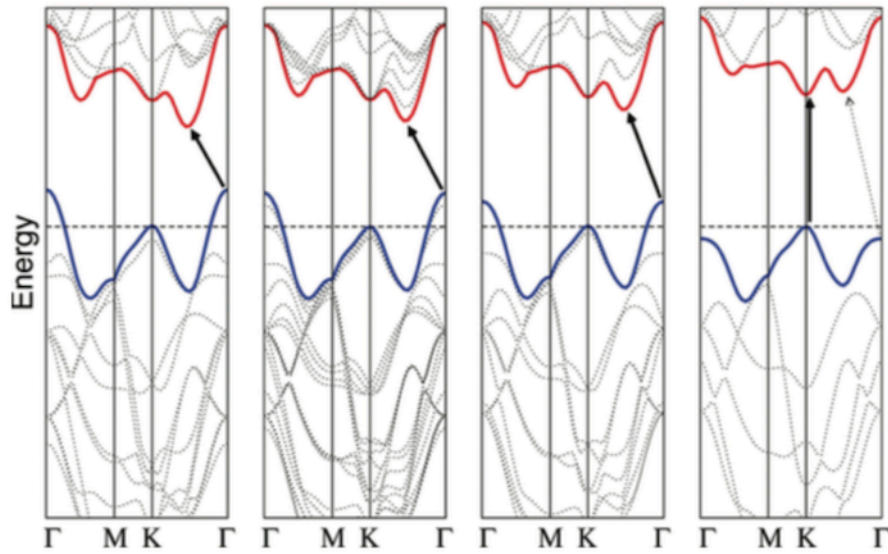


Figure 2.10 Band structures of (a) (from left to right:) bulk, quadrilayer, bilayer, and monolayer MoS₂ calculated by density functional theories. The solid arrows indicate the lowest energy transitions. The arrows indicate the lowest energy transitions. (Reproduced from Ref. ⁴⁹)

Spin splitting

Giant spin-orbit-induced splitting of the valence band also makes the monolayer MX₂ attractive.¹¹⁰ In the MX₂ bulk, Kramer's degeneracy $E^\uparrow(\mathbf{k}) = E^\downarrow(\mathbf{k})$ is established by combination of time-reversal $E^\uparrow(\mathbf{k}) = E^\downarrow(-\mathbf{k})$ and spatial inversion symmetry $E^\uparrow(\mathbf{k}) = E^\uparrow(-\mathbf{k})$, where E^\uparrow and E^\downarrow show two bands occupied by spin up and down electrons, and \mathbf{k} is crystal momentum.^{51, 110-112} This means that both spins up and down can be at both K and K' points in the Brillouin zone shown in Figure 2.11a. In contrast, monolayer MX₂ breaks the spatial inversion symmetry because the two sublattice sites are occupied by one transition metal, M, and two chalcogen X atoms in the monolayer honeycomb lattice structure. This broken spatial inversion symmetry lead to split the valence band along the line Γ -K and the splitting is apparent. The band structure of monolayer MoS₂ (the solid lines in Figure 2.11b) displays the splitting, in which the maximal splitting of the uppermost valence band at the K point amounts 148 meV for

MoS₂ monolayer (note that this is larger than thermal energy at room temperature ~ 26 meV).¹¹³ The dotted lines in Figure 2.11b exhibit the band structure of monolayer MoS₂ without inclusion of the spin orbit interaction that is shown as a reference. The spin-orbit interaction breaks the spin degeneracy of the valence band along the Γ -K line, while without spin-orbit interaction, the valence band do not exhibit the splitting. Mainly the transition metal $d_{x^2-y^2,xy}$ states are responsible for the giant spin splitting.

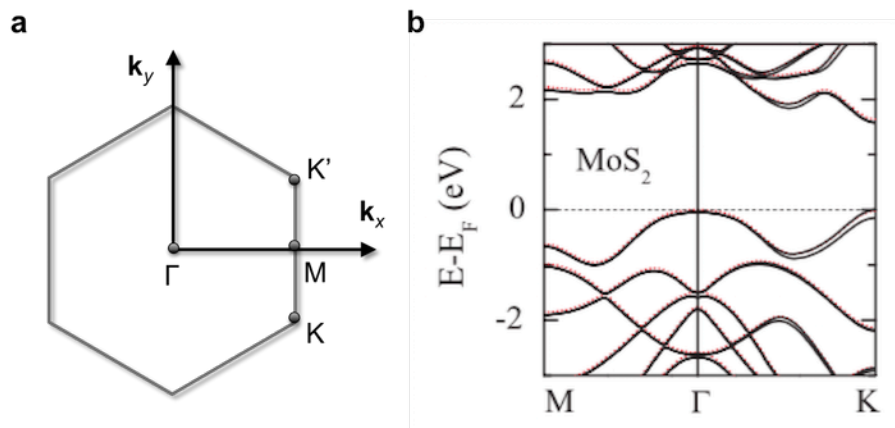


Figure 2.11 (a) Brillouin zone of monolayer MX₂. Highly symmetric points are labeled as K, K', M, and Γ . (b) Band structures calculated for the monolayer MoS₂ with (solid line) and without (dotted line) inclusion of the spin-orbit interaction in first-principles calculations. (Reproduced from Ref. ¹¹⁰)

2.4. Theory of optical transitions

2.4.1. Optical transitions

Fundamental optical transitions are mainly classified as absorption and luminescence processes. Figure 2.12 shows a schematic illustration of the absorption and luminescence process. A photon with energy of $\hbar\omega$ excites an electron and pushes up it from ground to excited states. In this process, the excited states must be vacant because of the Pauli exclusion principle, where two identical fermions (or particles with half-integer spin such as electron) cannot occupy the same quantum state

simultaneously. As a subsequent process, the optical excited electrons relax through radiative or non-radiative transitions from the excited states to the available vacant level in the ground states. Photons are emitted in the radiative decay process, which is called luminescence. Non-radiative decay occurs without photon emission and the energy is released by phonon emission. Basically the phonon emission process is much faster than the radiative decay. Their relationship between radiative and non-radiative decay are combined by PL quantum yield η described by

$$\eta = \frac{\Gamma_r}{\Gamma_r + \Gamma_{nr}}, \quad (\text{Eq. 2.12})$$

where Γ_r and Γ_{nr} are radiative and non-radiative decay rate. The quantum yield is defined by the fraction of the number of absorbed photon and the number of emitted photon. The value of the quantum yield can be a good indicator for development of photovoltaic devices as well as light emitting devices because the quantum yield reflects the quality of crystal.¹¹⁴

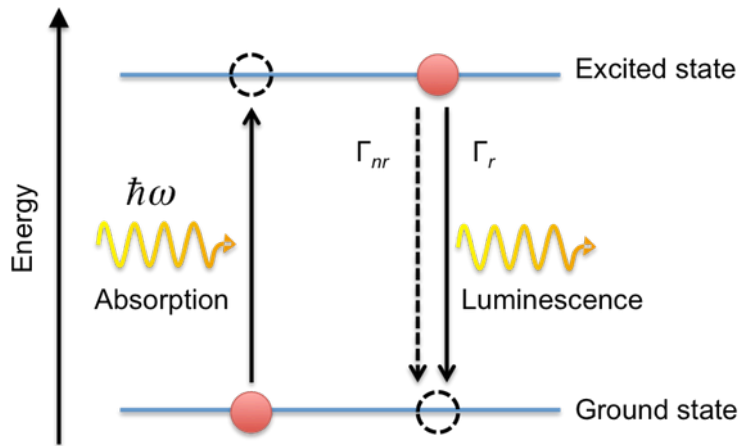


Figure 2.12 Schematic illustration of absorption and luminescence process. The red dots represent electron and the dotted circles show empty states. Γ_r and Γ_{nr} are radiative and non-radiative decay rate, respectively.

In optical measurements, these processes are basically detected through light

absorption and photoluminescence (PL) (or fluorescence). The optical transitions reflect electronic structures of the material, and the transition rates from initial to final state $W_{i,f}$ with optical excitation energy $\hbar\omega$ is derived from Fermi's golden rule written as

$$W_{i,f} = \frac{2\pi}{\hbar} |\langle f | H_1 | i \rangle|^2 \delta(\varepsilon_i - \varepsilon_f - \hbar\omega), \quad (\text{Eq. 2.13})$$

where $|i\rangle$ and $|f\rangle$ are initial and final states with momentum \mathbf{k}_i and \mathbf{k}_f and energies ε_i to ε_f , and H_1 is the interaction potential. If the transition matrix element $\langle f | H_1 | i \rangle$ has a value other than zero, the optical transition is allowed otherwise forbidden, depending on the symmetry of the wavefunction and direction of polarization. The delta function $\delta(\varepsilon_i - \varepsilon_f - \hbar\omega)$ means that momentum and energy are conserved in the optical transition process. The optical transitions are likely to occur in van Hove singularities (VHS) in the electronic structure, in which these correspond to singularities in the DOS. If the VHS are in both the conduction and valence bands, singularity comes up in the optical conductivity. The appropriate condition happens only at highly symmetric points in the Brillouin zone.

2.4.2. Molecule

Figure 2.13a shows molecular orbitals of benzene which is a minimum component of graphene. The π orbital originates from six uncombined 2p orbitals in which each orbital has one electron. In the molecular orbital, energy gap corresponds to the gap between highest occupied molecular orbital (HOMO) and lowest unoccupied molecular orbital (LUMO) since electrons are in the bonding orbitals (π), but electrons are absent in anti-bonding orbitals (π^*). Optical transitions, called π - π^* transition, occur in the HOMO-LUMO gap and the energy depends on the size of molecules as shown in Figure 2.13b. In this calculation based on density functional theory (DFT), the energy gap of "single" benzene is ~ 7 eV and the gap decreases down to ~ 2 eV for cluster of 37

aromatic rings because of decreasing the quantum confinement energy explained in Section 2.1.³⁹ In this thesis, the optical transitions in GO that exhibits blue and UV luminescence are more like this type of transitions, although the emission species of GO are not an isolated molecule, which will be discussed in details in Chapter 3.

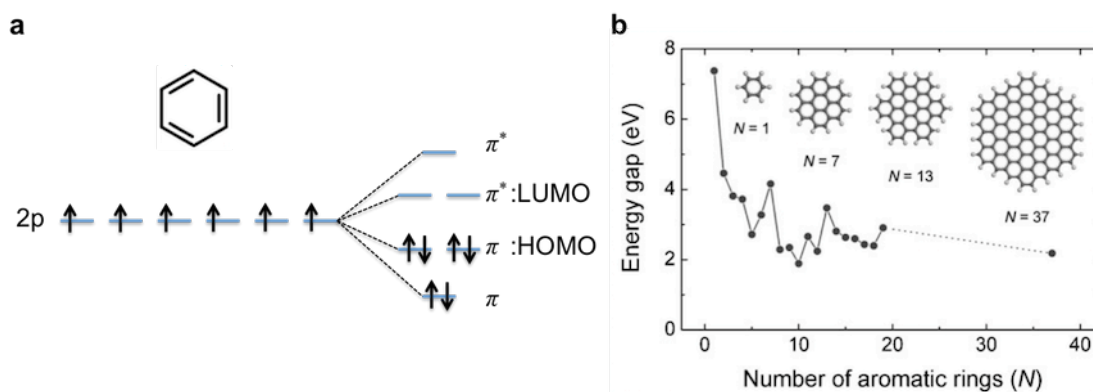


Figure 2.13 (a) Chemical structure (top), uncombined 2p orbitals (left) and π orbitals of benzene molecule (right). The arrows indicate up and down spin of electron. π and π^* are bonding and anti-bonding orbitals, respectively. HOMO and LUMO are indicated. (b) Energy gap of π - π^* transitions calculated based on DFT as a function of the number of aromatic rings (N). The inset shows the structure of the sp^2 molecules used for the calculations. (Taken from Ref. ³⁹ for (b))

2.4.3. Semiconductors

Interband transition

With increasing the size of a molecule, the system approaches to semiconducting solids, and the resulting electronic structure fundamentally changes. In contrast with molecular orbitals, semiconductors form continuous energy band which is consequence of overlapping millions of energy states with slightly different energies in solids due to the Pauli exclusion principle in solids. Figure 2.14a shows a schematic image for the generation of an electron-hole pair accompanied with optical transition between valence and conduction bands of a typical semiconductor. As the excitation photon energy

increases and exceeds to the energy gap between valence and conduction bands, electron in the valence band is excited to unoccupied state in the conduction band with momentum k_e and hole with momentum k_h is left behind. When the Coulombic interaction between electron and hole can be negligible, the excitation photon energy corresponds with the energy gap. However, when electrons are strongly confined in nano-sized materials such as atomically thin 2D materials, the Coulombic interaction between negative charge of electron and positive charge of hole cannot be negligible and the optically generated excited electron and hole pair forms a bound state called exciton.

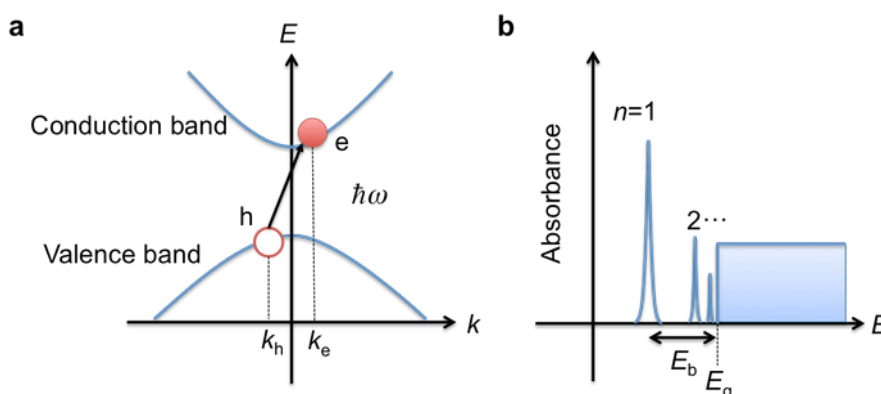


Figure 2.14 (a) Generation of an electron-hole pair accompanied with optical transition between valence and conduction bands of typical semiconductors. The red dot and circle indicate excited electron and hole, respectively. Momentum of excited hole and electron is k_h and k_e , respectively. (b) Schematic excitonic optical absorption spectrum of a 2D material, where n is main quantum number, E_b is the binding energy of exciton and E_g is the energy of the band gap.

Exciton

The bound state of electron-hole pair with the Coulomb interaction is called exciton. Since electron is negatively charged and hole is positively charged, this state

can be considered as analogous picture of a hydrogen atom. The excitonic absorption exhibits characteristic features below the band gap energy in the absorption spectrum as shown in Figure 2.14b. The binding energy of exciton E_n is described by

$$E_n = -\frac{\mu \varepsilon^4}{2\hbar^2} \frac{1}{\varepsilon_0^2} \frac{1}{n^2}, \quad (\text{Eq. 2.14})$$

where μ is reduced mass of exciton ($1/\mu = 1/m_e^* + 1/m_h^*$, m_e^* and m_h^* is the effective mass of electron and hole, respectively), ε_0 is static background dielectric constant of the material, and n is main quantum number. The binding energy becomes large if the material has large bandgap because it is insensitive to polarization and the ε_0 is small. Such a strongly bound exciton enhance the optical transition rate because the electron and hole get close each other and lead large transition matrix element. The size of exciton, exciton Bohr radius a_B is written by

$$a_B = a_H \frac{m_0}{\mu} \frac{1}{\varepsilon_0} n^2, \quad (\text{Eq. 2.15})$$

where a_H is Bohr radius of hydrogen atom. The sharp excitonic features appear as a pronounced absorption peak as shown in Figure 2.14b. In the absorption spectrum, the discrete peaks are observed, which is attributed to excitonic resonance of $n = 1, 2, \dots$ hydrogen-like Rydberg series. The exciton binding energy E_b corresponds to the separation between the energy of band edge ($n = \infty$) and $n = 1$ excitonic absorption peak. In other words, the binding energy corresponds to the energy difference between the bound exciton and free electron-hole pair states. This type of optical transition is observed in the band edge of TMDs.

Since the electrons of monolayer TMDs are confined in extremely thin quantum well, the Coulomb interaction is strongly enhanced. The consequence of exciton formation can dominate optical and charge-transport properties. The excitonic properties of 2D monolayer differ from a 3D bulk semiconductor. A schematic

real-space image of excitons is given in Figure 2.15a. In contrast to the bulk semiconductor, the exciton in 2D monolayer is strongly confined and experiences reduced screening due to the change in the dielectric environment.¹¹⁵ Figure 2.15b displays schematic optical absorption spectra for the 3D bulk and 2D monolayer. It follows that the bandgap is expected to increase for the monolayer and the electron-hole interaction is expected to increase the exciton binding energy. It has been reported that the extreme enhancement of Coulomb interaction in the monolayer lead an obvious deviation departure from the conventional hydrogen-like Rydberg series of energy levels of the excitonic states.¹¹⁵

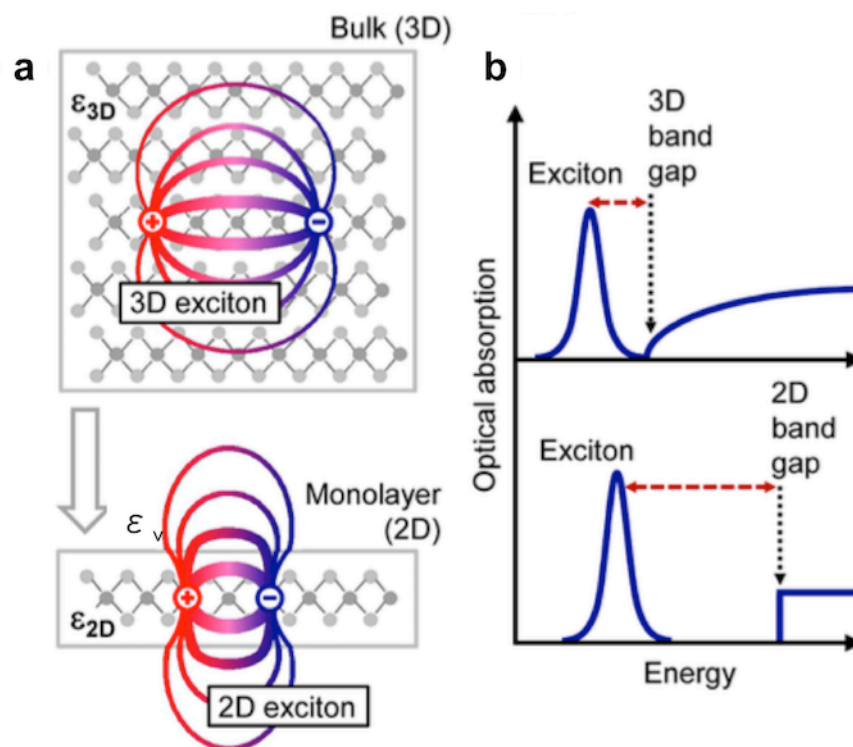


Figure 2.15 (a) Schematic real-space image of electron and hole bound into excitons for the 3D bulk and 2D monolayer TMDs MX_2 . The changes in the dielectric environment are indicated schematically by different dielectric constant ϵ_{3D} and ϵ_{2D} and by the vacuum permittivity ϵ_v . (b) Schematic optical absorption spectra for the 3D bulk and 2D monolayer. The red dashed lines indicate the exciton binding energy. (Reproduced from Ref. ¹¹⁵)

2.5. Fundamental optical properties of atomically thin layers

2.5.1. Graphene and chemically derived graphene

Density of states of graphene

The density of states (DOS) for graphene close to the Dirac point per unit cell is given by¹⁰³

$$\rho(E) = \frac{2A_c}{\pi} \frac{|E|}{v_F^2}, \quad (\text{Eq. 2.16})$$

where A_c is the unit cell area given by $A_c = 3\sqrt{3}a^2/2$ and v_F is the Fermi velocity. Figure 2.16 shows (a) DOS per unit cell as a function of energy computed from the energy dispersion, and (b) the zoom of the DOS close to the neutrality point. It is worth noting that the DOS of graphene is linearly dependent on E and zero at Fermi level E_F , which indicate that graphene is zero gap material. This character makes graphene unique compared to other 2D materials mentioned in Section 2.1.

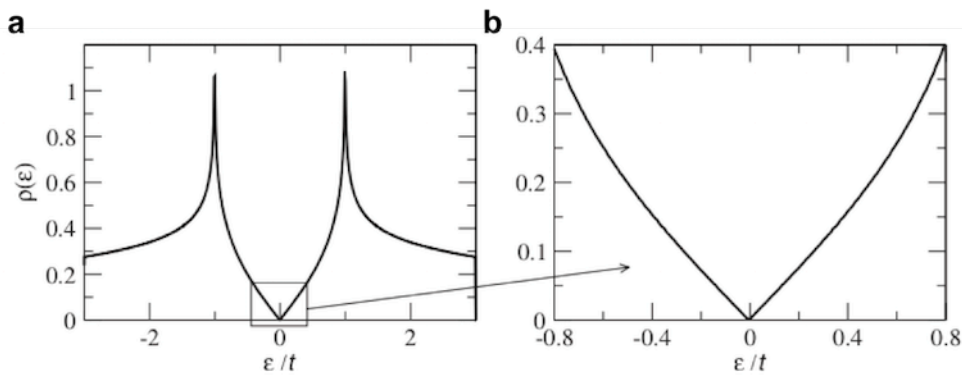


Figure 2.16 (a) DOS per unit cell as a function of energy computed from the energy dispersion. (b) Zoom of the DOS close to the neutrality point. (Reproduced from Ref.

Optical transition of graphene

Graphene has been theoretically predicted that its absorbance is independent of excitation energy and universal values is equal to $\pi\alpha = 2.3\%$ per layer due to the interband transitions in the linear dispersion of energy band structure.^{76, 116-118} These prediction have been confirmed over near infrared–visible region by optical reflectivity and transmission measurements.^{75, 76} Figure 2.17a shows the absorbance as a function of photon energy for three different graphene samples in the range of 0.5-1.2 eV. The three samples exhibit equivalent optical response. The absorbance is spectrally flat within $\pi\alpha$ (1 ± 0.1). The absorption originates from the direct transition as shown in Figure 2.17b, in which electrons from the valence band are excited into empty states in the conduction band through direct transitions. The absorbance of 2.3% might seem small, but it is indeed strong absorption if we consider that graphene consists of extremely thin carbon sheet with only one atom thickness. The ability to detect light over broad spectral range is a great potential for technical demands toward imaging, sensing, and ultra-broadband photodetectors.^{119, 120} The ultra-broadband absorption of graphene will enable to combine the previously separated wavelength regimes detected by existing different kinds of semiconductors with appropriate bandgaps such as Si for visible, InGaAs for NIR, and HgCdTe for IR detections.

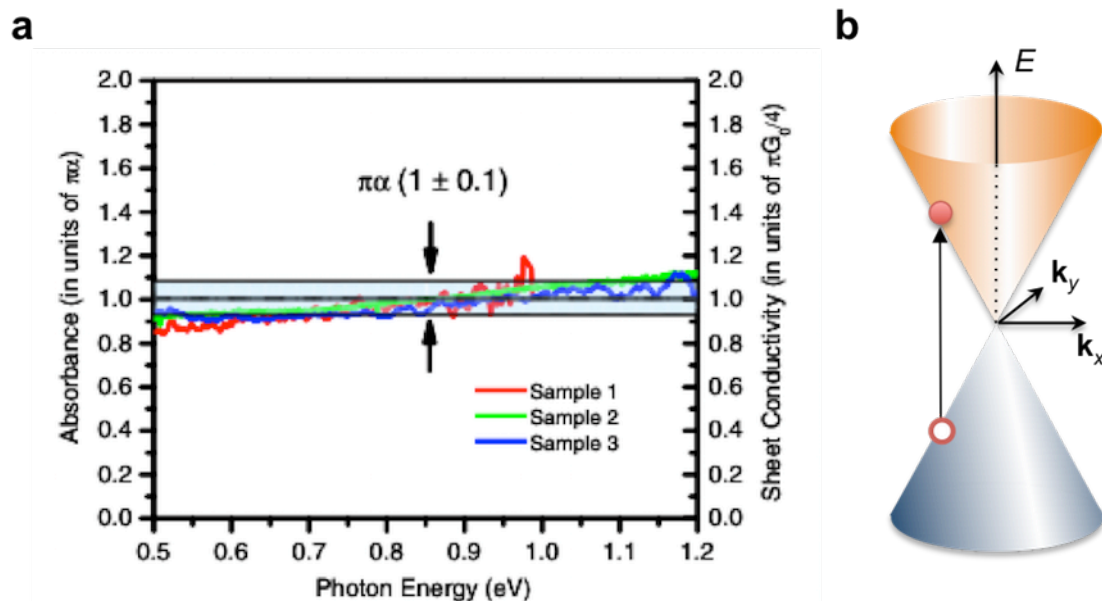


Figure 2.17 (a) Absorption spectra of different three graphene samples. The right axis indicates the corresponding optical sheet conductivity in units of $\frac{\pi}{4}G_0 = 6.08 \times 10^{-5}$ S.

The black horizontal line corresponds to the universal result of an absorbance of $\pi\alpha = 2.293\%$ within a range indicated of $\pm 0.1\pi\alpha$. (Taken from Ref. ⁷⁵). (b) Schematic band structure of the Dirac cone where the arrow shows optical transition in graphene. (Reproduced from Ref. ⁷⁶)

Tunable photoluminescence from GO

The inhomogeneous chemical and electronic structures of GO provide ability for tailoring optical properties as well as electrical properties, although the insulating and defective nature of GO does not allow the observation of unique physical phenomena obtained from graphene. The research interest of GO is shifting from a precursor of graphene to a new-class optoelectronic material. The most notable optical phenomenon in GO is luminescence, while the absence of energy gap in graphene implies no luminescence unless assisted by phonons.^{121, 122} The observation of PL from GO has

been reported for NIR to blue region.^{39-41, 80, 123, 124} The energy gap of GO can be tuned by chemical or thermal reduction to increase the ratio of sp^2 to sp^3 fraction. Figure 2.18 shows photoluminescence excitation intensity (PLE) maps of GO and broad range PL is observed around 750 nm.⁴¹ A progressive chemical reduction by hydrazine modifies the emission spectrum to longer wavelength. The PLE maps display remarkable redshift of emission wavelength center from 700 to 900 nm by increasing exposure time of hydrazine vapor (Figure 2.18). This chemical reduction by hydrazine leads GO to manipulate the energy gap.

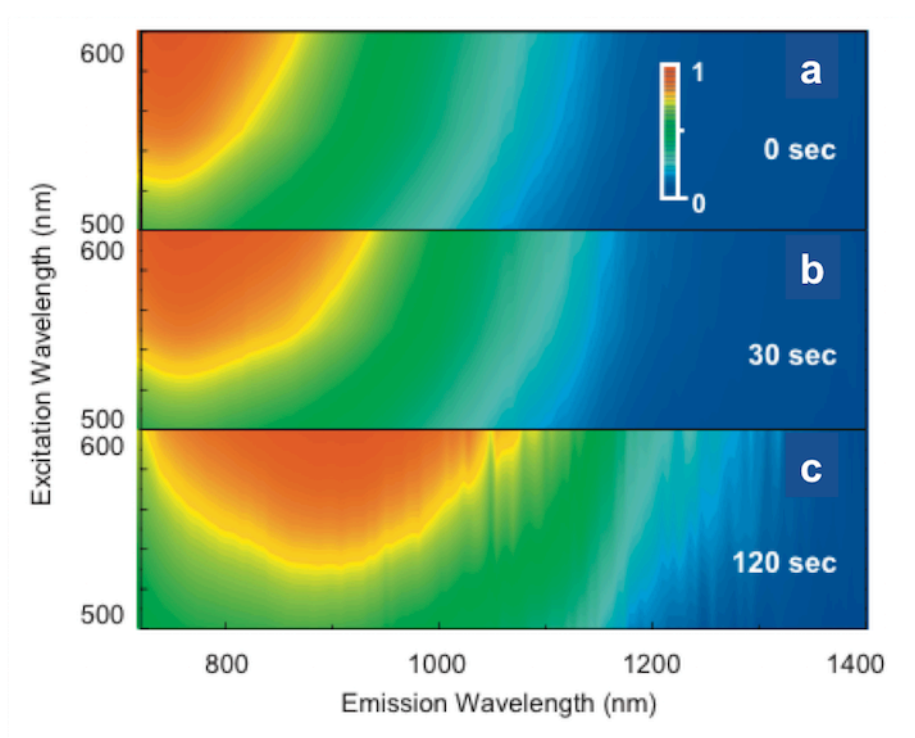


Figure 2.18 PLE intensity maps for GO deposited on substrates with varying exposure time of hydrazine vapor for 0-120 s. The vertical and horizontal axes show excitation and emission wavelength. (Reproduced from Ref. ⁴¹)

2.5.2. Transition metal dichalcogenides

Density of states

Since TMDs have parabolic energy dispersion, their features of DOS follow that of conventional 2D materials in contrast to graphene.¹²⁵ Figure 2.19a shows electronic band structure (left) and DOS (right) of monolayer MoS₂ calculated using *ab initio* density functional theory (DFT). The energy difference between the CBM and VBM, corresponding to the bandgap, is smallest at K point, which indicates that monolayer MoS₂ is a direct gap semiconductor. The VHS gives rise to step-like features of the DOS at K point. The higher DOS at higher energy region of the conduction band and lower energy region of the valence band is other origin, which is explained in detail in Section 5.6. Pronounced absorption peaks from excitonic transitions are observed as shown in Figure 2.19b.^{49, 50, 54} The two peaks are known as the A and B excitons, associated with the splitting of the valence bands due to the large spin-orbit interaction as mentioned in Section 2.3.2.

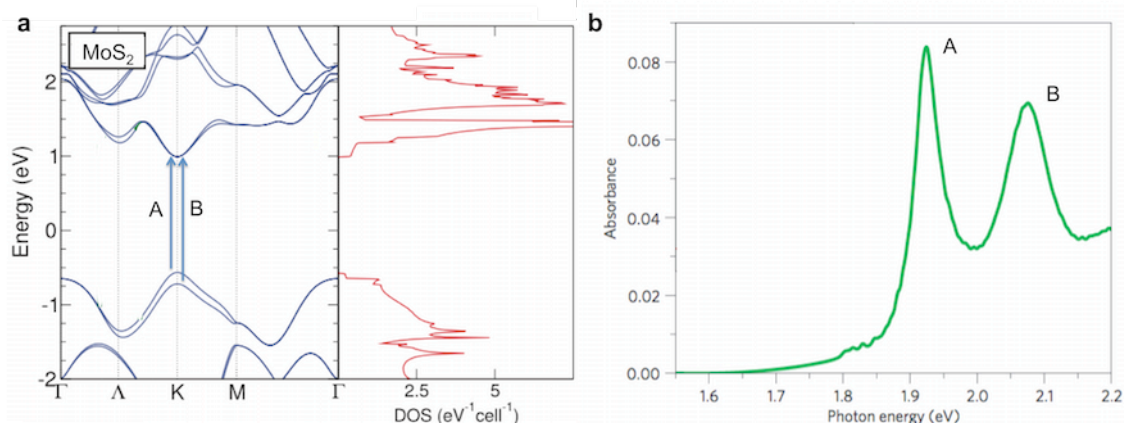


Figure 2.19 (a) Band structure and DOS of monolayer MoS₂. The two arrows correspond to direct transition for resonance with A and B excitons. (Reproduced from Ref. ¹²⁵) (b) Absorption spectrum of MoS₂ with two distinct peaks known as A and B excitons. (Reproduced from Ref. ⁵⁴)

Photoluminescence

The electronic structures of MoS₂ drastically change depending on their thickness (or the number of layers). The PL feature looks obviously different between monolayer and bilayer MoS₂ (Figure 2.20a).⁵⁰ The PL quantum yield decreases steadily with the layer number from $\sim 10^{-2}$ to $\sim 10^{-6}$ for monolayer to six layers (inset of Figure 2.20a). Figure 2.20b shows the normalized PL spectra for monolayer to six layers MoS₂. The Monolayer MoS₂ shows PL feature of A peak and weak B peak, while few layers MoS₂ shows three PL features labeled as A, B, and I. The A and B peaks are attributed to an exciton recombination at the direct gap, and the I peak is attributed to phonon-assisted emission at the indirect gap between Γ and Λ points.^{49, 50} B peak in the PL spectra is known to originate from B exciton hot luminescence.⁵¹ The A peak of the monolayer MoS₂ has narrow linewidth of 50 meV and is centered at 1.90 eV. The B peak lies about 150 meV above the A peak, and these two peaks have small red shift with increasing the layer number. The broad I peak feature lies below A peak and steadily shifts to lower energy and becomes less pronounced with increasing the layer number as shown in Figure 2.20b. Figure 2.20c shows the lowest energy of the PL peaks as a function of the layer number. The peak energy of monolayer MoS₂ is at 1.9 eV and decreases steadily with the layer number down to 1.3 eV at six layers. It should be noted that the energy of PL does not correspond to the bandgap of MoS₂. This is because the emission originates from excitonic luminescence and it includes the binding energy of the exciton estimated to be 0.9-1.1 eV by theoretical calculations for monolayer MoS₂¹²⁶⁻¹²⁹. Therefore, the PL is expected to exhibit at 0.9- 1.1 eV lower than the bandgap energy.

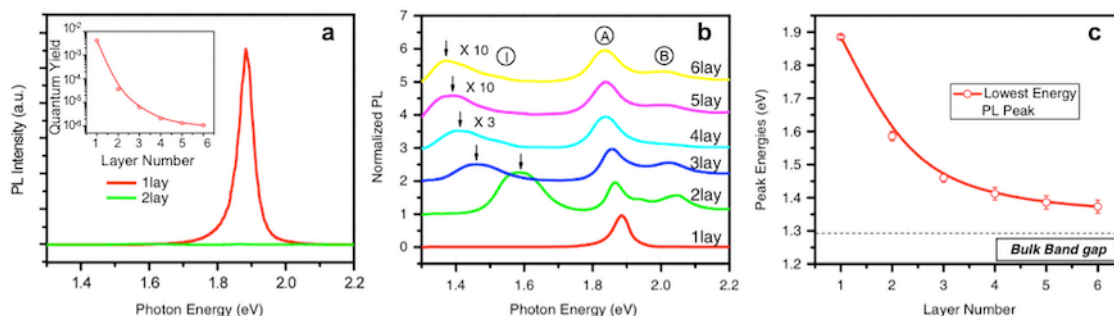


Figure 2.20 (a) PL spectra for monolayer (1 lay) and bilayer (2 lay) MoS₂. The inset shows PL quantum yield as a function of the number of layers (N). (b) Normalized PL spectra by the intensity of emission peak A. Feature of indirect I peak for $N = 4-6$ is magnified and the spectra are vertically displaced for clarity. (c) The lowest energy of PL peak for MoS₂ as a function of the layer number. (Taken from Ref. ⁵⁰)

2.6. Fundamental electrical properties of atomically thin layers

Optoelectronic devices are electronic devices that can harvest or emit light. The atomically thin 2D sheets have extensively studied for use in optoelectronic devices exploiting their flexible and transparent characteristics. Here a manifestation of promising electrical device properties of the materials is introduced in following Sections.

2.6.1. Graphene and chemically derived graphene

Graphene

A pronounced ambipolar electric field effect is observed in graphene due to the facile modulation of a location of the Fermi level (Figure 2.21b).^{5, 130} When the Fermi level locates at the K (or K') point, the valence band is almost full of electrons and the conduction band is almost empty, which lead a low concentration of carriers (electrons or holes). The Fermi level of graphene can easily shift by changing the gate voltage V_g

in the devices. Its conductivity σ shows minimum at $V_g = 0$ or the Dirac point, and increases linearly with increasing gate voltage V_g for both polarities. The charge carrier can be tuned continuously between electrons and holes in concentrations n as high as 10^{13} cm^{-2} by varying V_g and their mobility μ can exceed $15,000 \text{ cm}^2 \text{ V}^{-1} \text{ s}^{-1}$,^{5, 6, 24, 102} which is much larger than existing semiconductors such as that of Si ($1,400 \text{ cm}^2 \text{ V}^{-1} \text{ s}^{-1}$ for electron and $450 \text{ cm}^2 \text{ V}^{-1} \text{ s}^{-1}$ for hole) and GaAs ($8,500 \text{ cm}^2 \text{ V}^{-1} \text{ s}^{-1}$ for electron and $400 \text{ cm}^2 \text{ V}^{-1} \text{ s}^{-1}$ for hole).¹³¹ This extremely high mobility is because of the massless characteristics of the carriers originating from the linear band dispersion, where the carrier mobility is proportional to reciprocal of effective mass. Surprisingly, the mobility achieves in excess of $200,000 \text{ cm}^2 \text{ V}^{-1} \text{ s}^{-1}$ for the suspended graphene, suggesting that the presence of strong impurity scattering limits the mobility of graphene devices deposited on the substrates.^{16, 132} The extraordinary carrier mobility makes graphene attractive as the channel material for high-frequency field effect transistors..

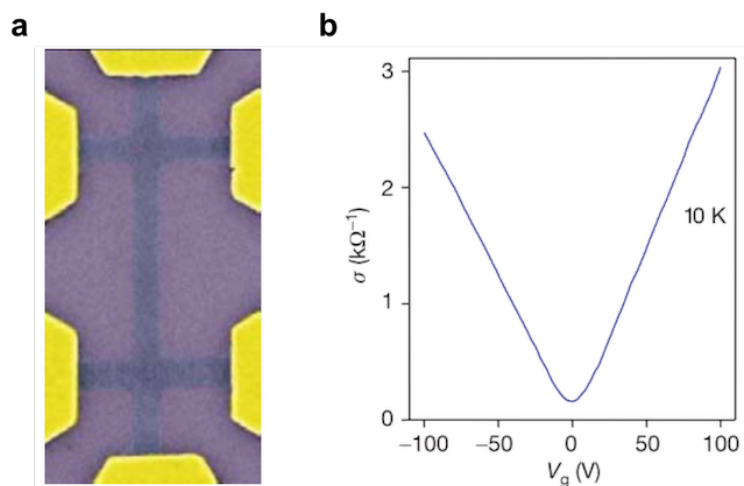


Figure 2.21 (a) Scanning electron microscope image of graphene devices on a SiO_2/Si substrate. Graphene films were further processed into multi-terminal devices for Hall measurements. (b) Conductivity as a function of gate voltage measured at 10 K. (Reproduced from Ref. ⁵)

Chemically derived graphene

Well-reduced GO devices also have the ambipolar characteristics (Figure 2.22),^{7, 32, 78, 133}, which is similar characteristics to that of graphene devices. Their mobility reaches $365 \text{ cm}^2 \text{ V}^{-1} \text{ s}^{-1}$ ¹³⁴ which is applicable level to organic electroluminescence displays ($> 10 \text{ cm}^2 \text{ V}^{-1} \text{ s}^{-1}$), although a typical values is as much as $10 \text{ cm}^2 \text{ V}^{-1} \text{ s}^{-1}$, depending largely on film thickness and reduction conditions, which is comparable level to that of organic transistor. Residual oxygen and defects in the structures severely limit the carrier transport in GO.¹³⁵ Lightly reduced GO has a finite energy gap and exhibits pronounced switching behavior with higher on/off ratio exceeding 10^3 at low temperatures.^{32, 77} With increasing reduction level, reduced GO reaches the zero-gap limit, leading to moderate on-off ratio, while the field effect mobility improves.

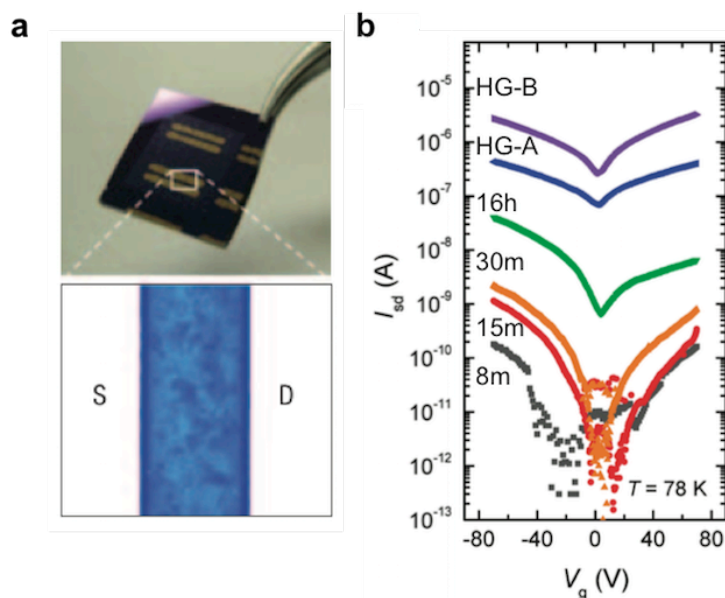


Figure 2.22 (a) Photograph of thin film transistor device based on GO with source and drain electrodes. (Reproduced from Ref. ⁷) (b) Source-drain current as a function of gate voltage measured at different temperatures. The labels, 8m, 15m, 30m, 16h (m = minutes, h = hours) correspond to total time of exposure to hydrazine monohydrate

vapor. HG-A and HG-B correspond to GO directly reduced in anhydrous hydrazine with annealing in forming gas at 150 °C. (Reproduced from Ref. ³²)

Electrical conduction depends on the reduction level of GO.³² GO undergoes insulator, semiconductor, and semimetal transitions with reduction. The carrier transport in reduced GO predominantly occurs via variable-range hopping¹³⁶ and further reduction leads to an increased number of available hopping sites. Figure 2.23 shows the plot of conductivity of GO film as a function of sp^2 -carbon fraction obtained by X-ray photoelectron spectroscopy (XPS). The extrapolation of the experimental data indicate that reduced GO can achieve comparable conductivity of polycrystalline graphite ($1.25 \times 10^3 \text{ S cm}^{-1}$)¹³⁷ at a sp^2 fraction of ~ 0.87 for reduced GO. At higher sp^2 fractions, percolation among the sp^2 clusters dominates the transport with a reasonable agreement with the theoretical threshold values for conduction among 2D discs.¹³⁸

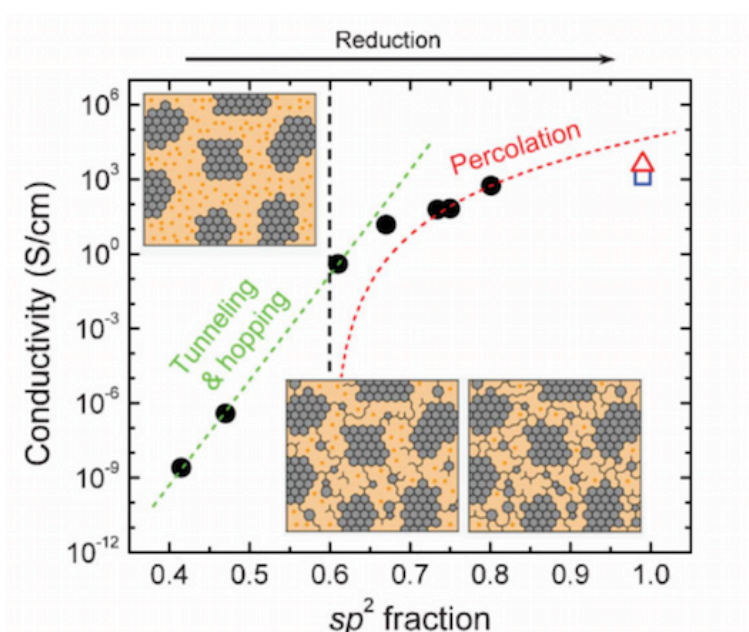


Figure 2.23 Conductivity of thermally reduced GO as a function of sp^2 carbon fraction obtained from XPS. The conductivity values for $\sim 100\%$ sp^2 carbon, namely polycrystalline graphite (square) and graphene (triangle), are plotted for comparison. The inset shows schematic image of the sp^2 clusters (gray) and sp^3 bonded carbon

regions (orange). (Reproduced from Ref. ³²)

2.6.2. Transition metal dichalcogenides

Two-dimensional transition metal dichalcogenides (TMDs) play a complementary role to graphene. Graphene transistors exhibit low on-off ratio because of the lack of a bandgap in graphene. In contrast, TMDs possess sizable bandgaps depending on the combination of elements, promising new electronic or optoelectronic devices. The first detailed demonstration of a monolayer TMDs transistor has been reported by Kis and co-workers.¹⁵ Current-voltage curves for the field effect transistor based on the monolayer MoS₂ is shown in Figure 2.24 with the schematic device structure. They demonstrate the excellent on-off ratio of 1×10^8 at room temperature. The devices show n-type channel behavior. The HfO₂ layer has high dielectric constant κ of 25, bandgap of 5.7 eV, and works as a mobility booster to realize the full potential of the monolayer MoS₂. The recent report provides that the low temperature mobility of MoS₂ transistor is up to $500 \text{ cm}^2 \text{ V}^{-1} \text{ s}^{-1}$.^{139, 140}

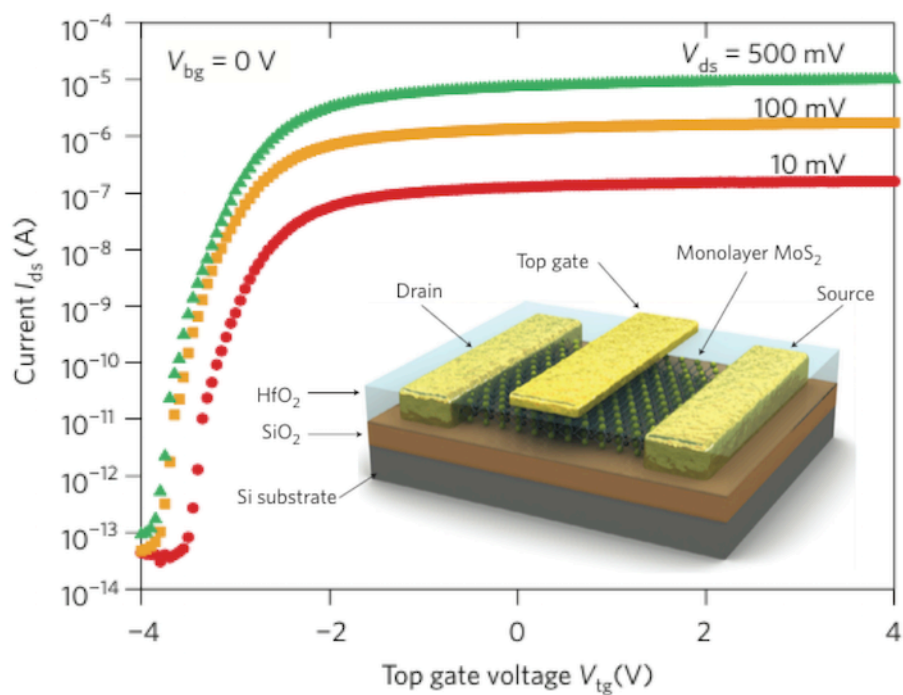


Figure 2.24 Drain-source current as a function of gate voltage measured at room temperature with the back gate grounded. The inset shows schematic view of MoS_2 transistor. The monolayer MoS_2 is covered by 30 nm of atomic-layer-deposition HfO_2 that acts as a gate dielectric and a mobility booster. (Reproduced from Ref. ¹⁵)

Chapter 3. Quasi-molecular blue and ultraviolet photoluminescence graphene oxide

3.1. Introduction

In this Chapter, we describe the manifestation of blue and UV photoluminescence (PL) and clarify the mechanism of PL from graphene oxide (GO).

The optical and electrical properties of GO are determined by π states of the sp^2 domains. The π and π^* electronic levels of the sp^2 clusters is within the energy gap of σ and σ^* states of the sp^3 matrix and are strongly localized.^{36, 37, 39} While the energy gap depends on the size of the sp^2 domains, the clarification of the luminescence mechanisms of GO is still controversial. due to the non-stoichiometric and inhomogeneous structures of GO. Possible major models of the luminescence are suggested that quasi-molecular luminescence from fragments that consists of 240 carbon atoms and oxygen functional groups for both blue and NIR PL,¹⁴¹ and the electron-hole recombination among the small sp^2 fragments for blue PL and luminescence from disorder states for red to NIR PL.^{39, 80} The study in this thesis shows that such large luminescent species consisting of 240 carbon atoms exhibit NIR PL and no longer behave like quasi-molecular, which discussed in Chapter 4. The NIR luminescence from the disorder states cannot fully explain the excitation-dependent PL that we have observed (discussed in Chapter 4).

First we tackle the challenge of revealing the origin of blue and UV emission from relatively small sp^2 fragments. The presence of molecular-like sp^2 domains has been suggested in transport studies of GO³² and PL from amorphous carbons¹⁴² and also from GO.^{39, 141} To clarify possible size and chemical structure of luminescent species of GO

provides a guideline for modulation of the structure to tune the luminescence properties. The tunability of luminescence wavelength is one of attractive characteristics in GO. We demonstrate that GO exhibits UV luminescence not only blue bands, which opens up new potential for optoelectronic applications of blue and UV light emitting devices.

In this Chapter, we study the blue and UV PL mechanism of GO by combining various experimental approaches of continuous-wave (cw) and time-resolved spectroscopy. The pH and photochemical reduction process dependence of PL spectra were examined. We found that highly exfoliated GO in aqueous solution exhibits PL peaks in ultraviolet (UV) and blue spectral regions. The PL spectra peaks, PL lifetimes, and their pH-dependencies are closely coincident with those of aromatic compounds with oxygen functional groups, which suggests that the PL peaks come from the small number of aromatic ring structures with oxygen functional groups embedded in the GOs as shown in Figure 3.1.

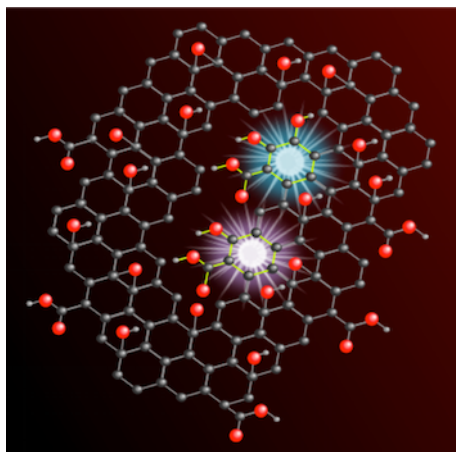


Figure 3.1 Schematic image of quasi-molecular luminescence species consisting of the small number of aromatic ring structures with oxygen functional groups embedded in the GOs. The grey, red and white dots represent carbon, oxygen and hydrogen atoms, respectively. The green lines indicate the main frame of the quasi-molecular states.

3.2. Sample preparations

Aqueous dispersions of GOs (highly concentrated graphene oxide dispersion in water, purchased from Graphene Supermarket) produced by modified Hummer's method were used in this study. The GO dispersions were centrifuged at 35,000 g for more than 10 h, and the supernatant was used for measurements to study optical properties of single-layered GOs.¹⁴³ The pH of the GO dispersions was controlled using sodium hydroxide (Wako 1st Grade, purchased from Wako Pure Chemical Industries, Ltd.) solution. A Xe lamp (Zolix, LSH-X150, 150W) with an IR cut filter (cut-on wavelength: 700 nm) was used for the GO reduction process. The chemical structural formula and photographs of used aromatic compounds are displayed in Figure 3.2. All the sample solutions look transparent. Phenol (Chameleon Reagent, Kishida Chemical CO., LTD.), benzoic acid (JIS Special Grade, Wako Pure Chemical Industries, LTD.), salicylic acid (Chameleon Reagent, Kishida Chemical CO., LTD.), phthalic acid (Chameleon Reagent, Kishida Chemical CO., LTD.), and 1-naphthoic acid (Wako Special Grade, Wako Pure Chemical Industries, LTD.) were used for the measurement.

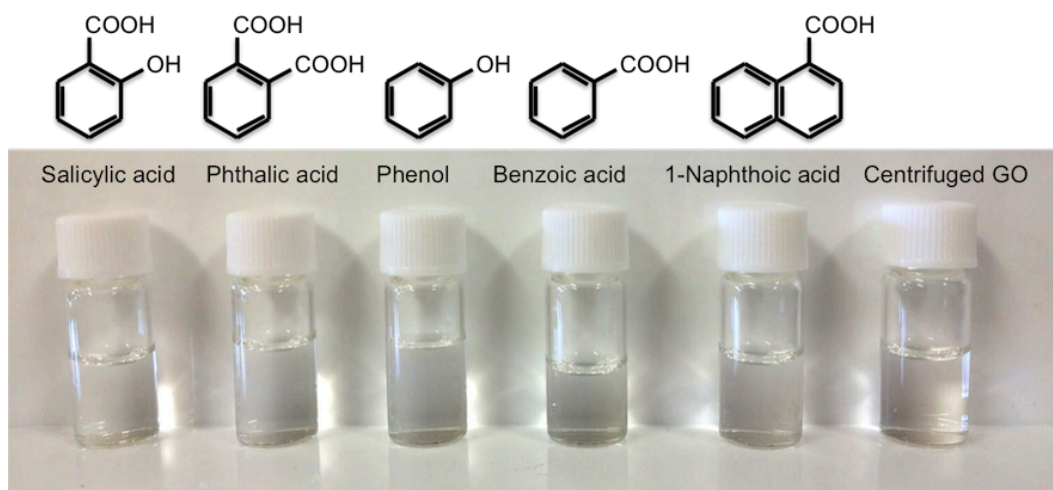


Figure 3.2 Chemical structural formula and photographs of salicylic acid, phthalic acid, phenol, benzoic acid, and 1-naphthoic acid. The centrifuged GO as displayed for reference.

3.3. Experimental methods

3.3.1. Light absorption measurements

Absorption spectra were measured using a UV-vis spectrophotometer (Shimadzu, UV-1800) shown in Figure 3.3. In the spectrophotometer, the excitation light source is a combination of deuterium (D_2) lamp and halogen lamp. The D_2 lamp and halogen lamp were employed in 200-340.8 nm and 340.8-1100 nm. White light from the lamps is cut into monochromatic light at the diffraction grating and split into two paths at the beam splitter. One path goes to the photodiode for the solution sample and the other path goes to the reference photodiode. Scanning the grating i.e. varying the excitation wavelength, the ratio of the light intensity transmitting through the sample and reference was measured to obtain absorption spectra. The scan rate of the grating was set as “middle speed” and the sampling pitch was set as 1 nm interval. The absorption measurements need the absorption spectrum of the solvent as a baseline and we used the same solvent as the sample solution to obtain the baseline.

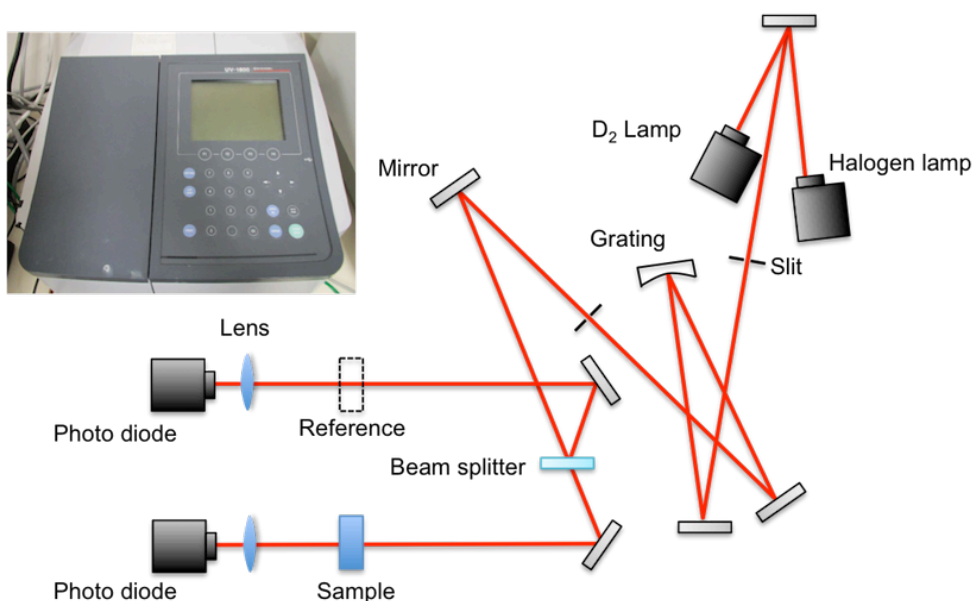


Figure 3.3 Photograph and schematic optical alignment of the UV-vis spectrophotometer.

3.3.2. PL and PLE measurements

The PL and PL excitation (PLE) spectra were obtained using a fluorescence spectrophotometer (Shimadzu, RF-5300PC) shown in Figure 3.4. The excitation light source is white light of Xe lamp and cut into monochromatic light at the diffraction grating. The monochromatic light is split into two beams, going to the sample and to the reference photodiode to monitor the excitation light. The PL is collected in the photomultiplier tube after the luminescent light is dispersed at the diffracting grating. The scan rate of the grating was set as “fast” and the sampling pitch was set as 1 nm interval. The slit was typically set as 5 nm bandwidth for the excitation side and as 10 nm bandwidth for the detection side. Color glass filters (long pass above 320, 435 and 610 nm, Edmund Optics, UV N-WG320 50MM, and Thorlabs, FGL435S and FGL610S, respectively) are used at the detecting side to remove the second order light caused by the Rayleigh scattering in the diffraction grating. The relative PL intensity was corrected for instrumental validations in excitation intensity and detection sensitivity using the standard lamps (Ocean Optics, LS-1-CAL). In the PLE spectroscopy, the energy of excitation light is varied and certain luminescence is monitored. The PLE intensity is mainly proportional to absorption and carrier recombination rates. This spectroscopy reveals electronic level structures of materials because the light of particular excitation energy can efficiently excite resonant energy states.

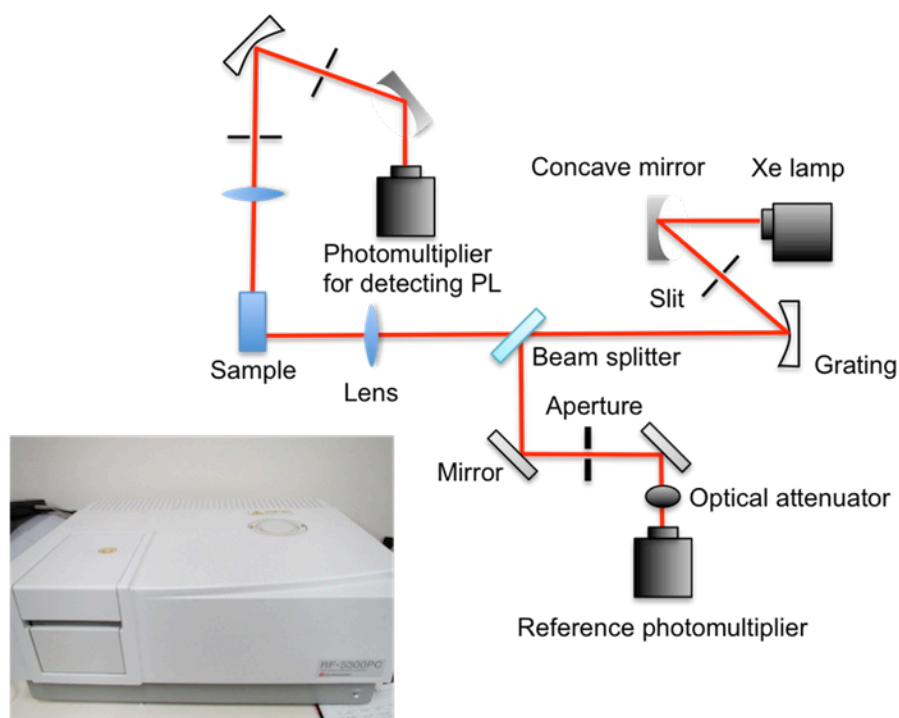


Figure 3.4 Photograph and schematic optical alignment of the fluorescence spectrophotometer.

3.3.3. Raman measurements

Raman spectra were obtained using a Raman spectrophotometer (Renishaw, inVia Raman Microscope) with a 100X magnification objective lens (Leica, N PLAN 100X, numerical aperture 0.90) shown in Figure 3.5. The sample of GO was prepared by drop casting of the GO solution on SiO_2/Si substrates. The excitation light source is the diode laser with 2.33 eV photon energy. The sample was optically excited with 400 μW laser power for 60s. The diffraction grating has 1800 grooves/mm and the grating scan type was set as “extended” to scan the grating in a wide range. In Raman spectroscopy, the energy difference between the energies of incident and Raman scattering light is measured as Raman shift. The Raman scattering is induced by interaction between incident photon and phonon (or lattice vibration). The Raman shift provides the

information on lattice structures of materials.

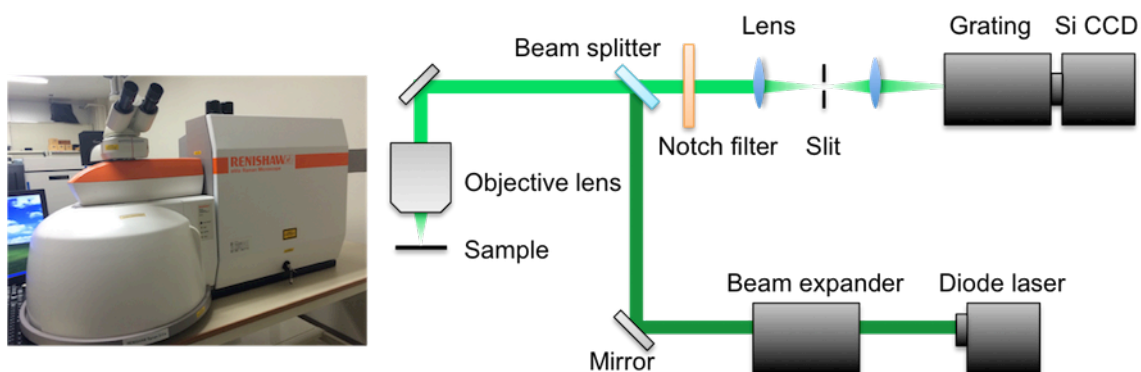


Figure 3.5 Photograph and schematic representation of the Raman spectroscopy.

3.3.4. Time-resolved PL measurements

The time-resolved PL (TRPL) spectroscopy was performed with a time-correlated single photon counting (TCSPC) module (Hamamatsu Corporation, Quantaurs-Tau C11367, provided by Prof. T. Morii). The excitation light source was light emitting diodes with 3.6 and 4.4 eV photon energy. The temporal resolution of the PL decay measurements is several hundreds of ps. The GO solution sample was used for the TRPL measurements. In the TCSPC system, time delay of single photons from sample luminescence is measured in respect to a reference signal, in which a part of excitation light is split as the reference signal. The time delay originates from recombination of photoexcited carriers. The detection of photons are repeated and accumulated to obtain statistic photon counts as a function of the time delay. This technique is often used to obtain PL lifetime of materials.

3.3.5. AFM measurements

AFM (Digital Instruments, Nanoscope IIIa), shown in Figure 3.6, was used to obtain the surface morphology of GO with cantilever probes purchased by Olympus

(OMCL-AC160TS-C3). The resonant frequency and spring constant of the AFM probes were typically ~ 300 kHz and 26.1 Nm^{-1} , respectively. The scan rate was set as 0.5 Hz per line and the number of scan lines was 256 with tapping mode. The sample for the AFM measurements was prepared by drop casting of the GO solution on SiO_2/Si substrates as well as the sample for the Raman measurements. In AFM measurements, atomic force is measured with scanning the cantilever probe. The atomic force becomes significant when the separation between the probe and atoms is small enough (typically below 1 nm). The atomic force modulates the amplitude, phase and frequency of the probe vibrations and these modulations are converted into the height of samples.

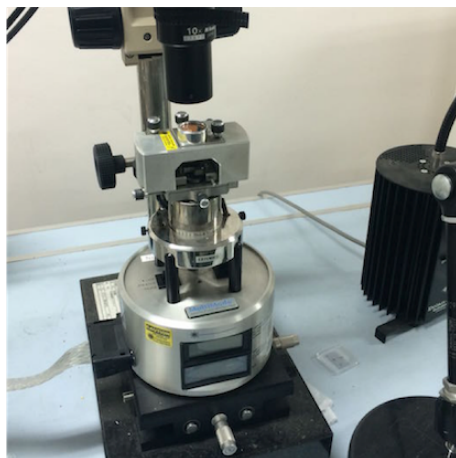


Figure 3.6 Photograph of the AFM.

3.4. Sample characterization

Figure 3.7 displays photograph of the centrifuged GO and of as-purchased GO for reference. The color of the GO solution turns closed to transparent through the centrifugation process. The Figure 3.8a-c show an atomic force microscopy (AFM) image of the GO after centrifugation treatment. Figure 3.8d is a cross sectional profile at the line labeled by 1 in Figure 3.8c. Typical lateral size and height of the GO flakes are ~ 100 nm and ~ 1 nm, respectively. The typical height of ~ 1 nm suggests that the most of the flakes are single-layered GOs.¹⁴⁴

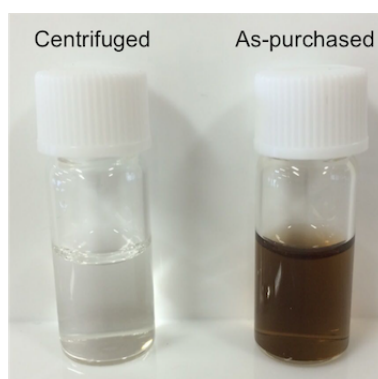


Figure 3.7 Photograph of the centrifuged GO and of as-purchased GO for reference.

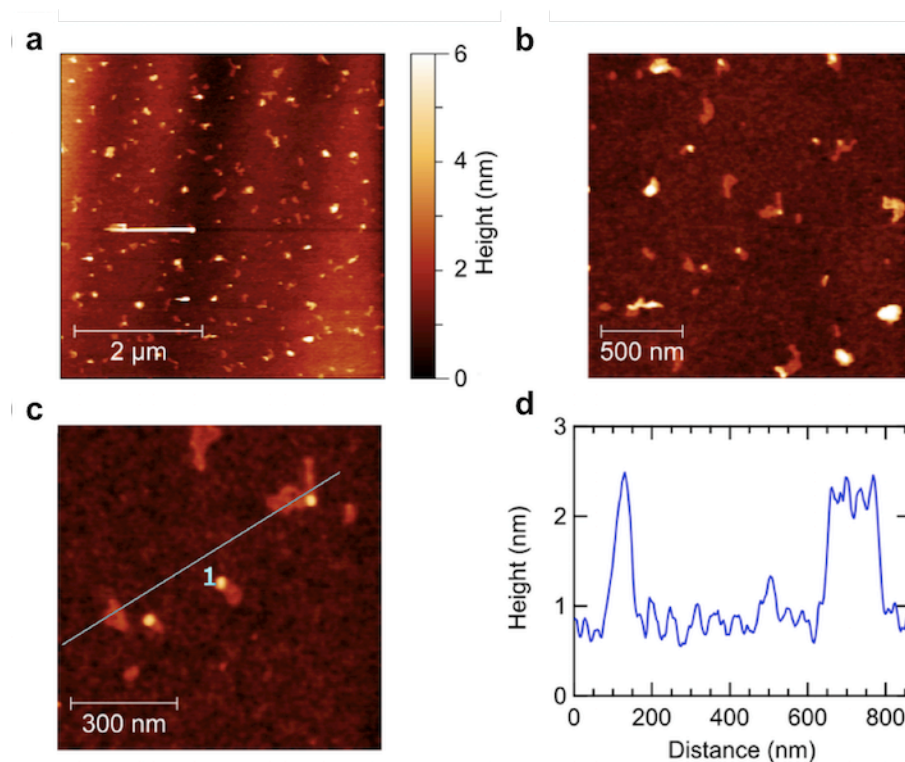


Figure 3.8 (a-c) AFM images of GOs with various magnifications. (d) Cross sectional profile on the line labeled by 1 in (c).

We also confirmed the characteristic Raman peaks such as G and D band of GO in Figure 3.9, which have been previously reported by other groups.¹²⁴ Figure 3.10 shows schematics of typical phonon scattering processes responsible for Raman modes in graphite (and also graphene) for G, G', D and D' modes. The G band (1580 cm^{-1})

originates from a primary in-plane vibrational mode, which suggests the existence of crystalline sp^2 carbons.¹⁴⁵ Both the D (1350 cm^{-1}) and D' are attributed to defect with intervalley and intravalley phonon scatterings. The D+D' mode (2950 cm^{-1}) is a combination scattering mode of the D and D'. The G' mode (2700 cm^{-1}) is second order process of intervalley scattering with two phonons, which is intrinsic mode in graphitic carbons unlike the D and D' modes.^{146, 147} The pronounced D peak indicates the presence of the crystalline imperfection because of the oxygen functional groups on the basal plane of the graphitic carbons.⁷

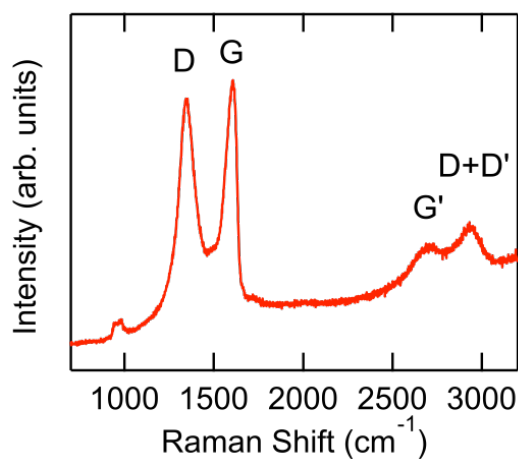


Figure 3.9 Typical Raman spectrum of GO at the excitation energy of 2.33 eV.

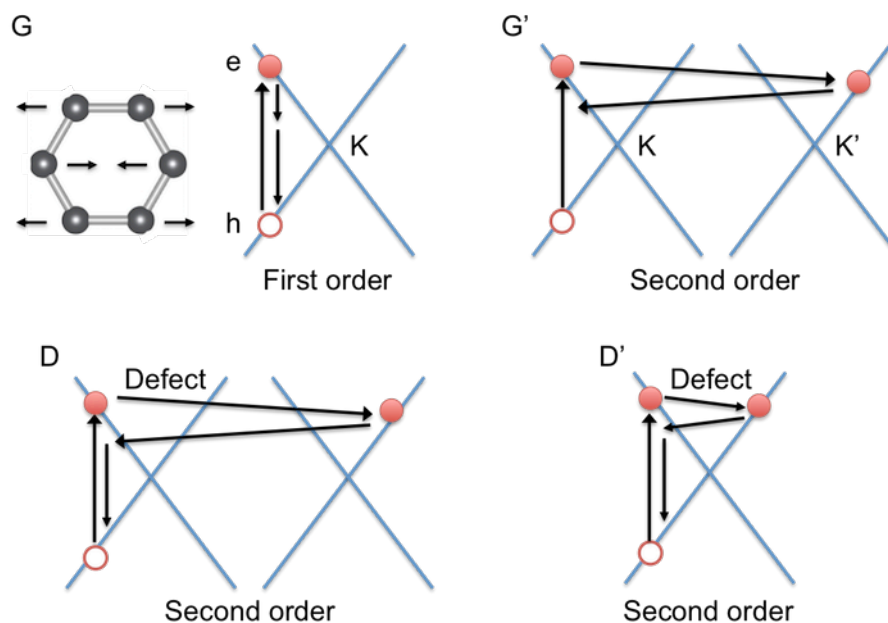


Figure 3.10 Schematics of typical phonon scattering processes responsible for Raman modes in graphite (and also graphene) for G, G', D and D' modes. The blue lines represent the energy band structures of graphene nearby K or K' points. Red dots and white circles represent the excited electron and hole. For G mode, a schematic lattice vibration is displayed where the grey dots represent carbon atoms.

3.5. Observation of blue and UV PL

Figure 3.11a shows absorption spectrum of a highly exfoliated GO in the aqueous solution at pH 6.5. The absorption intensity of the GOs gradually increases with energy. In the absorption spectrum, distinct gap and peak structures are not observed and only broad spectral structures are seen. The absorption at around ~ 5.0 eV is attributed to π - π^* transitions of C=C,³⁹ and the shoulder at approximately ~ 4.0 eV is attributed to n - π^* transitions of C=O.⁹⁰ We also measured the absorption spectra of GO after changing the pH from 2.5 to 11.1 as shown in Figure 3.12 and confirmed that the absorption spectra change primarily in the UV region shorter than 4.1 eV.

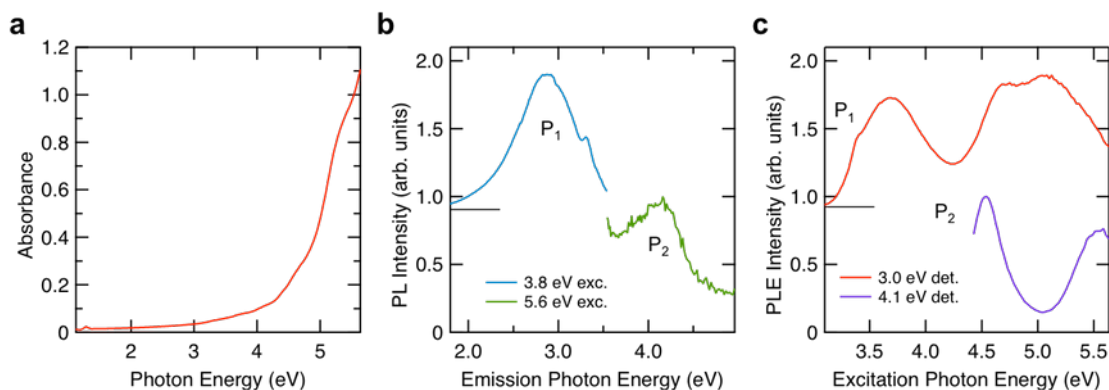


Figure 3.11 (a) Absorption spectra of GOs dispersed in aqueous solution at pH 6.5. (b) Typical PL spectra of GOs excited with 3.8 and 5.6 eV and (c) PLE spectra detected at 3.0 and 4.1 eV. The horizontal lines on the right show the offset.

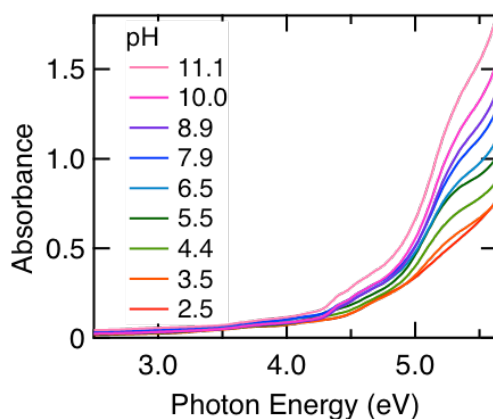


Figure 3.12 Absorption spectra of GOs in the aqueous solution at various pH conditions from pH 2.5 to 11.1.

Figure 3.11b shows typical PL spectra of GOs in aqueous solution at pH 2.5 excited¹⁴⁸ with 3.7 and 5.6 eV light. The two distinct PL peaks at ~ 2.8 and ~ 4.1 eV, indicated by P_1 and P_2 , are observed. The P_1 emission is similar to the previously reported peak in GO.^{39, 80, 148} The P_2 emission in the UV region has not been reported previously. Note that we observed both blue (P_1 : ~ 2.8 eV) and UV (P_2 : ~ 4.1 eV) PL of the highly exfoliated GO without any reduction processes. Previously, only the blue PL

in reduced GO has been reported.^{39, 80, 148} In PLE measurements, PL was detected with varying excitation energy. PL intensity in the measurements can be described by

$$I_{\text{PL}} = P_{\text{abs}} \cdot P_{\text{rel}} \cdot P_{\text{rec}} \cdot I_{\text{ex}} , \quad (\text{Eq. 3.1})$$

where P_{abs} , P_{rel} , P_{rec} , I_{ex} are absorption rate, relaxation rate, recombination rate, and excitation intensity. PLE spectroscopy enables a selective excitation to particular sites with resonant optical gap. This spectroscopy is a powerful tool to detect specific states in homogeneous systems such as GO and quantum dots.^{149, 150} Figure 3.11c shows PLE spectra monitored at emission energy of ~ 3.0 eV (P_1) and ~ 4.1 eV (P_2). The PLE spectra exhibit distinct peak structures and differ from the absorption spectra shown in Figure 3.11a, which suggests that the dominant light absorbing species in the GO do not show PL. The PLE spectra of P_1 (~ 2.8 eV) and P_2 (~ 4.1 eV) show excitation peaks at 3.7, 4.7, and 5.2 eV (orange curve), and at 4.6 and 5.6 eV (purple curve), respectively.

Figure 3.13a-c show PL intensities as a function of excitation and emission energy (two-dimensional PLE maps) of highly exfoliated GO at pH 2.5, 6.5, and 11.1, respectively. The maps are normalized by the absorption of GO at 3.7 eV. The two discrete and distinct PL peaks at ~ 2.8 and ~ 4.1 eV indicated by P_1 and P_2 are also observed in the maps. The PL intensity exhibits drastic change depending on the pH of the solvent.

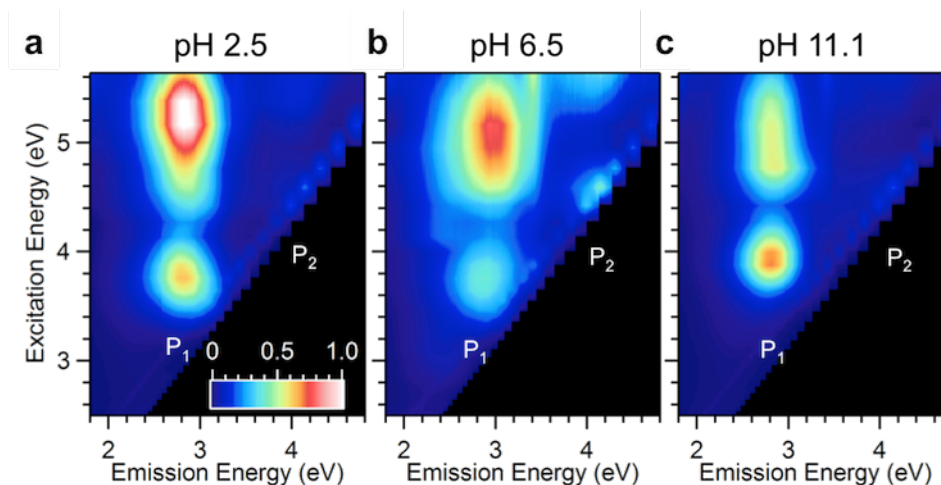


Figure 3.13 PLE intensity map of highly exfoliated GO in (a) pH 2.5, (b) 6.5, and (c) 11.1 solution, respectively. The maps are normalized by the absorption of GO at 3.8 eV.

It should be noted that GO exhibits similar PL to that of graphene quantum dots (GQDs) synthesized by oxidation of carbon fiber (Figure 3.14).^{151, 152} The blue and UV PL of GO is similar energy of emission to that of P₁ and P₂ from GQDs, respectively. The lateral sizes of GQDs are mainly 5-10 nm and the GQDs consist of sp² carbon clusters with sp³ bonded carbon. The luminescence of both materials can be the same origin.

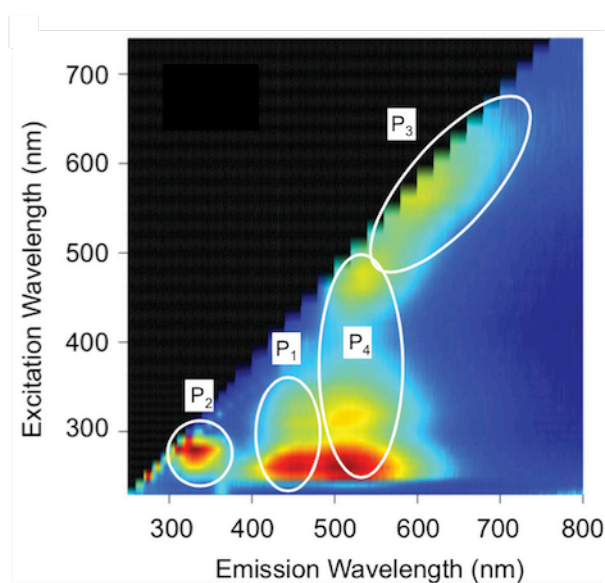


Figure 3.14 PLE intensity map of GQDs synthesized by oxidation of carbon fibers.

(Reproduced from Ref. ¹⁵²)

3.6. pH-dependent PL properties

Figure 3.15a and b show PL spectra of the GOs measured at 3.8 and 5.6 eV excitation, respectively, with pH values of the solvent from 2.5 to 11.1. The PL spectra are normalized by the absorption of GO at the excitation photon energy. The PL peak of P_1 shows a blueshift from strongly acidic (pH 2.5) to weakly acidic conditions (pH 4.4) and a redshift to basic conditions (pH 11.1). In contrast, the PL peak of P_2 shows no clear spectral shift from strongly acidic (pH 2.5) to basic conditions (pH 11.1). Figure 3.15c shows the integrated PL intensity of P_1 and P_2 peak as a function of pH. The PL intensity of P_1 exhibits nearly monotonic decrease with increasing pH from 3.5 to 8 and almost constant intensities above pH 8. The intensity of P_2 decreases monotonically from neutral to basic conditions, as shown in Figure 3.15c. The origin of the PL peaks will be discussed below based on the results from the pH-dependent PL spectra.

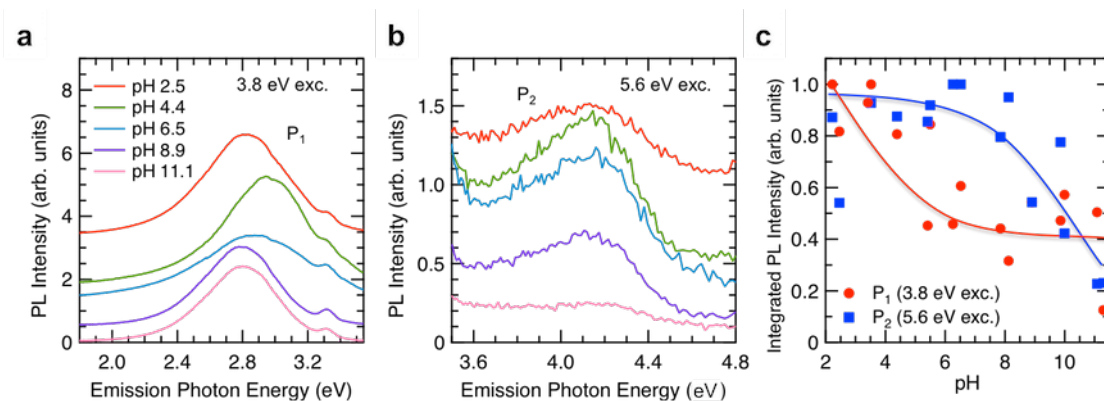


Figure 3.15 (a, b) PL spectra of P_1 and P_2 peaks in the GOs with various pH of the solvent from 2.5 to 11.1 excited at 3.8 and 5.6 eV, respectively. The horizontal lines on the right and left show the offset. (c) The integrated PL intensity of P_1 and P_2 peaks with various pH of the solvent excited at 3.8 and 5.6 eV, respectively. The red and blue lines are the eye-guides for P_1 and P_2 plots, respectively.

Quasi-molecular states¹⁴¹ are proposed as a blue and UV luminescent species of GO, which is different from simple aromatic compounds like isolated benzene or naphthalene as shown in Figure 3.16a and b, respectively. In contrast, the sp^2 domains of GO are embedded in sp^3 matrices of oxygen functional groups since the sp^3 matrices works as a potential barrier to the sp^2 domains as shown in Figure 3.16c. The sp^2 domains are sensitive to the surrounding sp^3 matrices, where the optical properties can be determined buy the size of the sp^2 domains¹⁵³ and the type of oxygen functional groups.^{154, 155} The aromatic rings of the quasi-molecular states are coupled with oxygen functional groups such as carboxyl and hydroxyl groups by covalent bonds (see Figure 3.1). The oxygen functional groups modulate the energy gap between π and π^* orbitals and also form defect states, which works to decrease PL energy.^{154, 155}

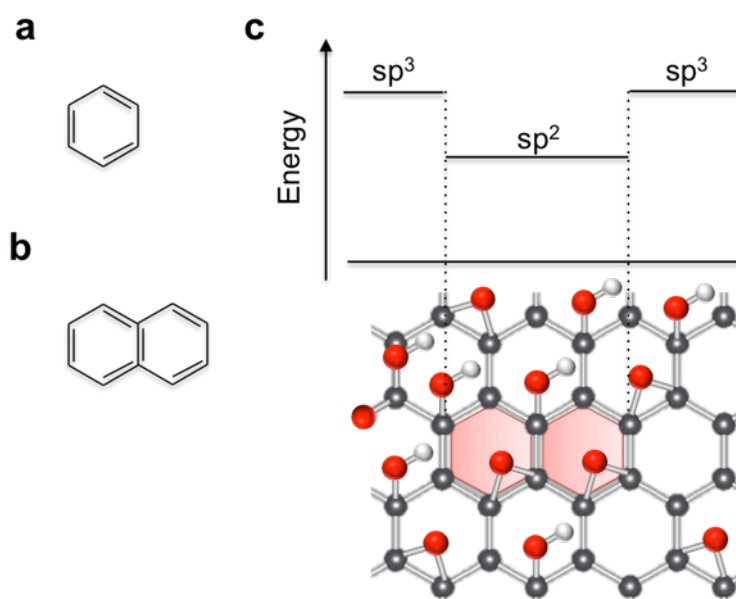


Figure 3.16 Chemical structures of (a) benzene and (b) naphthalene, which are typical aromatic compounds. (c) (top) Energy diagram of the quasi-molecular states spatially corresponding to (bottom) sp^2 domains and sp^3 matrices of oxygen functional groups in a GO atomic structure, where carbon, oxygen and hydrogen atoms are represented by grey, red, and white dots, respectively. Region of quasi-molecular states is highlighted

with red hexagon.

An important implication of the experimental observations is the similarity of the pH-dependent PL and PLE properties of GO to aromatic compounds. One possible origin of the blue (P_1) and UV (P_2) PL is the quasi-molecular PL, i.e., the quasi-molecules within sp^2 - sp^3 complexes work as PL centers embedded in sp^3 matrices of the GO. GO is a non-stoichiometric compound with various chemical structures, and the sp^2 hybrid carbons are decorated with oxygen functional groups, including hydroxyl ($-OH$), carboxyl ($-COOH$), and epoxy ($-O-$) groups.^{77, 95, 156} The PL related by such oxygen functional groups has been also discussed by some groups.^{124, 141} These functional groups and a nearby sp^2 fragment composed of a small number of benzene ring structures are related to the observed emissions in the GO.

From a calculation for the energy gap of π - π^* transitions based on density functional theory (DFT),³⁹ the gap of a single benzene ring is estimated as ~ 7.4 eV (170 nm). The energy gap drastically decreases down to ~ 2.6 eV (480 nm) for five aromatic rings with an increase of aromatic ring number and shows discrete values for fewer than five rings. With further increase of the number of aromatic rings, the energy gap changes very slowly as a function of the number of aromatic rings as described in Section 2.4.2. The experimental observation that the PL peak energy of P_1 and P_2 show discrete values suggests that the size of aromatic rings of sp^2 fragments is very small, i.e., fewer than five rings.

3.7. Comparison with molecular fluorescent species

Possible quasi-molecular electronic structures of sp^2 fragments as P_1 PL centers correspond to a benzene ring bound to several functional groups, which is similar to

hydroxybenzoic acid (for example, salicylic acid) and dicarboxybenzoic acid (for example, phthalic acid), because the emission energy of P₁ at 2.8 eV (Figure 3.11b top) is very close to that of hydroxybenzoic acid and dicarboxybenzoic acid.^{157, 158} One of the PLE peaks (3.7 eV) of P₁ (Figure 3.11c top) is almost coincident with that of hydroxybenzoic acid (3.8 eV).¹⁵⁷ In contrast, the possible quasi-molecular electronic structures of sp² fragment as P₂ PL centers correspond to a benzene ring bound to a single oxygen functional group. The benzoic acid or phenol-like structure could cause the P₂ emission at 4.1 eV (Figure 3.11b bottom) because these molecules exhibit a PL peak at 3.9-4.1 eV.^{159, 160} The PLE peaks of the first (4.6 eV) and second (5.6 eV) peak monitored at P₂ emission (Figure 3.11c bottom) are almost coincident with those of the first and second singlet-singlet transitions in benzoic acid (4.4 and 5.4 eV).¹⁶¹

Actually, we also confirmed the PL spectra of these model aromatic compounds as shown in Figure 3.17a and b, which are very similar to those of GO. Figure 3.17 shows PL spectrum of naphthoic acid, which has two-fused benzene rings with a carboxyl group. The PL of naphthoic acid is centered at 3.5 eV, which is far from the PL energy of GO, suggesting that no poly-aromatic compounds contribute to the PL of GO.

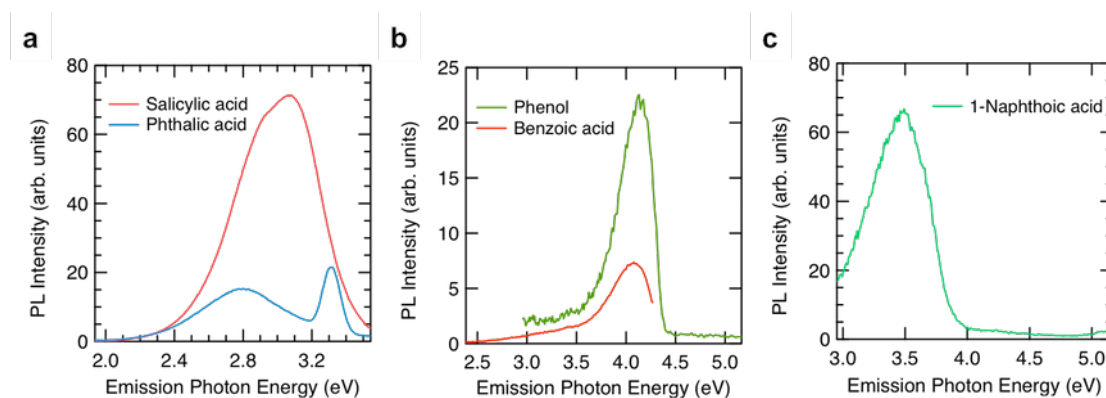


Figure 3.17 PL spectra of (a) phenol and benzoic acid as the model compounds of P₁, (b) Salicylic acid and phthalic acid as those of P₂, and (c) 1-naphthoic acid.

We also confirmed that the PL spectra of P₁ and P₂ peaks showed almost no change after a dialysis process for two days using a pour size of 1,000 Da (Figure 3.18). This experimental fact provides confirmation that the PL centers (P₁ and P₂) are not from isolated molecules in the aqueous solution; rather they are from the quasi-molecular structures embedded in the large sp³ matrices of GO. The chemical structure of the sp² fragment showing P₁ emission includes several oxygen functional groups and that of P₂ includes a single oxygen functional group.

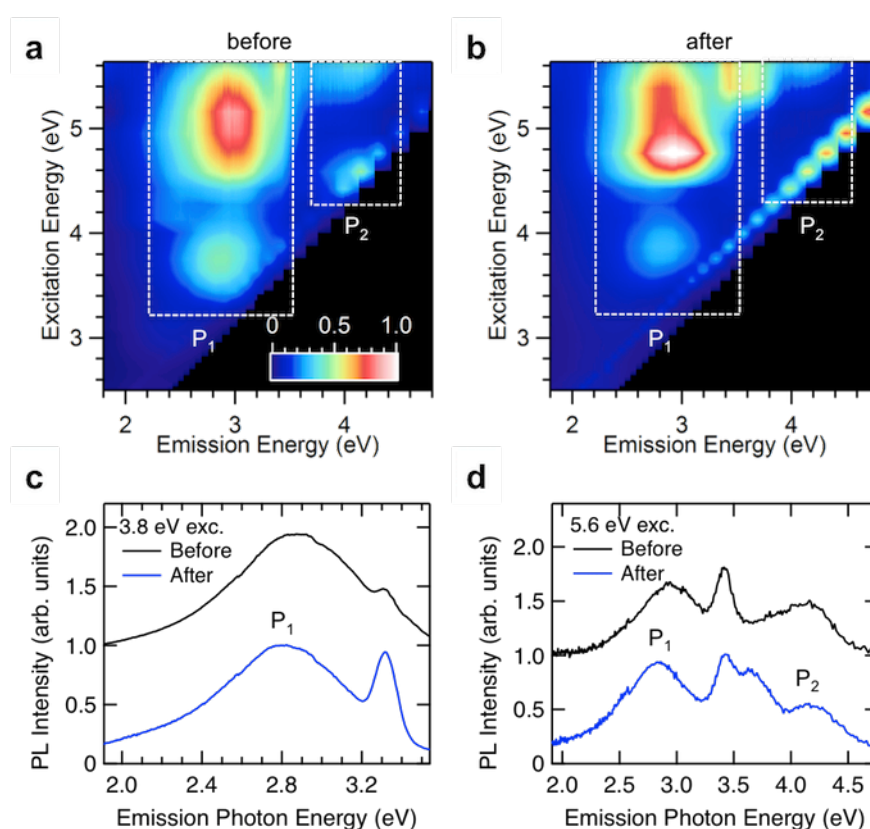


Figure 3.18 PL properties of GOs before and after dialysis process. PLE maps of GOs (a) before and (b) after dialysis process. PL spectra of GOs at (c) P₁ and (d) P₂ peaks, excited with 3.8 and 5.6 eV, respectively.

The pH dependence of PL and PLE spectra is also consistent with the interpretation presented above. The reduction of the integrated PL intensity and the peakshift of PL (PLE) of P₁ in the basic condition, shown in Figure 3.13 and Figure

3.15, are associated with the deprotonation of an oxygen functional group, such as a carboxyl group,¹⁶² from the sp^2 fragment (hydroxybenzoic and dicarboxybenzoic acid structure) embedded in the GO. Phthalic acid shows low PL intensity in higher pH, while hydroxybenzoic acid shows PL in higher pH. The low PL intensity of P_1 (Figure 3.15c) can be explained by a mixture of PL from these PL centers.

The observed redshift of the P_1 features from pH 4.4 to 11.1 (Figure 3.15a) can be also explained by the overlapping of several PL peaks because the GO has the inhomogeneous structure including some kinds of oxygen functional group; carboxyl, hydroxyl group, and so on.^{77, 95, 156} Particularly, we focused on hydroxybenzoic acid (salicylic acid) and dicarboxylic acid (phthalic acid). The hydroxybenzoic acid has three kinds of structure; *o*-, *m*-, and *p*-hydroxybenzoic acid. *o*-Hydroxybenzoic acid is called phthalic acid. The salicylic acid and *m*-hydroxybenzoic acid show PL centered at 3.1 and 3.0 eV, respectively. The PL of salicylic acid shows higher intensity than that of *m*-hydroxybenzoic acid in higher pH,¹⁶³ which should contribute to the redshift of the PL in the GO from pH 4.4 to 11.1. Phthalic acid shows PL at 2.8 eV and high PL intensity from neutral to basic region, which should contribute to the experimentally observed redshift and spectral broadening of the PL in the GO.

The intensity of P_2 also decreases monotonically from neutral to basic conditions, as shown in Figure 3.15c. This pH dependence of P_2 emission intensity is similar to that of aromatic compounds that contain the carboxyl group.¹⁶² The decrease of PL intensity in the basic region can be explained by the deprotonation of an oxygen functional group from the sp^2 fragment (phenol and benzoic acid structure^{141, 162}) embedded in the GO.

3.8. Oxidation level of the PL centers

Here we examine the oxidation level of the PL centers of P_1 and P_2 . We exposed the GO in the aqueous solution to cw UV light irradiation for 12 h using a Xe lamp. This treatment provides a gradual reduction of GOs.^{43, 164} Figure 3.19a shows PLE maps before and after the reduction process by irradiation of UV light. The PL and PLE peaks do not show a spectral shift; however, the PL intensity is drastically changed. Figure 3.19b shows PL spectra of GOs before and after the reduction process with excitation at 5.6 eV. By the reduction process, the relative PL intensity of P_2 to P_1 changes remarkably, i.e., the decrease of P_1 and increase of P_2 peak intensity. This change can be understood in terms of differences in the oxidation levels between P_1 and P_2 PL centers. We have attributed the P_1 PL to the chemical structures that include several oxygen functional groups and the PL of P_2 to structures that include a single oxygen functional group. The oxygen functional groups are reduced by the UV light. As a result, the chemical structure of the P_1 PL centers (sp^2 fragment bound to several oxygen functional groups) are changed into that of P_2 centers (sp^2 fragment bound to a single oxygen functional group). Thus, these results suggest that the PL centers of P_2 have more reduced chemical structures compared with those of P_1 .

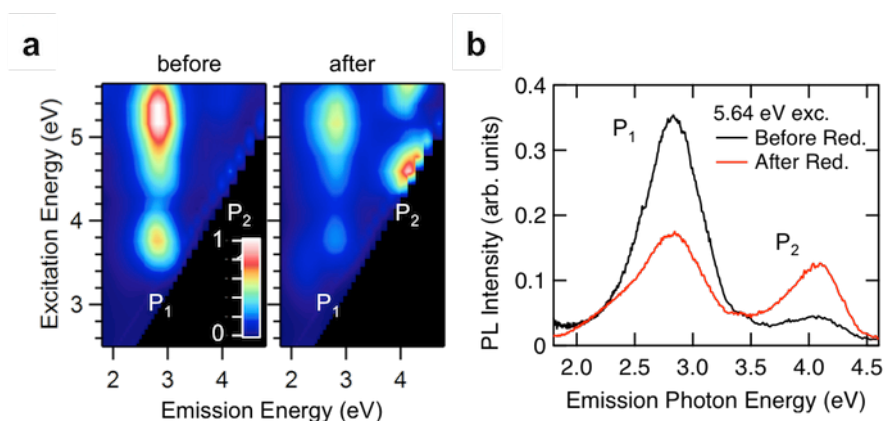


Figure 3.19 (a) PLE maps of GOs before and after the reduction process by Xe lamp irradiation. (b) PL spectra of GOs before (black line) and after (red line) the reduction process with excitation at 5.6 eV.

3.9. PL lifetime of the PL centers

To confirm these assignments, we conducted time-resolved PL spectroscopy to examine the PL lifetimes of P_1 and P_2 peaks. Figure 3.20a and b show the normalized transient PL decay curves monitored at 2.8 (P_1) and 3.8 eV (P_2) with excitation at 3.6 and 4.4 eV, respectively, in various pH from 1.8 to 11.1. The transient PL signals of both P_1 and P_2 peaks do not exhibit single-exponential decay, implying that the PL signals come from some chemical structures of PL centers with various PL lifetimes. The PL decay behaviors of P_1 and P_2 change slightly in varying pH conditions. Figure 3.20c shows the two-dimensional PL lifetime map with excitation at 4.4 eV. Two emission features at 2.8 and 3.8 eV are clearly observed in the map. These emission features correspond to P_1 and P_2 peaks and are consistent with the results of the cw PL measurement, as shown in Figure 3.11.

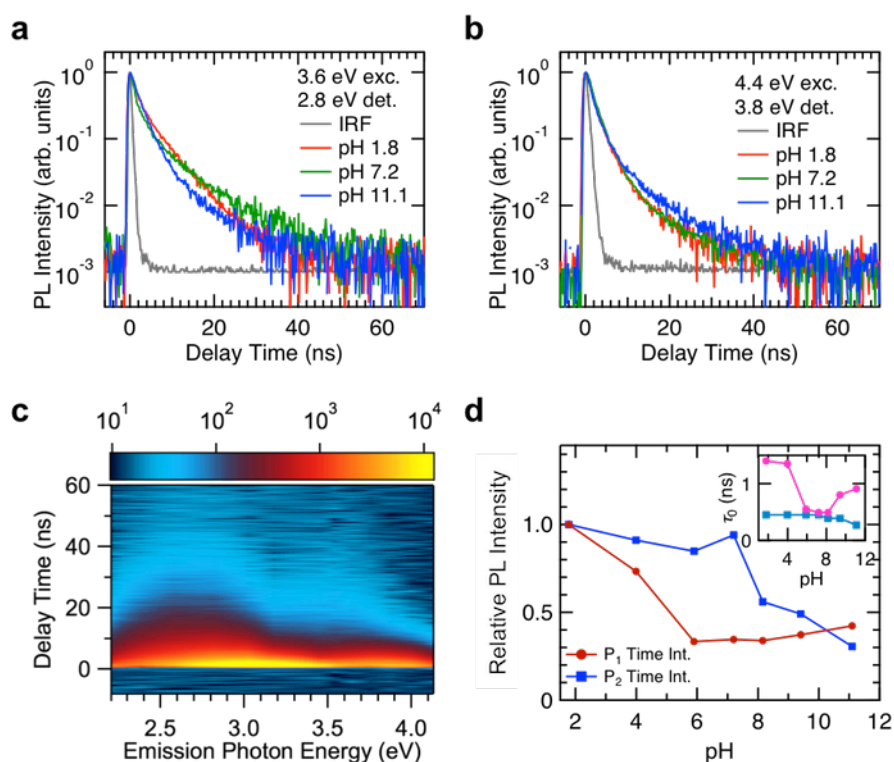


Figure 3.20 (a, b) PL decay curves of P_1 and P_2 in the GOs measured at 3.6 and 4.4 eV

excitation with various pH from 1.8 to 11.1, respectively. The instrument response function (IRF) in this measurement is also shown. (c) Two-dimensional PL lifetime map of GO. (d) Time-integrated PL decay signals of P₁ and P₂ peaks as a function of pH. The inset shows the obtained lifetimes of P₁ and P₂ as a function of pH.

The PL lifetimes of each decay curve are determined as an average lifetime τ_{PL} . The PL lifetime can be written as:

$$\tau_{\text{PL}} = \int_0^{\infty} tI(t)dt / \int_0^{\infty} I(t)dt, \quad (\text{Eq. 3.2})$$

where t is delay time and $I(t)$ is PL intensity as a function of t . The obtained average lifetimes of P₁ and P₂ plotted as a function of pH are in the range of 8-13 and 6-8 ns, respectively, as shown in the inset of Figure 3.20d. We also plotted the time-integrated PL decay signals of P₁ and P₂ peaks as a function of pH. Figure 3.20d shows that the pH dependence of obtained time-integrated PL decay signals is almost consistent with that of the time-integrated (cw) PL intensity in Figure 3.15c. This result indicates that the time-integrated PL intensity change with varying pH comes from the change of number density of PL centers.

The PL lifetimes of aromatic carboxylic acid and hydroxyl acid, such as naphthoic acid, benzoic acid, naphthol, and naphthoic acid, are the order of several nanoseconds,^{159, 165-167} which is similar to the experimentally observed PL lifetimes of P₁ and P₂. These results also support the interpretation that the electronic structure of the P₁ and P₂ PL centers are analogous to hydroxybenzoic acid, dicarboxylic acid, and phenol or benzoic acid embedded in the GO, respectively. Therefore, the series of the time-resolved PL measurements indicate that the PL originates from the quasi-molecular states, that is, the sp² domains of GO are embedded in sp³ matrices of oxygen functional groups .

3.10. Chapter summary

In this Chapter, we studied the mechanism of two distinct PL peaks (~ 2.8 and ~ 4.1 eV) of highly exfoliated GOs in aqueous solution and determined possible quasi-molecule structures of PL centers in the GO. We used static and time-resolved PL spectroscopy. The average PL lifetimes of those emission peaks at ~ 2.8 and ~ 4.1 eV are 8-13 and 6-8 ns, respectively. The experimentally observed peak photon energy of pH-dependent PL, PLE spectra, and the PL lifetimes are closely coincident with those of aromatic compounds bound with oxygen functional groups, which suggests that the PL peaks come from the quasi-molecular structure consisting of a small number of aromatic rings with oxygen functional groups embedded in the GO. The obtained results in this study provide important insights for understanding of optical and electronic properties of GO.

Chapter 4. Excitonic photoluminescence from nanodisc states in graphene oxide

4.1. Introduction

The presence of the oxygen functional groups in graphene oxide (GO) provides opportunities for tailoring its optical properties. The intrinsic and tunable luminescence paves the way for new functional optoelectronics. In this Chapter, we elucidate the PL mechanism of NIR-visible emission, which can be key factor to realize the tailor-made light emitting devices. We note that the calculations based on the *ab initio* density functional theories (DFT) in this Chapter have been conducted by Dr. Xi Zhu and co-workers in Nanyang Technological University, Singapore.

The GO is an oxidized graphene sheet decorated with oxygen functional groups including hydroxyl and epoxy groups on the basal plane and carboxyl groups at edge sites.^{95, 156, 168, 169} The non-decorated region consists of sp^2 graphitic carbon of which their sizes are typically smaller than 6 nm^2 revealed by high-resolution transmission electron microscopy (TEM).^{38, 80} Reduction treatments transform GO from an insulator to a graphene-like semimetal by varying the ratio of sp^2 and sp^3 carbon bond.^{32, 41, 144, 170-173} The bandgap engineering of GO stimulates a study of its optical properties and application for optoelectronic devices.

It has been reported that the GO exhibits photoluminescence (PL) in near-infrared, red, blue and even ultraviolet region.^{39, 41, 43, 80, 124, 148, 174-176} Although its non-stoichiometric and inhomogeneous structure makes it difficult to understand the mechanisms of PL, recent studies have revealed its origin in a step-by-step manner. The blue PL of reduced GO is attributed to the recombination of electron-hole pairs,

localized within the small sp^2 carbon clusters.^{39, 80} The subpicosecond time-resolved PL spectroscopy show that the red PL is a consequence of spectral migration among emitting states.⁴³ Moreover, the roles of functional groups as well as the non-oxidized region are added to the interpretation of the PL.^{79, 124, 141, 153-155, 175}

Since the optical behavior in GO is dictated by a bound electron-hole pair (exciton) confined in the sp^2 carbon clusters,^{42, 43, 79, 124} it implies scaling effect on the properties with the size of sp^2 carbon clusters in GO. Considering that the bandgap of GO is tunable by the reduction treatments and the position of oxygen atom is able to be manipulated with atomic precision,^{172, 177} it is intriguing to explore scaling relationships of the electronic and excitonic properties with the size of the sp^2 carbon clusters. In this Chapter, we examine the PL mechanism associated with the scaling effect using photoluminescence excitation (PLE) and time-resolved spectroscopy, and first principle density functional theory (DFT) based on many body perturbation theory, i.e. *GW* (with quasi-particle correction) and Bethe-Salpeter (with electron-hole interaction) approaches. We show that the PL originates from ensemble emissions from various sizes of sp^2 carbon cluster states and the quantum confinement induces the excitonic properties (Figure 4.1). We further demonstrate that the excitonic properties are highly sensitive to the protons around the oxygen functional groups of GO. Our study sheds light on the aspect of the zero dimension-like graphene structures in two-dimensional GO sheets.

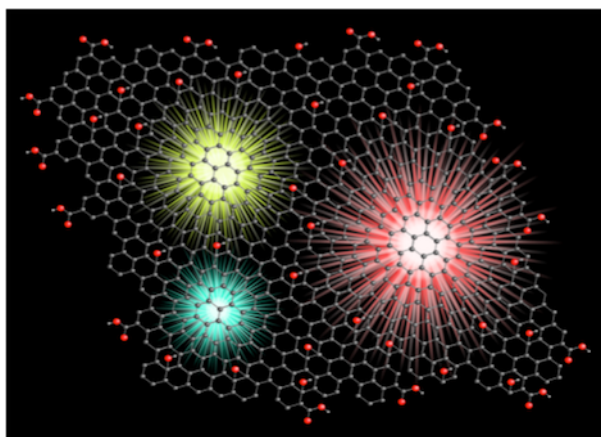


Figure 4.1 Schematic image of sp^2 carbon clusters exhibiting luminescence depending on their size. The grey, red and white dots represent carbon, oxygen and hydrogen atoms, respectively.

4.2. Sample preparation

We used aqueous dispersions of GO (highly concentrated graphene oxide dispersion in aqueous solution, purchased from Graphene Supermarket) produced by a modified Hummer's method. For optical measurements, GO solution was diluted down to 0.1 of absorbance to avoid reabsorption of luminescence. The pH of GO dispersions was controlled using NaOH (Wako first Grade, purchased from Wako Pure Chemical Industries, Ltd.) from pH 4.1 to 11.3 and HCl (Volumetric Analysis Grade, purchased from Wako Pure Chemical Industries, Ltd.) solution from pH 4.1 to 3.4. The photographs of the GO solutions are shown in Figure 4.2. The color of the solution turns dark with increasing pH of the solution. Reduced GO solution was prepared by photochemical reduction for the as-purchased GO solution. A Xe lamp (Zolix, LSH-X150) was used for the illumination of the GO solution in a quartz cell to conduct the photochemical reaction with 150 W of lamp power for 50 h.

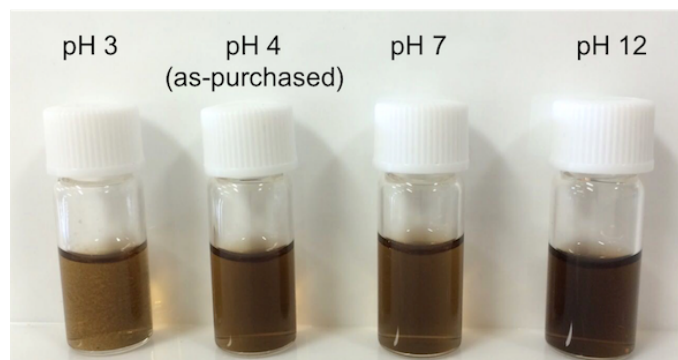


Figure 4.2 Photograph of GO solutions for pH 3, 4 (as-purchased), 7 and 12.

4.3. Experimental methods

The optical absorption was collected with UV-vis spectroscopy (Shimadzu, UV-1800). In the PL and PLE measurements, the GO in aqueous solution was excited by Xe lamp light passed through a monochromator, and all the PL spectra were collected at room temperature. Color glass filters were used to cut excitation light in the detection side (long pass above 320, 435 and 610 nm, Edmund Optics, UV N-WG320 50MM, and Thorlabs, FGL435S and FGL610S, respectively). The slit width of monochromator in both excitation and detection was adjusted from 5-20 nm depending on its PL intensity and demands. The relative PL intensity was corrected for instrumental variations in detection sensitivity using a standard lamp (Ocean Optics, LS-1-CAL). Atomic force microscopy (AFM) (Digital Instruments, Nanoscope IIIa) was used to obtain the surface morphology of GO with cantilevers purchased by Olympus (OMCL-AC160TS-C3).

Time-resolved PL measurements were carried out using streak camera (Hamamatsu Corporation, C5680). Figure 4.3a and b show the schematic experimental apparatus and photograph of the measurement. The GO aqueous solution was excited with optical pulses from second harmonics of a Ti:sapphire laser light at 3.4 eV (Spectra Physics, Tsunami, repetition rate of 80 MHz, and pulse duration ~ 1 ps). A β -barium

borate (BBO) crystal was used to generate the second harmonics. The luminescence from the sample was collected through a lens (focal length $f = 200$ mm) and dispersed in a polychromator (Hamamatsu corporation, C5094). A part of the excitation light was split at the beam splitter to a fast photodiode (Hamamatsu Corporation, C1802-02) as an optical triggering signal. The temporal resolution of the PL decay measurements is ~ 20 ps. Figure 4.3c shows the schematic of streak camera, which is a device to detect time-dependent spectral relaxation.¹⁷⁸ In the streak camera, luminescent light is collected to the photocathode and converted into photoelectrons. The photoelectrons are dispersed by sweeping voltage between the deflection plates (or sweep electrodes) with synchronizing excitation laser pulse. The dispersed photoelectrons are multiplied in the micro-channel plate (MCP) and converted into photons in the phosphor screen. The photons are detected on CCD. Since the photons are detected at different positions depending on arrival time and luminescent wavelength, the streak camera can be used to measure temporal and spectral light intensity.

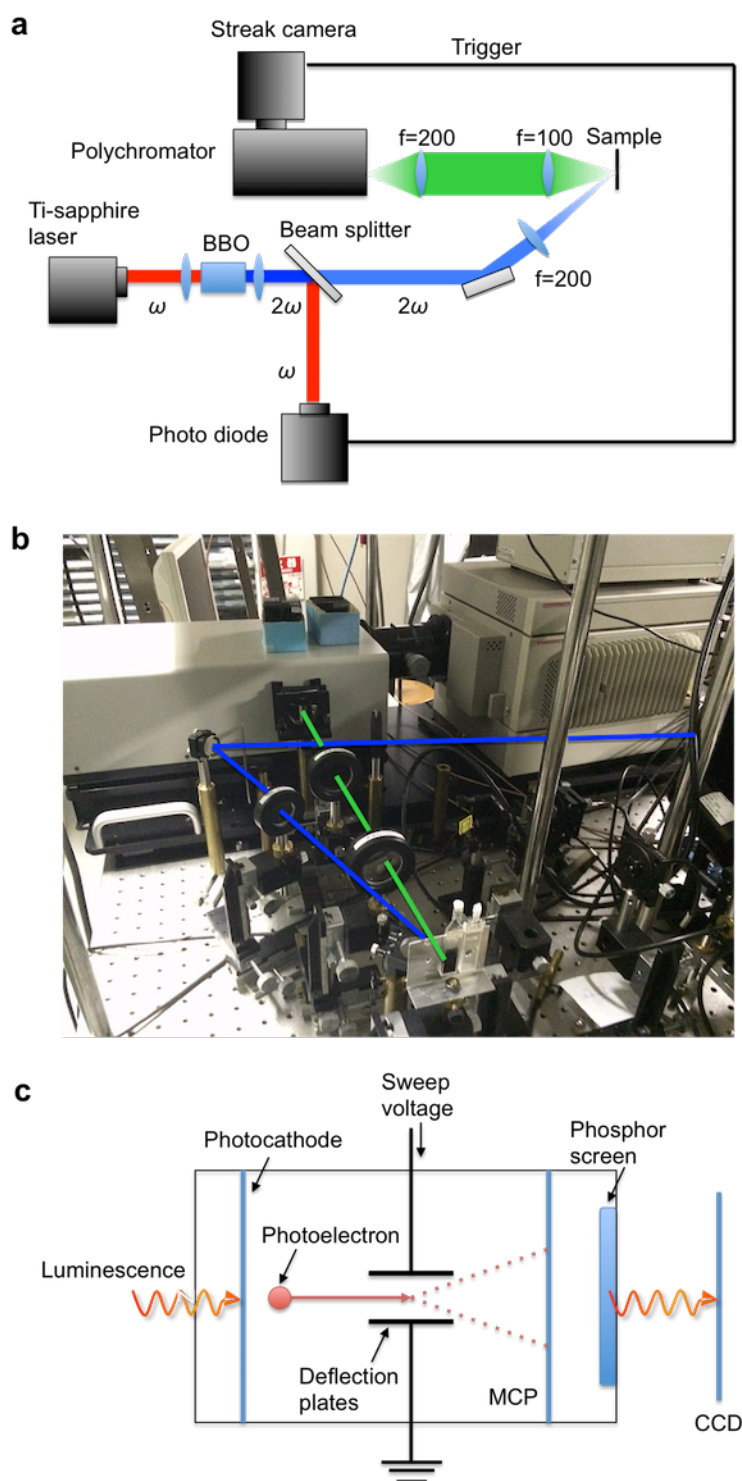


Figure 4.3 (a) Schematic optical alignments and (b) photograph of the time-resolved PL measurement, where ω is the frequency of the excitation light and f is the focal length of the lens. The excitation light with first (ω) and second (2ω) harmonics is colored with red and blue, respectively, and the luminescence from the sample is colored with green.

The laser pathways are highlighted by blue and green lines, in which the colors correspond to the color in (a). The photograph was provided by Prof. Masao Ichida, Konan University. (c) Schematic of typical streak camera. (Reproduced from Ref. ¹⁷⁸)

4.4. Theoretical calculation methods

Using first-principles DFT based on many body perturbation theory, we investigated the electronic and excitonic properties with the scaling effect in the sp^2 carbon clusters system. We first obtained the ground state wavefunctions by the local density approximation (LDA) using the ABINIT code¹⁷⁹. Normconserving pseudopotentials with a kinetic energy cutoff of 50 Ry were employed during the calculations. Each structure was fully relaxed until the force convergence reaches 0.01 eV/Å. The G_0W_0 approximation was used for the self-energy operator to make the quasiparticle corrections to the LDA ground state bandgaps. The plasmon-pole approximation¹⁸⁰ was introduced to treat the screening. The electron-hole interactions are solved by the Bethe-Salpeter equation, and a box-shape truncated Coulomb interaction was applied to the calculation cell to avoid the image effect caused by the nearby supercells to mimic isolated graphene nanodiscs (GNDs) as the similar way in Ref. ^{181, 182}.

4.5. Optical transitions in the graphene nanodisc states

4.5.1. Typical PLE properties

Figure 4.4a shows PL spectra of GO in aqueous solution with excitation at various photon energies from 1.8 to 2.5 eV, where the arrows indicate the excitation energies. The PL spectrum of GO shows a broad emission peak in NIR region (~1.7 eV), and the gradual blueshift and broadening of emission features are observed with increasing the excitation energy. Figure 4.4b shows PLE spectra of GO with various monitored

emission energies from 1.6 to 1.8 eV, where the numbers indicate the monitored photon energies. The PLE spectra show a broad resonance peak below ~ 1.95 eV depending on the monitored energy, which is also observed in the PLE map as shown in the inset of Figure 4.4a.

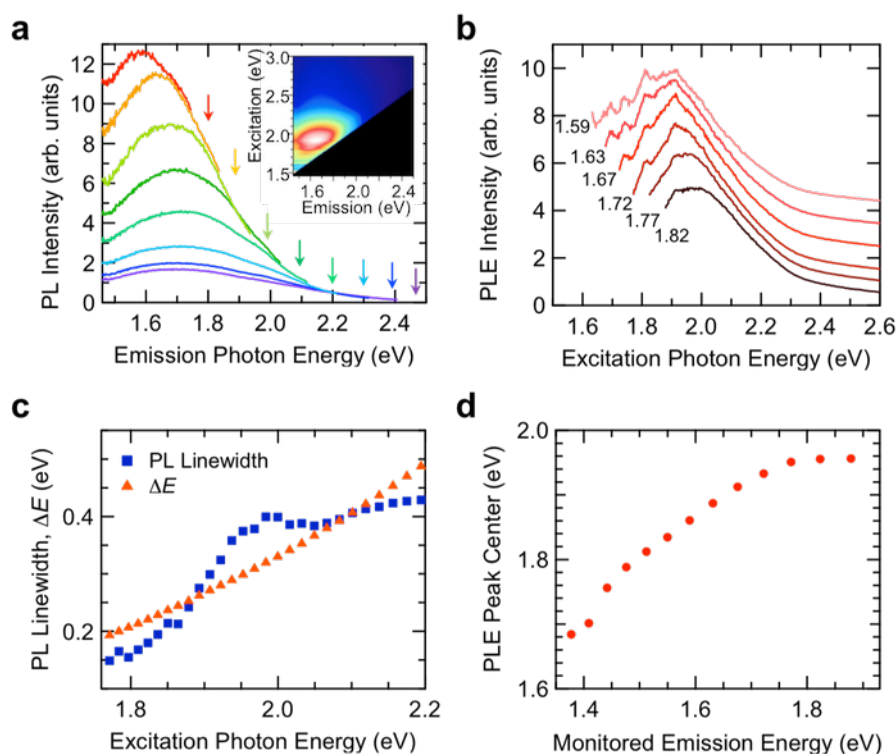


Figure 4.4 (a) PL spectra of GO in aqueous solution obtained with various excitation energies from 1.8 to 2.5 eV. The arrows indicate the excitation energy. Inset shows a PLE intensity map of GO. (b) PLE spectra of GO with various monitored emission energies from 1.6 to 1.8 eV. The numbers indicate the monitored emission energy. The spectra in (a) and (b) are displaced along the vertical axis for clarity. (c) The linewidth of PL peak and energy shift between excitation and PL peak center energy (ΔE) as a function of excitation energy. (d) PLE peak center of GO as a function of monitored emission energy.

The observed PL spectra indicate the broadening originates from the emission from inhomogeneous structure of GO because of the energy redistributions within an

ensemble of emitting states.⁴³ The PL linewidth and peak center are analyzed by curve fitting of Gaussian function to the PL spectra. Figure 4.4c displays the linewidth of PL peak (i.e., full-width at half-maximum: FWHM) and energy shift as a function of excitation energy, where the energy shift, DE , is defined as the energy difference between the excitation energy and PL peak center. The PL linewidth increases monotonically and reaches a nearly constant value (~ 0.4 eV) with a slight increase above 1.9 eV of excitation, with an increase of excitation energy. The energy shift increases with excitation energy. The PLE peak energy of GO as a function of monitored emission energy is plotted in Figure 4.4d. The PLE peak energy increases monotonically depending on the monitored emission energy in the obtained range and shows saturation above 1.8 eV of monitored emission energy.

4.5.2. Morphology

Here we discuss the mechanism of NIR PL of GO. The optical and atomic force microscopy (AFM) image reveal that typical lateral size of GO is ~ 1 μm (Figure 4.5a and b). The height of the GO flakes is mainly in the range of 1-2 nm and its average is ~ 1.5 nm (Figure 4.5b). The estimated size of emission features can be much smaller than overall size of a GO flake with consideration of the energy of NIR PL (~ 1.7 eV) of GO, because the predicted bandgap of a large size graphene structure (~ 1 μm) is negligibly small due to the weak quantum confinement effect. The PL shift depending on the excitation energy (Figure 4.4a) suggests the contribution of sp^2 carbon clusters in GO with various optical gaps (~ 1.7 -1.95 eV) depending on their sizes, which we call graphene nanodisc (GND) states.

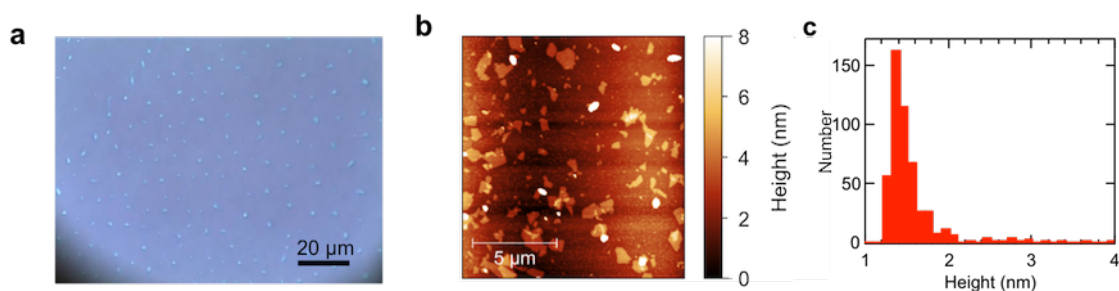


Figure 4.5 (a) Optical microscopic, (b) AFM image and (c) height histogram obtained from AFM of GO on an SiO₂/Si substrate.

Here we define GND states as isolated sp^2 carbon clusters with the size of several nanometers embedded in sp^3 domain or GO matrix. In contrast to the quasi-molecular states of GO discussed in Chapter 3, the size of GND states is relatively large. The quasi-molecular states consist of a few aromatic rings with oxygen functional groups. The GND states consist of enough numbers of aromatic rings and result in forming a disk-like structure so that the exciton can be confined in the sp^2 carbon clusters. In the DFT calculation, we assume that at least seven aromatic rings compose the GND states. The main part of Figure 4.6 shows aberration-corrected TEM image of a single sheet of suspended GO, which has been reported by Zettl and co-workers.³⁸ In Figure 4.6, the domain A shows GO with a high degree of oxidized region, that is the sp^3 domain. The both domain B and C are the sp^2 carbon clusters and their size is in range of 1 and 6 nm².^{38, 80} The difference of domain B and C is with and without oxygen functional groups on the plane of sp^2 carbon clusters. The electronic states are quantum-confined in the sp^2 carbon clusters embedded in sp^3 domains acting as potential barriers. Figure 4.7 shows schematic image of ensemble emission from the multiple GND states of GO with high and low energy excitation conditions, and corresponding energy diagram, where the energy gap decreases with increasing the size of the GND states. The observed broadening of PL linewidth with increasing the excitation photon energy (Figure 4.4c) can be attributed to the increase of overlapping ensemble emission from the multiple

GND states. Higher energy light excites many sizes of sp^2 carbon clusters, while lower energy light excites only large sp^2 carbon clusters. Therefore, the excitation energy-dependent PL can originate from the size-selected resonant excitation for the GND states with various sizes.

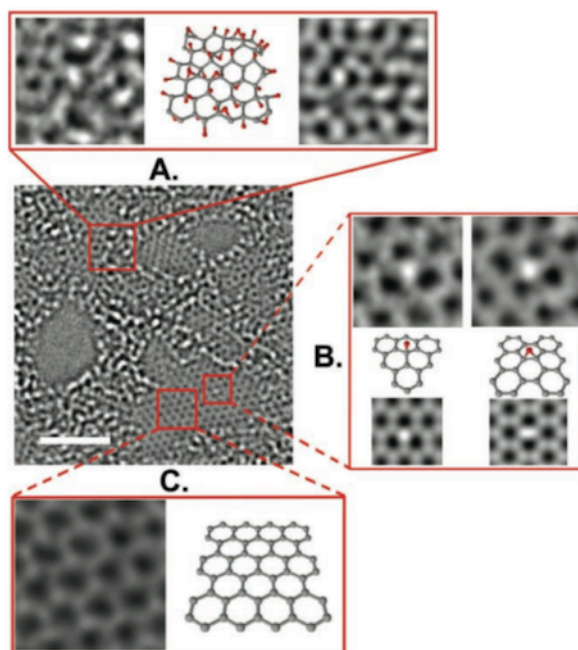


Figure 4.6 Aberration-corrected TEM image of a single sheet of suspended GO. The scale bar corresponds to 2 nm. Expansion (A) shows 1 nm² enlarged oxidized region (left), proposed atomic structure (center), and simulated TEM image. Expansion (B) shows obtained TEM image of hydroxyl (left top) and epoxy (right top) functional groups, the second and third line display those of atomic structure and simulated TEM images. Expansion (C) shows 1 nm² graphitic region and its atomic structure. (Taken from Ref. ³⁸)

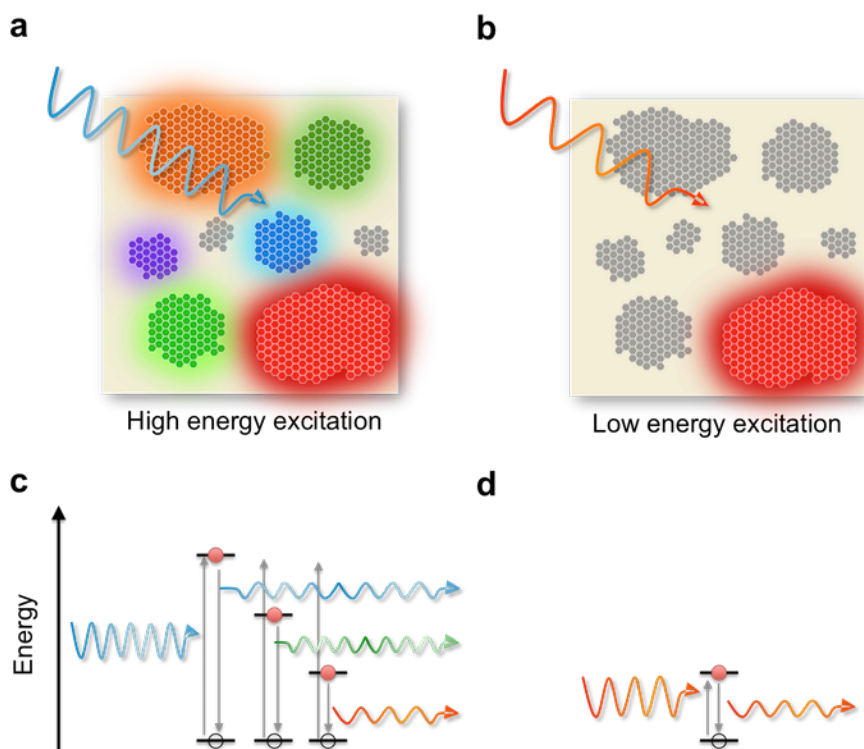


Figure 4.7 Schematic image of ensemble emission from the multiple GND states of GO with (a) high and (b) low energy excitation. Energy diagram of the ensemble emission with (c) high and (d) low energy excitation conditions, where red dots and white dots represent excited electrons and holes, respectively. The straight arrows and winding arrows show the optical transitions and luminescence with various energies.

4.5.3. Calculation of optical transition energy

The energies of PLE and PL in GO are further examined by the first principle DFT based on GW and Bethe-Salpeter approaches. Hexagonal GND structures are constructed as a model system with termination of hydrogen atoms (top of Figure 4.8). Figure 4.8a shows the binding energy of exciton (E_b) as a function of size of GND (D), where A_1 (≈ 2.2) is coefficients, and the two numeric number a_1 is an exponent in the power law scaling relationship. The binding energy of exciton (E_b) is defined as the energy difference between the E^{GW} and E_{ts} , that is $E_b = E^{GW} - E_{ts}$, where E^{GW} is the GW

one-electron bandgap and E_{ts} is the first optically allowed transition energy corresponding to the absorption energy.

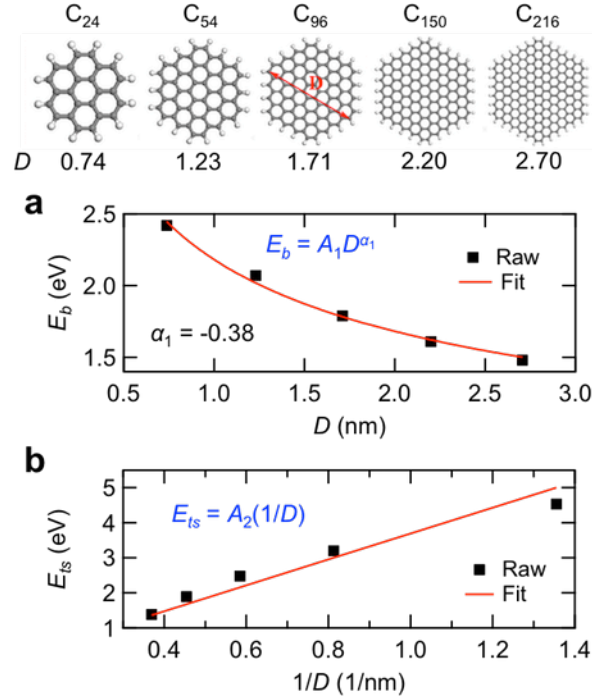


Figure 4.8 Model structures for the GNDs with size scaling. The diameter (D) is displayed on the bottom of each structure. (a) Scaling relations for the exciton binding energy (E_b) with the size of the GNDs (D). (b) The transition energy (E_{ts}) as a function of inverse of a size ($1/D$). The E_{ts} is picked up as the first bright peak in the absorption spectrum for each structure. The black block and the red line represent the raw data and the numeric data by power law fitting.

Figure 4.8b shows the calculated E_{ts} as a function of inverse of a size ($1/D$), where the value of slope A_2 is 3.63. We can clearly see simple linear scaling law of E_{ts} as a function of $1/D$ in the GNDs system, which is similar to that in the 1D confined GNRs.¹⁸² This is because $E \propto 1/D$ can be obtained by substituting the solution of a-particle-in-a-box-problem $q_n = n\pi/D$ into the linear dispersion relationship of graphene $E_{\pm}(\mathbf{q}) \approx \pm\hbar v_F |\mathbf{q}|$ as mentioned in Section 2.5.1. Therefore, the interval between the absorption peaks (E_{ts}) between each size of GND becomes narrower at

larger diameter. The departure from linear scaling of E_{ts} is due to the many-body interactions, where the electron-electron interaction exhibits logarithmic renormalizations in the band dispersions.¹⁸³ It is found that the exciton absorption peaks of GNDs with D from 2.70 to 0.74 nm correspond from 1.5 to 4.2 eV (corresponding to wavelength in range of 800-300 nm) from the scaling law in Figure 4.8b, which covers whole wavelength from visible to NIR region. From the experimental and theoretical results, the estimated size of GND states falls within a reasonable range compared to the previous reports of observation in the high-resolution TEM images (see Section 4.5.2).^{38,}

80

Figure 4.9 shows the GW one-electron bandgap (E^{GW}) as a function of size of GND (D), where A_3 (=5.8) is a coefficient, and the numeric number α_3 is exponents in the power law scaling relationships. The E^{GW} can be fit with the size D by a power law with an index $\alpha_3 = -0.63$, which is smaller than the values in the 1D graphene nanoribbons (GNR).¹⁸² It is due to the dimension reduction from the quasi 1D GNRs to 0D GNDs.

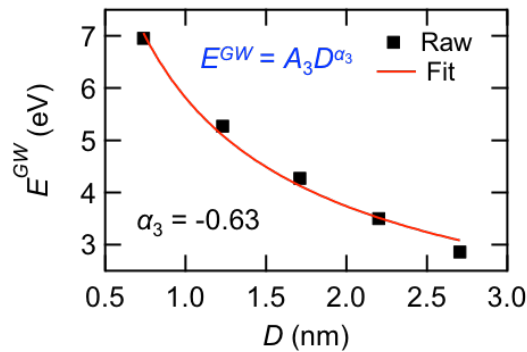


Figure 4.9 Scaling relations for the GW bandgaps (E^{GW}) with the size of the GNDs (D).

We have found that the bandgaps of GNDs decrease from UV to NIR regions corresponding to the size of GND states from the experimental and theoretical results.

In our previous report, a co-existing blue and UV PL of GO exhibits excitation peaks at 4.5 and 4.1 eV, in which the PL originates from a quasi-molecular fluorescence consisting of a few benzene rings with oxygen functional groups.[11] The PL of reduced GO shows excitation peak at 3.8 eV and continuous decrease of excitation peak energy from 2.6 to 2.0 eV (Figure 4.11), in which the emission species can be small and isolated sp^2 domains (or small GND states) but larger than the quasi-molecular states.^{39,}
⁸⁰ The NIR PL shows continuous excitation peak at lower than 1.9 eV, in which the size of GND states can be larger than that above. The scaling law of E_{ts} (Figure 4.8c) explains these experimental trends qualitatively.

4.5.4. Effect of reduction

The size of GNDs in GO can be varied by photochemical reduction.^{80, 144, 164} After deoxygenation, small and isolated sp^2 domains are formed. We have carried out PL and PLE measurements for photochemically reduced GO to investigate the optical properties of smaller GNDs. The photograph of the reduced GO solution is shown in Figure 4.10 and the as-purchased GO is also displayed for reference. The color of the solution turns dark through the reduction treatments. Figure 4.11 displays (a) PLE maps of reduced and as-prepared GO, and (b) typical PL and PLE spectra of the reduced and as-prepared GO. The PL exhibits continuous blueshift with increasing excitation energy of 2.0 to 2.6 eV, while the PL energy with excitation of 3.8 eV is independent of the excitation energy. New PL features for the reduced GO are also observed in higher energy at 2.0-2.3 (P_4) and 2.7 (P_1) eV with excitation peak at 2.0-2.6 and 3.8 eV, respectively. It should be noted that the luminescent species labeled as P_3 is similar PL energy to those of P_3 features for GO (Figure 3.13) and GQD (Figure 3.14). The PL features resemble the species P_4 and P_1 that observed in the centrifuged GO (see Chapter 3) and the GQD synthesized from carbon fibers through strong oxidation process, originating from quasi-molecular fluorescence of small sp^2 fragments in GO.¹⁷⁵

This picture is consistent with the electrical measurement varying reduction level of GO^{32} as shown in the inset of Figure 2.23.

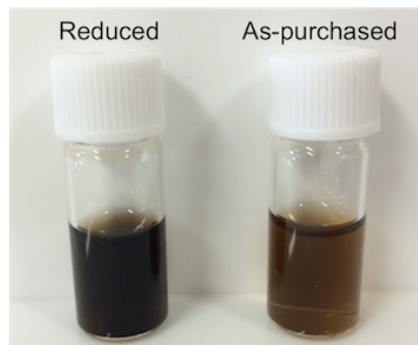


Figure 4.10 Photograph of the reduced GO solution. As-purchased GO is also displayed for reference.

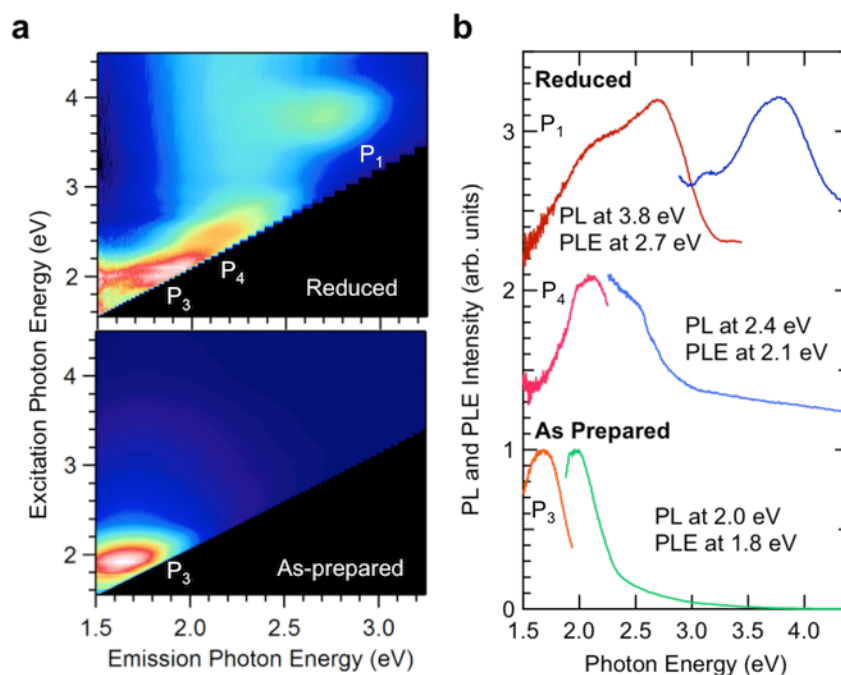


Figure 4.11 (a) PLE intensity maps of reduced (upper) and as-prepared (bottom) GO in aqueous solution. (b) Typical PL (left) and PLE (right) spectra of the reduced and as-prepared GO. Each luminescent species is labeled as P_1 , P_3 , and P_4 that corresponds the labels used for those of the GO and GQD.

4.6. Dynamics of the carriers in the nanodisc states

4.6.1. Time-resolved PL measurements

Time-resolved PL spectroscopy is conducted to further verify the characteristics of the GND states. A PL decay map is obtained with excitation of 3.4 eV (the inset of Figure 4.12a). The map exhibits larger amplitude and slower decay at lower emission energy. Figure 4.12a shows the PL decay profiles monitored at various emission energies from 1.80 to 2.73 eV. The PL decay profiles at lower emission energy exhibit remarkable build-up behavior in the rising stage of the PL profile, suggesting the energy transfer between the GND states. The build-up behavior of the decay curves can be attributed to be an energy influx (or energy transfer) from adjacent GND states from higher-energy level. The energy transfer is also implicated by the experimental observations of the increasing ΔE and broadening PL with increasing excitation energy (Figure 4.4).

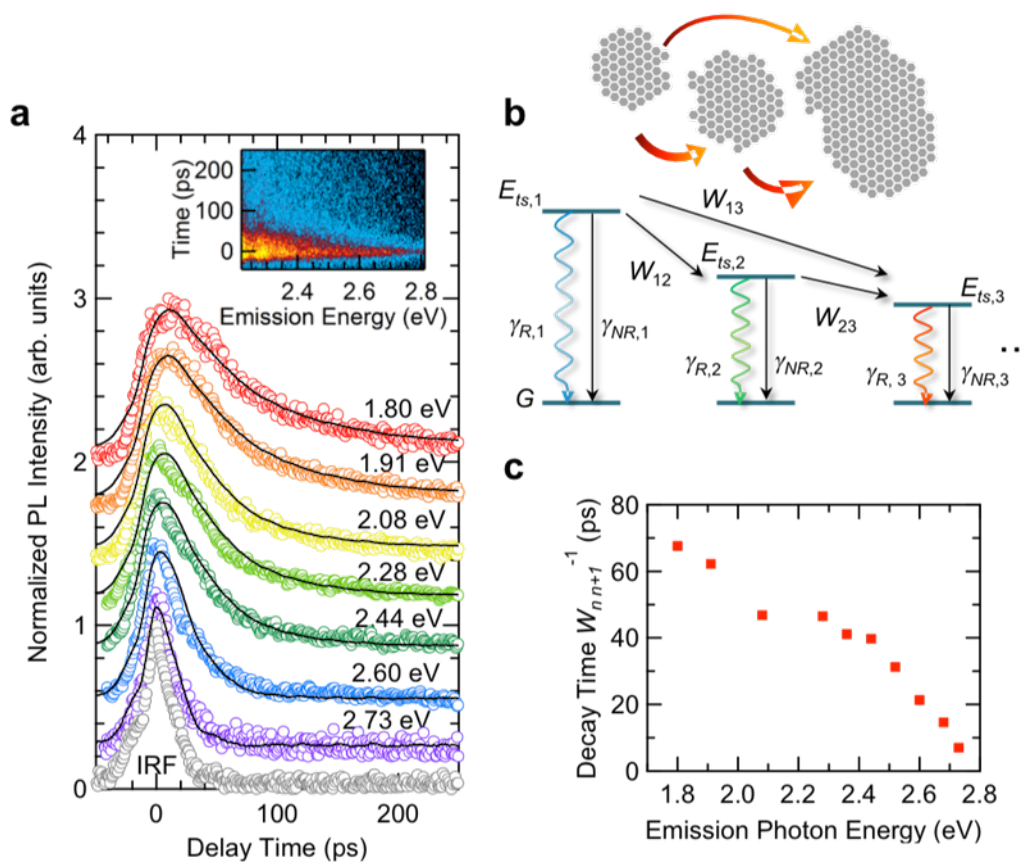


Figure 4.12 (a) Normalized PL decay profiles of GO in aqueous solution with various emission energies of 1.80 to 2.73 eV excited at 3.4 eV. The gray circle shows the instrument response function (IRF) in the experiment. The profiles are displaced along the vertical axis for clarity. The inset displays a PL decay map. (b) Schematic illustration of the exciton relaxation process composing of radiative (γ_R), non-radiative decay (γ_N) and energy transfer (W) between neighboring GNDs. The image at top is a schematic image of the energy transfer between GNDs. (c) Decay time for the energy transfer $W_{n,n+1}^{-1}$ as a function of emission photon energy.

4.6.2. Quantum dots array model

We use analog of quantum dot (QD) array model^{184, 185} to analyze the dynamics of

energy transfer in GO. Figure 4.13a and b show schematic illumination of the exciton dynamics in the QD array generated with higher and lower energy excitation, respectively. Higher excitation energy leads multiple-stage relaxations, while lower energy excitation leads a single stage relaxation. Figure 4.13c displays simulated luminescence decay curves as a function of delay time after a pulse excitation with different excitation energy ϵ_{exc} from -0.08 to 0.04 eV at 300K, where ϵ_{exc} is a relative energy to the average exciton energy in the QDs. The lower energy excitation induces a monotonic decay close to a single exponential. In contrast, the higher energy excitation induces an initial rise or building up of decay curve at around several ns, originating from carrier influx from higher to lower potential dots. We similarly analyze the exciton dynamics in GO because sp^2 carbon clusters are embedded in sp^3 matrix (Figure 2.23), and are consider to work as the QD array.

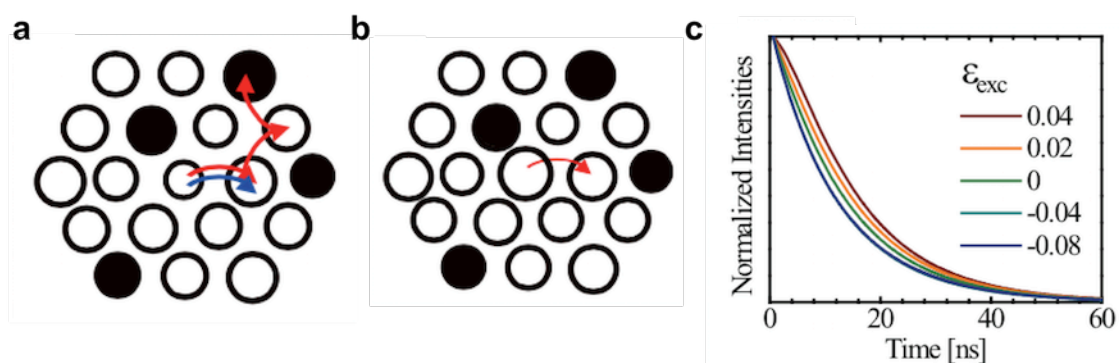


Figure 4.13 Schematic illumination of the exciton in the QD array generated with (a) higher and (b) lower energy excitation. Open and filled circles in the array shows bright and dark QDs, respectively. In this system, exciton in bright QD mainly shows radiative decay, while one in dark QD mainly shows non-radiative decay. (c) Simulated luminescence decay curves as a function of delay time after a pulse excitation with different excitation energy ϵ_{ex} at 300K. (Reproduced from Ref. ¹⁸⁵)

4.6.3. A numerical simulation for the energy transfer

A numerical simulation for the energy transfer has been conducted based on the multi-levels corresponding to various GND states.¹⁸⁵⁻¹⁸⁷ In the model as shown in Figure 4.12b, $\gamma_{R,n}$ and $\gamma_{NR,n}$ denote the radiative and non-radiative decay rate for n th level of exciton, respectively, and W_{mn} denotes the transfer rate of m th to n th level. On excitation, the carriers first show extremely fast relaxation to the exciton states (< 1 ps) as hot carriers.^{188, 189} In the model, the energy of an exciton in a GND migrates to a neighboring nanodisc with multiple-level relaxations. Since the energy transfer is very fast compared with the radiative and non-radiative decay in GO,⁴³ the energy transfer process can predominantly determine the feature of PL decay curve. A possible energy transfer comes from a coupling via incoherent long-range dipolar interactions rather than direct overlapping wavefunctions between neighboring GNDs. This is because the direct overlapping wavefunctions requires strong inter-GND interactions, which is difficult to achieve in the GNDs embedded in sp^3 matrix of GO.¹⁸⁶ The governing equation for the model is described by^{184, 185}

$$\frac{d\rho_n}{dt} = \sum_{m \neq n} W_{mn} \rho_m - \left(W_n + \frac{1}{\tau_{n,R}} + \frac{1}{\tau_{n,N}} \right) \rho_n, \quad (\text{Eq. 4.1})$$

where ρ_n and ρ_m are exciton densities of m th and n th level. $\tau_{n,R}$ and $\tau_{n,N}$ denote the radiative and non-radiative decay time from n th level to ground state, respectively. The transition rate from m th to n th level, W_{mn} , can be written as,¹⁸⁶

$$W_{mn} = \frac{|C_{mn}|^2}{2\pi\hbar^2} \Theta_{mn} \quad (\text{Eq. 4.2})$$

The transition rate depends on a coefficient related to the donor-acceptor Coulomb coupling and the spectral overlap integral Θ_{mn} between m th and n th level. The transition rate from the n th level to a neighboring graphene nanodisc (GND) is described as

$W_n = \sum_{l \neq n} W_{nl}$. The PL and absorption line shapes for m th and n th level are expressed as

Gaussian function.^{187, 190}

$$F_m(\omega) = \frac{\hbar}{\sqrt{2\pi}\sigma_h} \exp[-(\hbar\omega - \varepsilon_m + 2\Delta)^2 / 2\sigma_h^2] \quad (\text{Eq. 4.3})$$

$$A_n(\omega) = \frac{\hbar}{\sqrt{2\pi}\sigma_h} \exp[-(\hbar\omega - \varepsilon_n)^2 / 2\sigma_h^2] \quad (\text{Eq. 4.4})$$

where ε_m is the exciton energy of the m th level and Δ is the lattice reorganization energy with the Stokes shift given by 2Δ . The linewidth of the spectrum is directly related to the Stokes shift and temperature as $\sigma_h^2 = 2\Delta k_B T$.¹⁸⁷ In actual calculation procedure, we assumed discrete energy level of ε_m and ε_n . The value of ε_m and ε_n are estimated from the emission energy and stokes shift. We used ten energy levels of GND states and consider just three successive levels since the difference of the energy between the first and fourth levels are so large that the spectral overlap integral Θ_{mn} extremely small, in other words, the inter-GND interaction is negligible. Then the solution of (Eq. 4.1) can be simplified and given by

$$\rho_n = a_1 \exp(-W_{nn+1}t) + a_2 [\exp(-W_{nn+1}t) - \exp(-W_{n-1n}t)] + a_3 [\exp(-W_{nn+1}t) - \exp(-W_{n-2n}t)], \quad (\text{Eq. 4.5})$$

where a_1 , a_2 and a_3 are fitting coefficients which implicitly contain the magnitude of exciton densities. The solid lines in Figure 3a are drawn using (Eq. 4.5).

The solid lines of Figure 4.12a show the calculated PL decay curves with consideration of energy transfer among the GNDs. The calculated decay curves well reproduce the obtained characteristic PL decay curves the build-up behavior at lower emission energy and the emission-energy-dependent decay features. The calculations and experimental decay curves verify the energy transfer between GND states with various sizes in GOs.

Figure 4.12c shows the derived energy transfer time (inverse of derived decay rate constant) from n th to $n+1$ th level of GND ($W_{n\ n+1}^{-1}$) as a function of emission energy. The energy transfer time increases with decreasing emission energy. This can be understood by the slow relaxation process involving the multiple steps of the energy transfer among neighboring nanodisc states in GO. The derived energy transfer rate is in the range of (~ 10 to 70 ps) $^{-1}$. The saturation of the PLE peak energy above 1.8 eV of monitored emission energy (Figure 4.4d) can be explained from the experimental fact that the larger PL intensity (inset of Figure 4.12a) and longer decay time (Figure 4.12c) in the lower emission energy. At the early stage after excitation with high energy, smaller GND states are resonantly excited, and begin to show the energy transfers to adjacent larger GND states at a high rate. Since the excitons tend to be lower energy states below ~ 2 eV, the steady state PL is observed in NIR rather than in higher emission energy, resulting in the PLE saturation. Therefore, photocarrier can finally relax to larger graphitic region with a zero gap, leading to quenching PL. This energy transfer can cause a decrease of PL quantum yield.

4.7. The effect of protonation and deprotonation

4.7.1. PLE properties

We conducted pH-dependent PL spectroscopy of GO in aqueous solution to investigate the effect of protonation and deprotonation on the optical properties. Figure 4.14a shows PLE maps of GO in solvent of pH 3.4, 4.1, 6.6, and 9.6. In the PLE maps, the emission and excitation peak exhibit redshifts with increasing pH of the solvent. Figure 4.14b and c shows PL and PLE spectra with various pH of the solvent under the condition of 2.1 eV excitation and 1.9 eV emission, respectively. The emission and excitation peak energy as a function of pH of the solvent are plotted in the inset of Figure 4.14b and c, respectively. The emission peak energy gradually decreases from

1.69 at pH 3 to 1.65 eV up to pH 8 and drastically decreases down to 1.55 eV above pH 8. The excitation peak energy decreases with increasing pH.

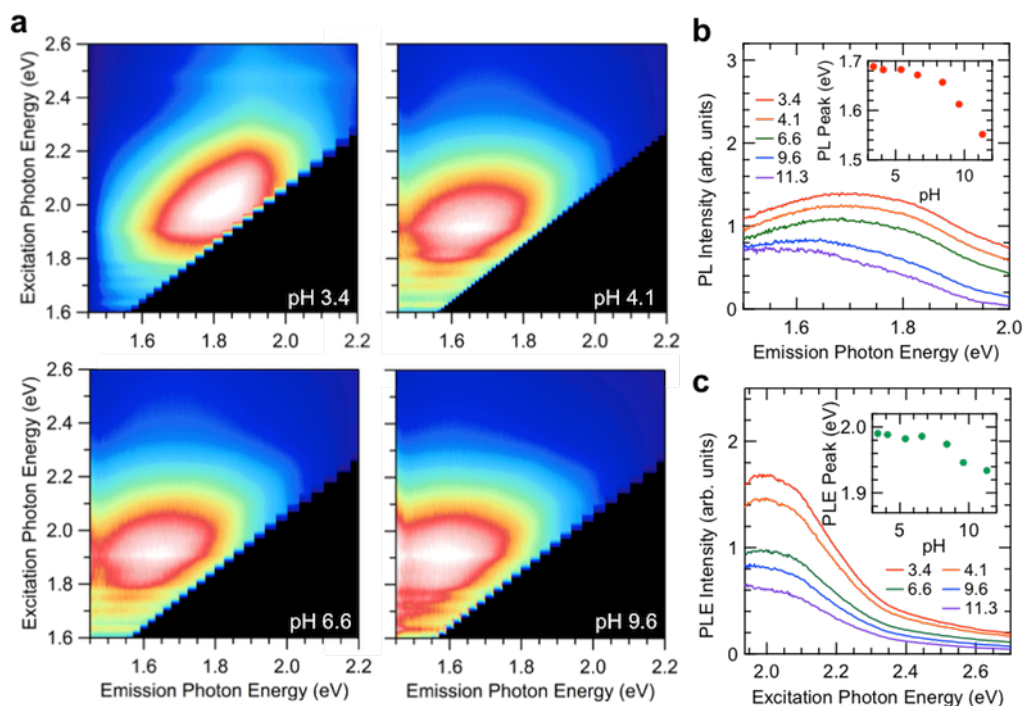


Figure 4.14 (a) PLE intensity maps of GO in solvent at pH 3.4, 4.1, 6.6 and 9.6, respectively. (b) PL and (c) PLE spectra of GO with various pH of the solvent using excitation photon energy of 2.1 eV and emission photon energy of 1.9 eV, respectively. The inset of (b) and (c) is emission and excitation resonance peak energy, respectively, as a function of pH of the solvent.

We also investigate pH-dependent optical absorption of GO as shown in Figure 4.15. In the absorption, no clear features except for a peak near 5.3 eV. This is from π -plasmon absorption.¹⁴¹ The tail of the spectra below 5 eV shows redshift with increasing pH, which is consistent with the redshift of PL and PLE as shown in Figure 4.14. These results are consistent with the redshift of absorption spectra with increasing pH (Figure 4.14), and a previous report on pH-dependent absorption.¹⁹¹

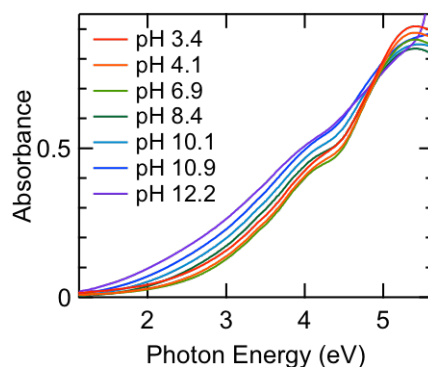


Figure 4.15 Absorption spectra of GO in solvent with various pH of 3.4 to 12.2.

4.7.2. Calculation of the protonation and deprotonation effects

In this Section, we discuss the protonation and deprotonation effects on the optical transitions of GO in order to understand the observed spectral shift in the PL and PLE spectra (Figure 4.14). First we investigate the contribution of hydroxyl and carboxyl groups to the optical transitions. We calculated the GW bandgaps E^{GW} and absorption spectra for C_{96} , C_{96} -OH and C_{96} -COOH (Figure 4.16). E^{GW} is found to decrease by adding both hydroxyl and carboxyl group. The additional functional groups increase the nominal size of GND, as a result, E^{GW} and absorption energy decreases.

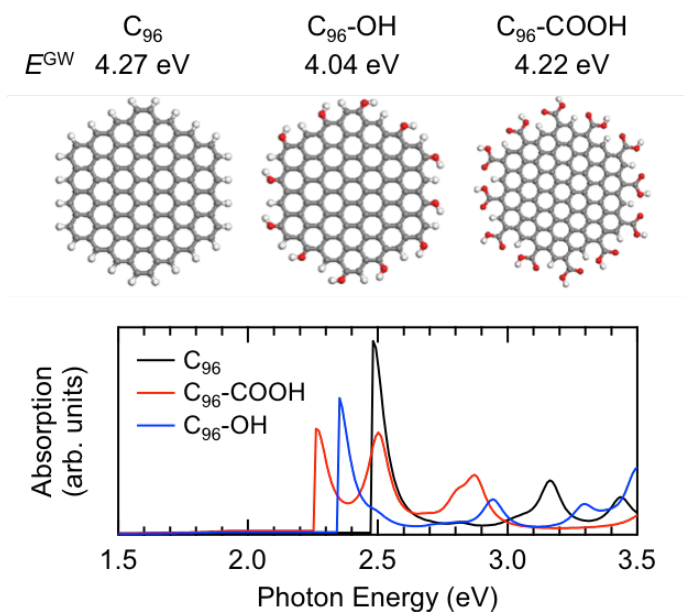


Figure 4.16 Atomic structure and absorption spectra for the hydrogen, hydroxyl and carboxyl terminated GNDs with 96 carbon atoms in the center (top). The white, gray and red ball represents the hydrogen, carbon and oxygen atoms. The GW bandgaps (E^{GW}) is shown above the atomic structure.

We investigate the effect of protonation and deprotonation on electronic structures and excitonic properties using the DFT based on many body perturbation theory. First, hydroxyl and some carboxyl functional groups are substituted with some of hydrogen atoms of C_{96} GND to mimick the GND states within GO (see the upper middle structure in Figure 4.17). The size of the C_{96} GNDs nominally increases from 1.71 to 2.00 nm due to the additional edge functions. As a result, the absorption energy of the protonated GND decreases and the lowest absorption peak (E_{ls}) shows redshift from 2.47 to 1.95 eV (Figure 4.8b and Figure 4.17).

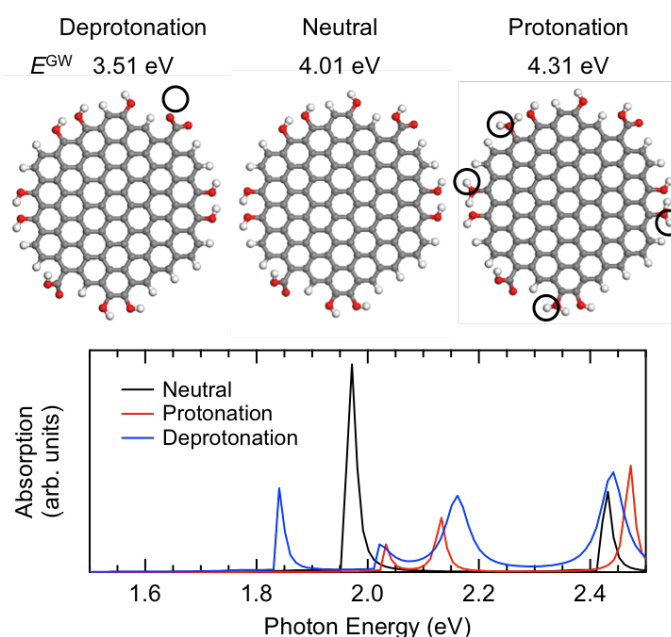


Figure 4.17 Atomic structures and the absorption spectra for GNDs with deprotonation, neutral and protonation, where the black circles represent the positions for the protonation and deprotonation hydrogen atoms. The GW corrected bandgaps are displayed above the atomic structures.

Under the basic condition, the lowest energy of absorption peak shows a redshift of 0.2 eV due to the deprotonation process (see the upper left structure in Figure 4.17). On the other hand, i.e. the acidic condition, the hydroxyl groups are protonated as shown in the upper right structure in Figure 4.17. Consequently, the lowest absorption peak energy of GNDs increases and shows a blue shift by 0.2 eV. The protonation and deprotonation for functional groups can change the electronic structures of GNDs in GO and strongly affect the optical properties of GO. The theoretical results provide the microscopic mechanism of the experimentally observed pH dependent shift in PL and PLE spectra.

4.8. Chapter summary

In this Chapter, we have highlighted the GND states in GO that have an important role of determining its optical properties. We have investigated the mechanism of NIR PL from GO by the experimental results of the static and time-resolved PL excitation spectroscopy and first-principle theoretical calculation. The observed static NIR emission peak in the range from 1.5 to 2.0 eV shows the resonance in the range from 1.8 to 2.3 eV and the emission peak energy depends on the excitation photon energy. The NIR PL originates from ensemble emissions among various sizes of GND states. The time-resolved PL measurements revealed that the PL lifetime is 10 to 70 ps depending on the detected emission energy. The PL decay curves suggested that the photocarriers experiences energy transfers from smaller to larger GND states.

The electronic properties are highly sensitive to the protons around the oxygen functional groups of GND states in GO. The pH-dependent PL spectroscopy and the theoretical calculation have revealed that increase and decrease of bandgap in various pH of solvent are attributed to protonation and deprotonation of oxygen functional groups around the graphitic regions in GO. The theoretical calculations have provided the band gap, transition, and binding energy. The scaling law of the exciton properties manifesting remarkable quantum confinement provides a guideline for designing the new GO engineered with atomic precision. The GND states could be a significant aspect of GO-based optoelectronic devices.

Chapter 5. Photocarrier relaxation pathway in two-dimensional semiconducting transition metal dichalcogenides

5.1. Introduction

So far, we have revealed the characteristic behavior of graphene oxide (GO). In this Chapter, we describe giant light-matter interaction and unique photocarrier relaxation in two-dimensional semiconducting transition metal dichalcogenides (TMDs). GO and TMDs have opposite optical properties. The energy gap of GO can be tuned in wide wavelength range from NIR to UV region because of the abundant functional groups, while TMDs has the rigid energy gap and also need clarification of photocarrier behavior for efficient utilization of the carriers. TMDs are also promising materials for next-generation ultrathin optoelectronic devices. In this Chapter, we describe the detailed mechanism of the giant light-matter interaction and their photocarrier relaxation based on the unique band structures. We note that the calculations based on the *ab initio* density functional theories in this Chapter have been conducted by Dr. Alexandra Carvalho and the co-workers in National University of Singapore, Singapore.

Individual layers of TMDs are excellent light absorbers despite being atomically thin.^{65, 74} Absorption spectra of MX_2 ($\text{M} = \text{Mo}, \text{W}$ and $\text{X} = \text{S}, \text{Se}$) consist of characteristic peaks due to excitonic resonance and interband transitions. Recent *ab initio* studies have attributed the strong light-matter interaction to the “band nesting”, which gives rise to singularity features in the joint density of states (JDOS).¹²⁵ In the nesting region of the band structure, the conduction and valence bands are parallel to each other in the momentum space. The JDOS diverges for the resonance energy, resulting in giant enhancement in the corresponding optical conductivity. While

singularities in the JDOS are present in common semiconductors and metals such as silicon and aluminum, divergence in optical conductivity occur only in low-dimensional materials.¹⁹² The absorption is also enhanced for photon energies corresponding to transitions between van Hove singularity peaks in the DOS, which are attributed to heavy effective mass of carriers in MX_2 compounds.^{104, 125}

Since absorption is highly efficient in the resonance conditions, understanding photocarrier relaxation dynamics is crucial in implementing these materials into light harvesting devices such as photovoltaic cells or photodetectors. Photocarriers generated in the band nesting region are of particular interest as the electrons and holes are expected to relax at the same rate, but with opposite momentum. In this Chapter, we examine the relaxation processes of photoexcited carriers in mono- and bilayer MX_2 using photoluminescence excitation (PLE) spectroscopy and *ab initio* density functional theory (DFT) calculation. We show that the relaxation channel of the photoexcited carriers is strongly dependent on the excitation energy (Figure 5.1). The findings reveal the unique implication of 2D band structure and the characteristic photocarrier relaxation.

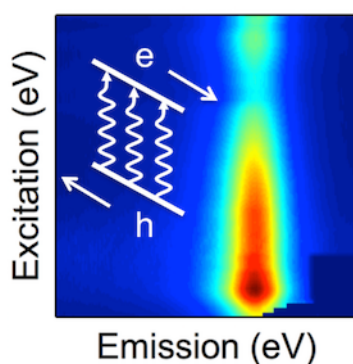


Figure 5.1 Schematic PLE intensity map of 2D semiconducting TMDs. The inset exhibits that the electrons and holes that generated in the band nesting relax at the same rate, but with opposite momentum.

5.2. Sample preparation

The samples used in this study were monolayer (and bilayer) MoS₂, MoSe₂, WS₂ and WSe₂ crystalline flakes. For MoS₂, we studied mechanically exfoliated flakes as well as chemical vapor deposition (CVD)-grown samples. Figure 5.2 shows the typical optical microscope images of monolayer mechanically exfoliated and CVD-grown MoS₂ deposited on quartz substrates. Monolayer MoS₂ on quartz substrate was directly grown by CVD following Ref. ¹⁴⁰. In the CVD growth, MoO₃ (Alfa Aesar) and Sulfur (Sigma Aldrich) were used as a precursor. The CVD reaction was performed in a quartz tube at up to 700 °C under atmospheric pressure with flowing pure nitrogen gas. Single bulk crystals of MoSe₂, WS₂ and WSe₂ were grown by chemical vapor transport using iodine as the transport agent following Ref. ¹⁹³. The crystals were mechanically exfoliated and deposited on quartz substrates. In the mechanical exfoliation, a few small pieces of single crystals (~ 1 mm) were placed on a sheet of scotch tape. The sticky-sides are attached and peeled several times, and placed on a quartz substrate. The tape was rubbed gently and peeled slowly to transfer MX₂ flakes onto the substrate.

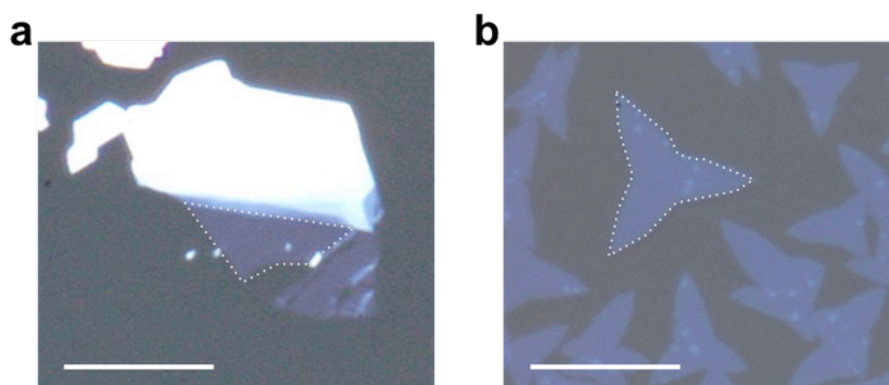


Figure 5.2 Typical optical microscope images of monolayer (a) mechanically exfoliated and (b) CVD-grown MoS₂ deposited on quartz substrates. A part of monolayer regions is highlighted by dotted lines. The scale bars correspond to 10 μm .

5.3. Optical measurements

Schematic diagram and photograph of the confocal optical system for PLE measurements are shown in Figure 5.3. The micro-PL spectra under a back scattering geometry were collected to a Si CCD array (Andor, iDus401) dispersed in a spectrometer built with a monochromator (NT-MDT, NTEGRA Spectra). The excitation light source was a super-continuum light (Fianium, SC-450) coupled to a tunable laser filter (Photon-etc, TLS VIS-2). Extra ray is cut by short pass filter (Edmund, hard coated OD4 bandpass filter kits 400-700 nm-25 mm) after the tunable laser and long pass filter (Thorlabs, FELH500, FELH550, FELH600, FELH650, FEL700 and FELH750) in front of the spectrometer. The Si CCD detector was cooled by Peltier system down to $-70\text{ }^{\circ}\text{C}$. The laser spot was focused through 100x objective lens (Olympus, MPLFLN100x, numerical aperture 0.90) and its excitation intensity for PL and PLE measurements was kept below $10\text{ }\mu\text{W}$ in which the effect of optical non-linearity is negligible (see Section 5.8). The measured spectral data were corrected for variations in the detection sensitivity with the correction factors obtained by using a standard tungsten-halogen lamp. The Raman measurements were also conducted with the same apparatus with except the excitation light source. A Diode laser was used as the light source, which emits 2.33 eV photon below $50\text{ }\mu\text{W}$. The number of grooves in the diffraction grating was 100 grooves/mm for the PL and PLE measurements and 2400 grooves/mm for the Raman measurements.

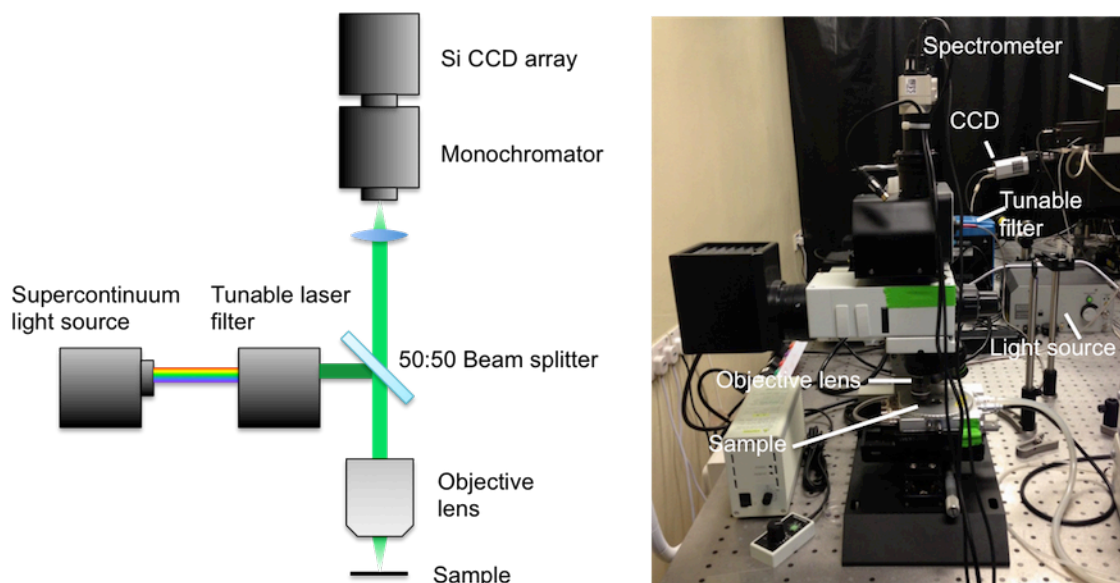


Figure 5.3 Schematic diagram and photograph of the confocal optical system for PLE measurements.

The measurements of differential reflectance were performed using a tungsten-halogen lamp (Zolix, LSH-T150, 150 W) as a light source instead of the super-continuum light as shown in Figure 5.4. The diameter of the lamp beam was adjusted through a pinhole on a sheet of black paper down to ~ 1 mm to illuminate the desired region of the sample. In order to obtain the reflection only from the sample, an aperture loaded in the spectrometer was adjusted into as small diameter as possible and the region of interest in the CCD pixels was limited on the sample not to pick up the reflection of the quartz substrates. The differential reflectance is defined as $(R_{S+Q} - R_Q)/R_Q$, where R_{S+Q} and R_Q are the reflected light intensities from the quartz substrate with and without the material, respectively.^{50, 193, 194}

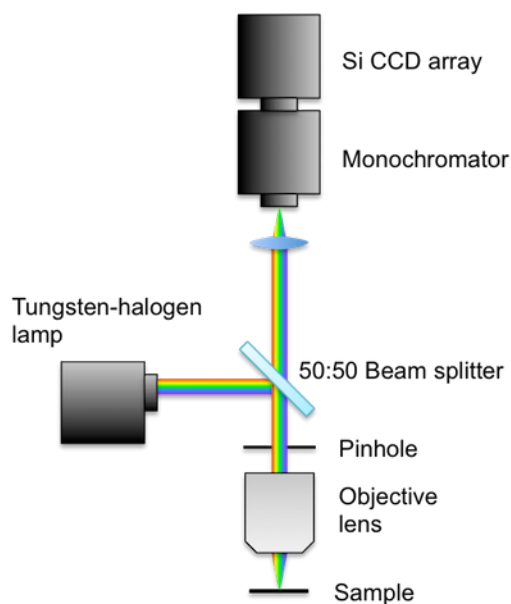


Figure 5.4 Schematic diagram of the apparatus for the reflection measurements.

5.4. Theoretical calculations

We performed a series of DFT calculations for the semiconductor TMDs family using the open source code QUANTUM ESPRESSO.¹⁹⁵ The JDOS, the dielectric permittivity, and the optical conductivity were calculated using a modified version of the epsilon program of the QUANTUM ESPRESSO distribution to account for full relativistic calculations. We calculated the optical conductivity directly from the band structure.¹⁹⁵ We used norm-conserving, fully relativistic pseudopotentials with nonlinear core-correction and spin-orbit information to describe the ion cores. The pseudopotentials used were either obtained from the QUANTUM ESPRESSO distribution or produced using the ATOMIC code by A. Dal Corso. The exchange correlation energy was described by the generalized gradient approximation (GGA), in the scheme proposed by Perdew, Burke, and Ernzerhof (PBE).¹⁹⁶ The integrations over the Brillouin zone were performed using a scheme proposed by Monkhorst-Pack¹⁹⁷ for all calculations. Single-layer samples were modeled in a slab geometry by including a vacuum region of 45 bohr in the direction perpendicular to the surface. A grid of

$16 \times 16 \times 1$ \mathbf{k} points was used to sample the Brillouin zone. The energy cutoff was 50 Ry. The atomic positions were optimized using the Broyden-Fletcher-Goldfarb-Shanno (BFGS) method for the symmetric structure. The lattice parameter a was determined by minimization of the total energy. A Gaussian broadening of 0.05-eV width was applied in the optical conductivity. It is well known that GGA underestimates the band-gap,¹²⁸ and hence the optical conductivity shows the peaks displaced towards lower energies relative to actual experiments. However, their shapes and intensities are expected to be correct.

5.5. Characterization of the samples

The number of layers of MX_2 was verified by PL, differential reflectance, Raman spectra (2.33 eV excitation), and atomic force microscopy. Figure 5.5a shows schematic illustration of the typical Raman modes for the bulk MX_2 . The main Raman peaks correspond to the out-of-plane A_{1g} mode and in-plane E_{2g}^1 mode as illustrated in Figure 5.5a. With decreasing the layer thickness, the frequency of A_{1g} mode decreases and that of E_{2g}^1 increases. The origin of the shifts is attributed to the influence of neighboring layers on the effective restoring forces on atoms and the increase of dielectric screening of long-range Coulomb interactions.^{46, 198} The peak shifts tell the thickness, that is the number of layers can be identified by the wavenumber difference between the main two peaks. Figure 5.5b and c show Raman spectra for the samples that we used in this study. For example, the monolayer of MoS_2 exhibits the wavenumber difference between A_{1g} and E_{2g}^1 modes as $\sim 20 \text{ cm}^{-1}$, while that of bilayer increases to $\sim 22 \text{ cm}^{-1}$ as shown in Figure 5.5.¹⁹⁹

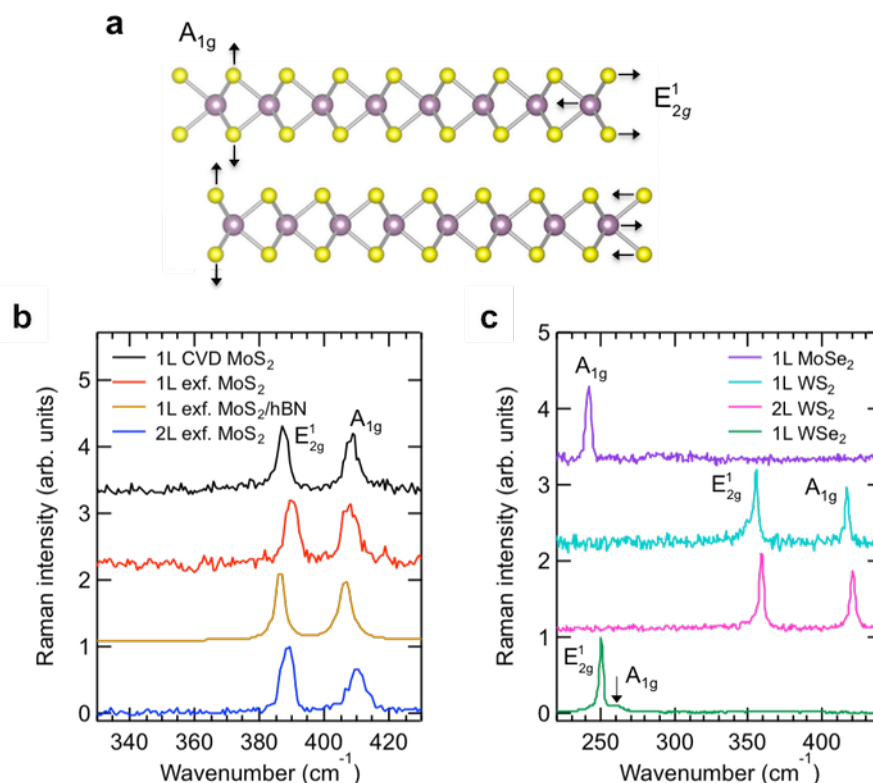


Figure 5.5 (a) Schematic illustration of the out-of-plane phonon mode A_{1g} and the in-plane phonon mode E_{2g}^1 for the bulk MX_2 . Raman spectra for (b) monolayer CVD-grown MoS_2 , monolayer mechanically exfoliated MoS_2 , MoS_2 on hBN, and bilayer mechanically exfoliated MoS_2 excited at 2.33 eV. (c) Raman spectra of monolayer mechanically exfoliated $MoSe_2$, WS_2 , bilayer mechanically exfoliated WS_2 , and monolayer WSe_2 excited at 2.33 eV.

The AFM measurements also tell us the number of layers for TMDs. As we mentioned in Section 2.2.2, the honeycomb lattice of the atomically thin layers are stacked along c-axis, the monolayer thickness of MoS_2 is 0.6 nm for S-Mo-S structures, and the interlayer spacing is ~ 6.5 Å.^{46, 49, 200} The AFM images and the height profiles of monolayer (0.83 nm) and bilayer (1.96 nm) in Figure 5.6 agree well with these values and also we identify the number of layers from the AFM measurements. The Raman spectra and the thickness obtained from AFM measurements agree well with previous

reports. 49, 201, 202

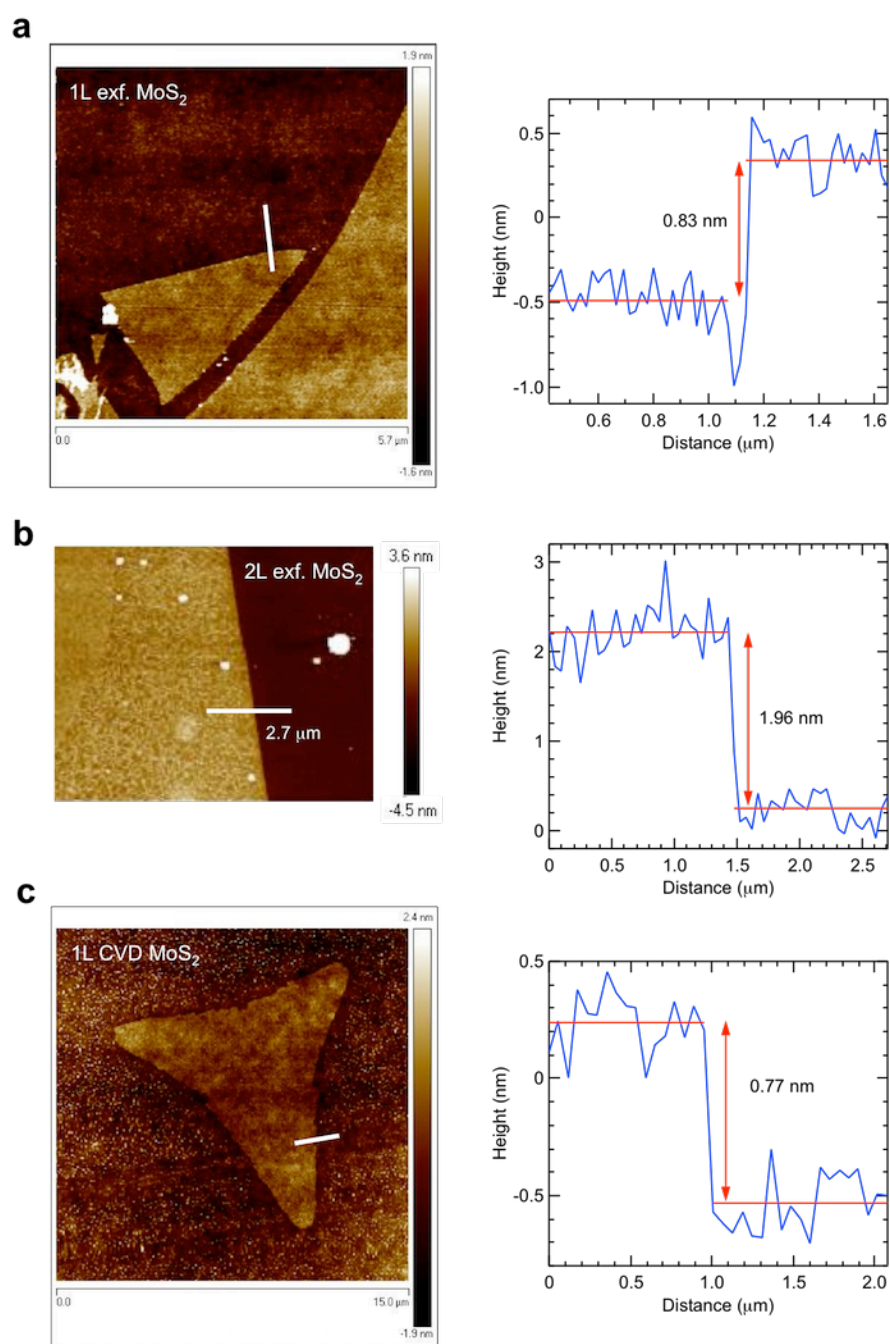


Figure 5.6 AFM images and height profiles for (a) monolayer mechanically exfoliated, (b) bilayer MoS₂ and (c) CVD-grown monolayer MoS₂.

5.6. Band nesting and optical response

Large optical response due to the phenomenon of “band nesting” is theoretically predicted for 2D semiconducting TMDs.¹²⁵ Figure 5.7a shows energy band structures and DOS of monolayer MoS₂. In band nesting, conduction and valence bands are parallel to each other in energy of the energy band structure. The largest absorption is often considered to be in van Hove singularities (VHS) of the DOS rather than at the bandgap edge. If there are VHS both in the conduction and valence bands at a given point of momentum space, there will be a singularity of the optical conductivity.

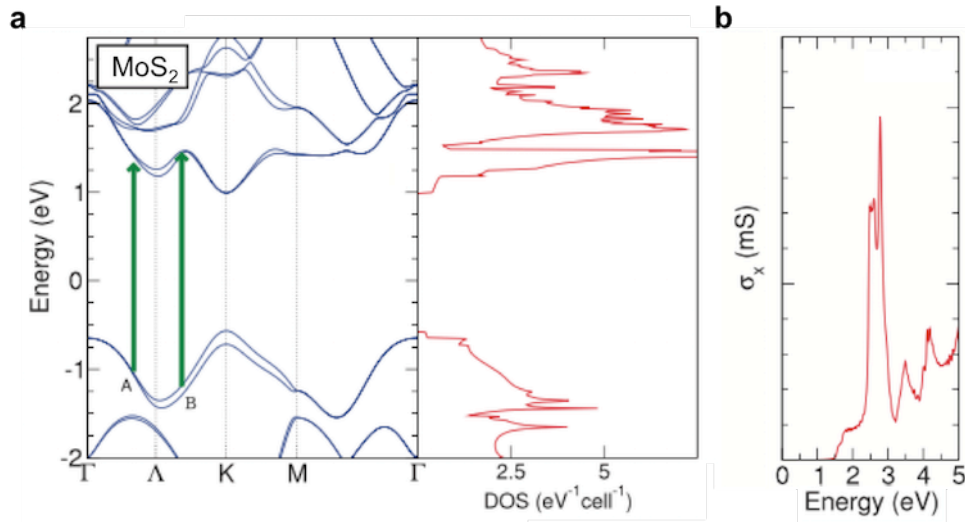


Figure 5.7 (a) Energy band structures, DOS and (b) optical conductivity σ_x of monolayer MoS₂ calculated using *ab initio* density functional theory. The arrows indicate the transitions corresponding to the first pronounced peaks in the optical conductivity. (Reproduced from Ref. ¹²⁵)

The optical conductivity of materials can be described as^{125, 192}

$$\sigma_1(\omega) = \kappa_2(\omega)\omega\epsilon_0, \quad (\text{Eq. 5.1})$$

where $\kappa_2(\omega)$ is the imaginary part of the relative electric permittivity, ω is the frequency of the incoming electromagnetic radiation, and ϵ_0 is the vacuum permittivity. In the optical dipole approximation, we can write $\kappa_2(\omega)$ as

$$\kappa_2(\omega) = \frac{4\pi^2 e^2}{m^2 \omega^2} \int_{BZ} \frac{d^2 \mathbf{k}}{(2\pi)^2} |d_{vc}|^2 \delta(E_c - E_v - \hbar\omega), \quad (\text{Eq. 5.2})$$

where e is the electric charge, m is the carrier mass and d_{vc} is the dipole matrix element. The sum is over the occupied states in the valence band (v) and the unoccupied states in the conduction band (c) with energy E_v and E_c . The integral is evaluated over the entire 2D Brillouin zone. If we consider cross section $S(E)$ of constant energy E , $E = \hbar\omega = E_c - E_v$, in the band structure, we can express

$$d^2 \mathbf{k} = dS \frac{d(E_c - E_v)}{|\nabla_k(E_c - E_v)|} \quad (\text{Eq. 5.3})$$

and the integral (Eq. 5.2) can be rewritten as

$$\kappa_2(\omega) = \frac{4\pi^2 e^2}{m^2 \omega^2} \sum_{v,c} \frac{1}{(2\pi)^2} \int_{S(\omega)} \frac{dS}{|\nabla_k(E_c - E_v)|} |d_{vc}|^2 \quad (\text{Eq. 5.4})$$

If d_{vc} varies slowly over these regions, or d_{vc} vanishes except near special k because of symmetry, we can describe

$$\kappa_2(\omega) \approx \frac{4\pi^2 e^2}{m^2 \omega^2} \sum_{v,c} |d_{vc}|^2 \rho_{vc}(\omega), \quad (\text{Eq. 5.5})$$

where

$$J_{vc}(\omega) = \frac{1}{(2\pi)^2} \int_{S(\omega)} \frac{dS}{|\nabla_k(E_c - E_v)|} \quad (\text{Eq. 5.6})$$

is the joint density of states (JDOS).

It should be noted that the strong peaks in the optical conductivity will come from regions or points in the spectrum, where $|\nabla_k(E_c - E_v)| \approx 0$. The points are called critical points and can be classified as several types. One classifies three types of critical points which we denote by C_0 , C_1 and C_2 . The subscripts indicate the number of coefficients which are negative. At the minimum (C_0) and maximum (C_2) JDOSs exhibit a step function singularity, while at the saddle point C_1 a logarithmic singularity occurs as

shown in Table 5.1. If $\nabla_k E_c = \nabla_k E = 0$, the points, C_0 , C_1 and C_2 occur in each band. These points are often spotlighted because they are easy to be pointed out by inspection by visual inspection of the band structure, and cause singularities in the DOS (Figure 5.7a). On the other hand, the condition of $\nabla_k(E_c - E_v) = 0$ with $|\nabla_k E_c| \approx |\nabla_k E_v| > 0$, that is “band nesting”, gives rise to singularities of the JDOS and therefore exhibits high optical conductivity as described in (Eq. 5.6) (Figure 5.7b). While singularities in the JDOS are present in common semiconductors and metals such as silicon and aluminum, divergence in optical conductivity occur only in low-dimensional materials.¹⁹²

Table 5.1 Analytic behavior and schematic representation of JDOS ($J(E)$) near critical points for the 2D system. For convenience $A = (8\pi/c)h^{-2}(m_x m_y)^{1/2}$, E_0 is a resonant energy and B indicates a constant which depends on the detailed band structure. m_x And m_y are the electron mass along the x and y direction (under the condition of confinement along the z direction), respectively. (Taken from Ref. ¹⁹²)

Critical Point	Joint density of states	Schematic representation
C_0 Minimum	$J(E) = \begin{cases} B + O(E - E_0) & \text{when } E < E_0 \\ B + A + O(E - E_0) & \text{when } E > E_0 \end{cases}$	
C_1 Saddle point	$J(E) = B - \frac{A}{\pi} \ln \left 1 - \frac{E}{E_0} \right + O(E - E_0)$	
C_2 Maximum	$J(E) = \begin{cases} B + A + O(E - E_0) & \text{when } E < E_0 \\ B + O(E - E_0) & \text{when } E > E_0 \end{cases}$	

5.7. Strong light absorption

Semiconducting group 6 TMDs consist of strongly bonded two-dimensional X-M-X layers that are held together by weak van der Waals forces.^{45, 104} Lattice structures of monolayer and bilayer MX_2 are shown in Figure 5.8a. Each layer of the M and X atoms forms a two-dimensional hexagonal structure. Monolayer MX_2 is noncentrosymmetric, while bilayer and bulk materials exhibit inversion symmetry.²⁰³ The bandgap is direct for monolayer MX_2 in contrast to indirect gap of bilayer and thicker multilayers.^{49, 50} Since group 6 MX_2 is isoelectronic, the general features of the electronic structure are similar. The band structure of monolayer MoS_2 calculated by the DFT is shown in Figure 5.8b. For monolayer MX_2 , the conduction band minimum (CBM) and the valence band maximum (VBM) are both at the K point of the Brillouin zone.^{106, 128, 204-206} Conduction band valley at the Λ point and the valence band hill at the Γ point play a dominant role in the direct to indirect gap crossover. Band nesting regions in Mo and W disulphide and diselenide monolayers occur midway between the Γ and Λ points.¹²⁵

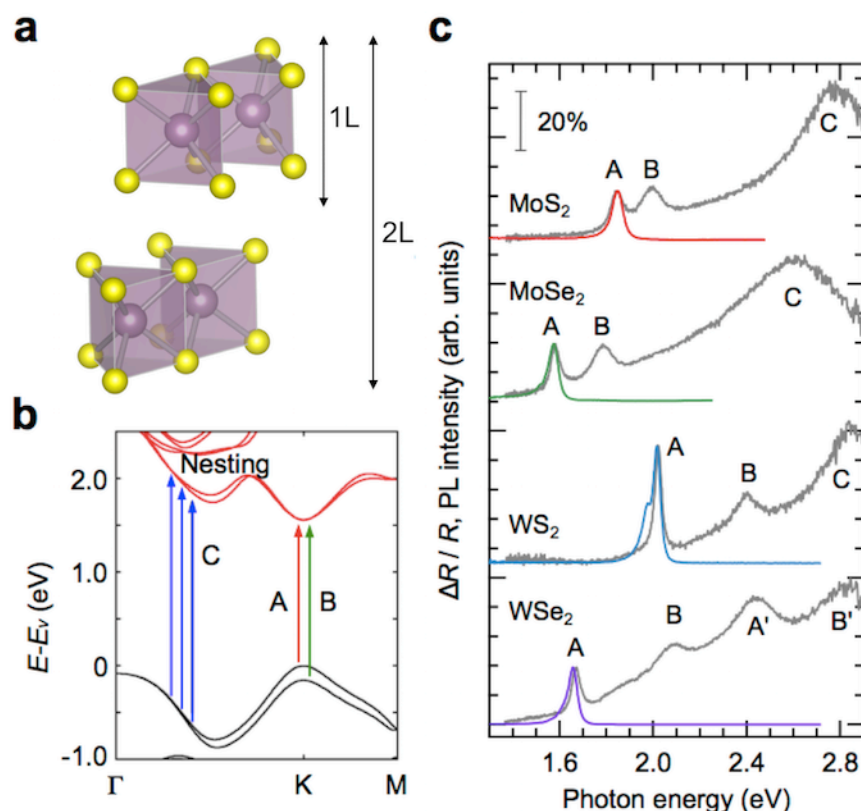


Figure 5.8 Properties of monolayer MX₂. (a) Lattice structures of monolayer and bilayer MX₂. (b) The band structure of monolayer MoS₂ calculated by the DFT with the label of A, B, C. The arrows indicate the transition in A, B and the band nesting C. (c) PL spectra (red, green, blue and purple curves) from excitation at the C (A' for WSe₂) peak and differential reflectance spectra (gray curves) of monolayer MX₂ flakes on quartz substrates. The scale bar indicates 20% absorption based on differential reflectance spectra. The PL intensity is normalized by the A exciton peak of the differential reflectance spectra for each material and the spectra are displaced along the vertical axis for clarity.

The optical signatures of the MX₂ materials reflect basic features of the energy band structure. Figure 5.8c shows the PL and differential reflectance ($\Delta R/R$) spectra of monolayer MoS₂, MoSe₂, WS₂ and WSe₂ on a quartz substrate, where $\Delta R/R$ is described by^{75, 193, 207}

$$\Delta R / R = \frac{R_{s+q} - R_q}{R_q} = \frac{4}{n_q^2 - 1} Abs. \quad (\text{Eq. 5.7})$$

R_{s+q} is the reflectance of the sample on the quartz substrate, R_q is the reflectance of the quartz substrate, n_q (~ 1.5) is refractive index of quartz, and Abs is absorbance of the sample. The (Eq. 5.7) is valid for a layer of material with much smaller thickness than the wavelength of light, that is supported by thick transparent substrate.⁷⁵ The differential reflectance is an effective measure of the absorbance for ultrathin samples.¹⁹³ The resonance peaks A and B (labeled according to earlier conventions²⁰⁶) correspond to excitonic transitions occurring at the K/K' points of the momentum space (See Figure 5.8b).^{49, 110, 194} The PL peak of the monolayer MX_2 is located at A peak of the differential reflectance spectra, suggesting that the PL feature corresponds to the band edge emission at the K point. Strong light absorption at higher energies (C peak for MoS_2 , WS_2 , and MoSe_2), which is estimated to be above 30% based on reflectance and transmittance measurements, arises from near-degenerate exciton states.¹²⁹ In a single-electron band picture, this feature corresponds to region of the Brillouin zone, where the valence and conduction bands are nested.¹²⁵ The absorption features of WSe_2 are typically more complex due to strong effects of the Se p orbitals²⁰⁶ but the strong absorption above ~ 2.4 eV may be attributed partly to band nesting.

5.8. Excitation power-dependent PL properties of monolayer WSe_2

In the series of PL and PLE measurements, we used low power excitation power below $10 \mu\text{W}$ on the sample in the series of optical measurements. To verify the low power conditions, we conducted excitation power-dependent PL measurements for monolayer WSe_2 . The spectral shape does not exhibit significant change with excitation below $10 \mu\text{W}$ of 2.43 eV light (Figure 5.9a). The emission tail at lower energy (Figure 5.9a) and PL saturation (Figure 5.9b) are observed above $10 \mu\text{W}$ excitation. From these

results, we used low power excitation below 10 μW to avoid PL saturation and heating effects by the optical excitation.

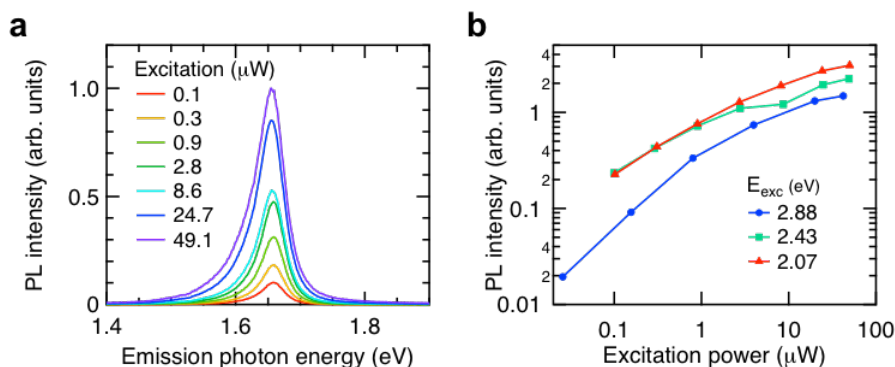


Figure 5.9 Excitation power-dependent PL spectra of monolayer WSe_2 . (a) PL spectra with various excitation power and (b) PL intensity as a function of excitation power for monolayer WS_2 , where E_{exc} is the excitation energy.

5.9. Effect of band nesting

The calculated band structure indicates that excited electrons and holes in the nesting region relax to their immediate band extremum (see Figure 5.8b). This corresponds to Λ valley and Γ hill for electrons and holes, respectively. The intraband relaxation is known to be extremely fast (< 500 fs) in mono- and few-layer MoS_2 and dominates other relaxation processes (see more information in Table in Appendix).²⁰⁸⁻²¹⁰ The electron-hole pairs separated in the momentum space requires emission or absorption of a phonon and should be a slow process, resulting in low yield emission by the radiative recombination following the separation. The carrier lifetime in the indirect emission process can be estimated to be on the order of 1 ns based on previous studies.^{208,211} On the other hand, direct excitons exhibit lifetime on the order of 100 ps with correspondingly higher QY.²⁰⁹ Here, we investigate the effect of band nesting on the behavior of photoexcited electron-hole pairs in monolayer MX_2 by studying their excitation-dependent PL QY. To obtain micro-PLE spectra from

micrometer-sized flakes of mechanically exfoliated samples, we utilized a supercontinuum light source coupled to a tunable laser filter as the excitation source. The excitation power was kept constant and low to avoid undesired nonlinear effects.

Figure 5.10 shows the PLE intensity map of monolayer (a) MoS₂, (b) MoSe₂, (c) WS₂ and (d) WSe₂ flakes and comparisons between the PLE spectra (red plots), relative QY of emission (blue dots) and the differential reflectance spectra (gray lines). The relative QY is estimated by dividing the integrated PL intensity by the absorption at the excitation energy. It can be seen that the PLE intensity is enhanced when the excitation is in resonance with the B exciton absorption. In contrast, for MoS₂ and MoSe₂, the PLE intensity at the C absorption peak is suppressed or only weakly enhanced. We note that similar suppression of the PLE is seen for WS₂ and WSe₂ for excitation near the C and B' absorption peaks, respectively. In all cases, the relative QY drops consistently for excitation energies above the B peak resonance. We attribute this behavior to the spontaneous separation of electron-hole pairs in the momentum space due to band nesting.

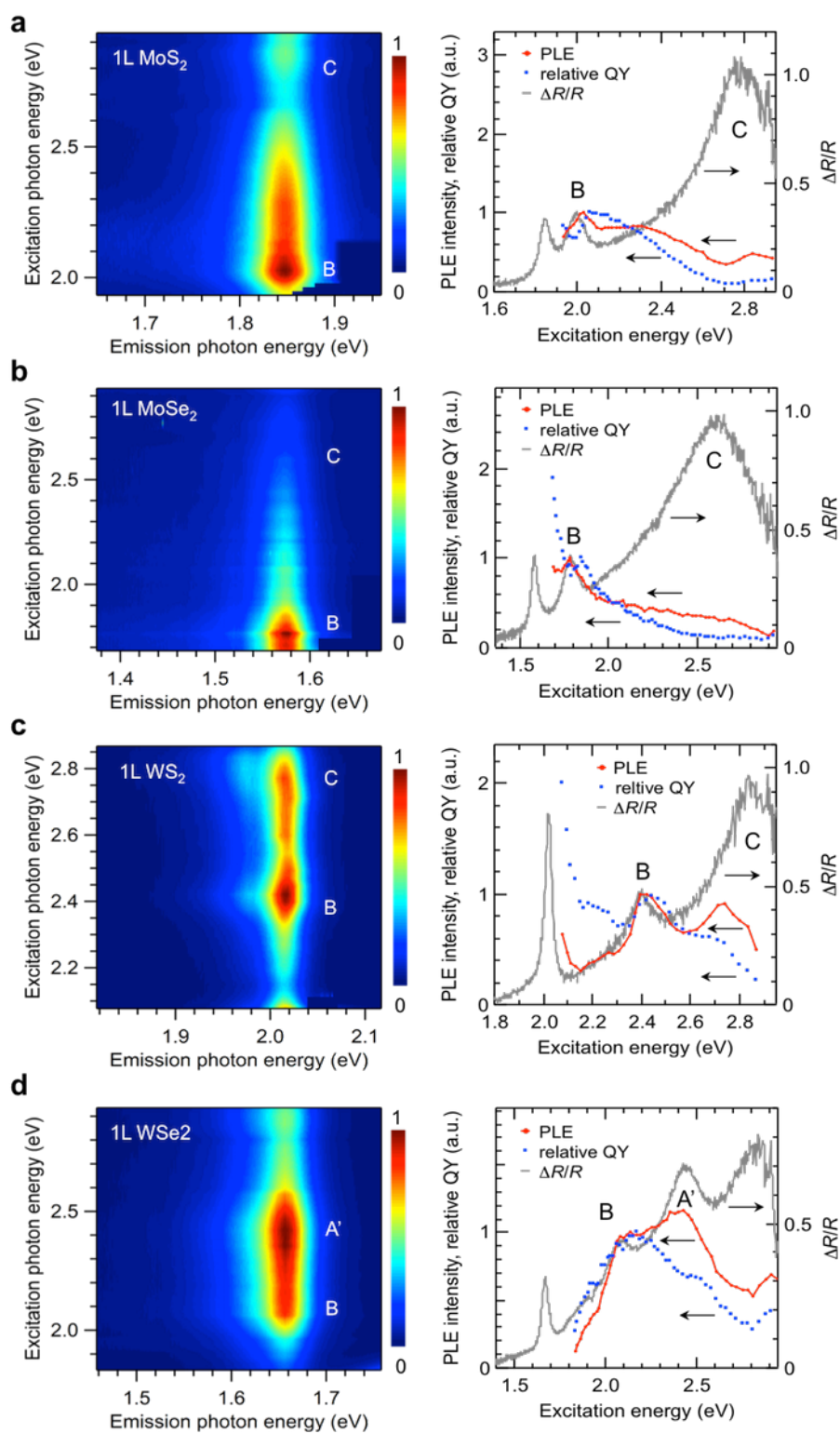


Figure 5.10 PLE spectra of monolayer MX₂. PLE intensity map (left panel), PLE spectra and relative QY of emission (right panel) for bandgap emission for monolayer (a) MoS₂, (b) MoSe₂, (c) WS₂ and (d) WSe₂ flakes. Differential reflectance spectra are

also shown for comparison. The PLE spectra are based on the integrated intensity of the A peak in the PL spectra at each excitation energy. Each PLE spectrum is normalized by the B exciton peak of each material.

In order to further verify this effect, we studied the PLE properties of bilayer MoS₂. The PLE intensity map of the bilayer MoS₂ is shown in Figure 5.11a and exhibits two emission features at 1.45 and 1.85 eV corresponding to indirect and direct emissions. Figure 5.11b shows the PLE spectra and the differential reflectance spectrum is also shown for comparison. The absorption features of bilayer samples are similar to those of monolayers, exhibiting excitonic resonance peaks A and B and strong C peak absorption due to band nesting as shown in Figure 5.11b. Figure 5.11c shows PL spectra of bilayer MoS₂ collected with excitation energy of 2.02, 2.38, 2.48, 2.76 eV. According to previous studies,^{193, 205} bilayer MoS₂ exhibit indirect bandgap emission involving Λ valley in the conduction band and Γ point in the valence band. Thus, we expect enhancement in the bandgap indirect emission when the carriers are excited in the band nesting region. The PLE spectrum of the indirect peak (I) shows a distinct enhancement at the C absorption peak (Figure 5.11b). On the other hand, the A emission peak shows relatively weaker enhancement in this energy range (Figure 5.11b). Figure 5.11d shows the evolution of the ratio of indirect (I) and direct (A) peak. It may be noted that the bandgap emission QY of bilayer samples was distinctly smaller (~ 4 times) than that of monolayer samples (both mechanically exfoliated) for B peak excitation. In contrast, this ratio was only 2.6 for C peak excitation. These results further demonstrate that the photocarrier relaxation pathways and the radiative emission channels are uniquely related to band nesting. Similar results were obtained for bilayer WS₂ as shown in Figure 5.12.

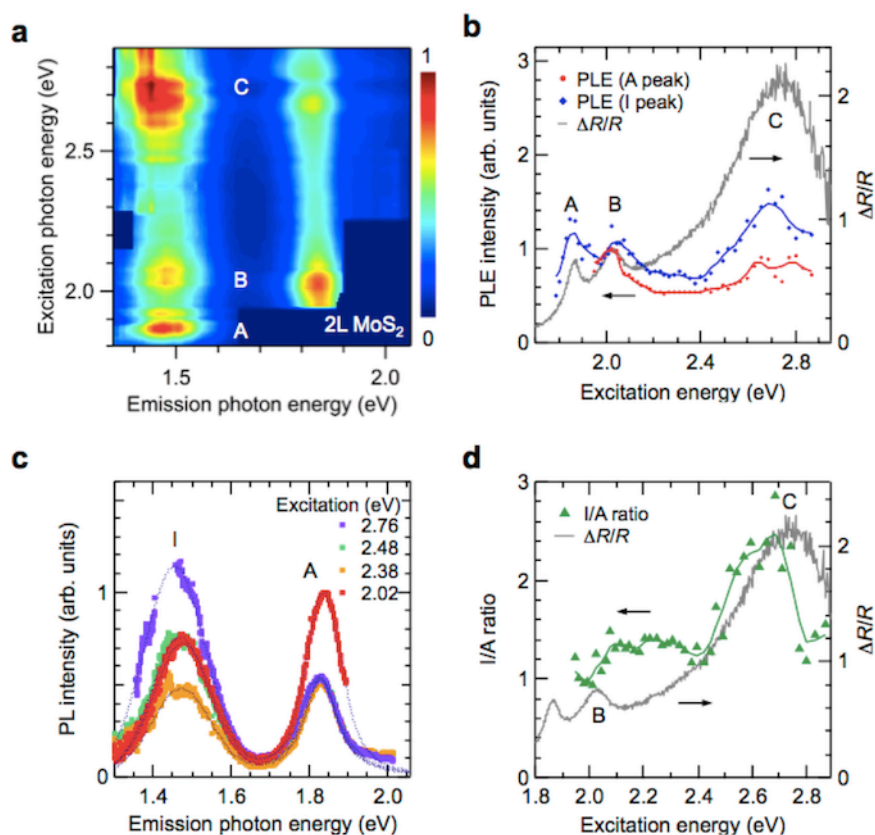


Figure 5.11 PLE spectra of bilayer MoS₂. (a), (b), PLE intensity map and PLE spectra for bilayer MoS₂. The PLE spectra are based on the integrated intensity of the A and I peak in the PL spectra at each excitation energy. The differential reflectance spectrum is also shown for comparison. The PLE spectrum of the A peak is normalized by the B exciton peak of the differential reflectance and the PLE of the I peak is multiplied by the same factor as the PLE spectrum of the A peak. (c), PL spectra collected with excitation energy of 2.02, 2.38, 2.48, 2.76 eV. (d), The ratio of integrated PL intensity between the I and A peak as a function of excited energy. The differential reflectance spectrum is also shown for comparison.

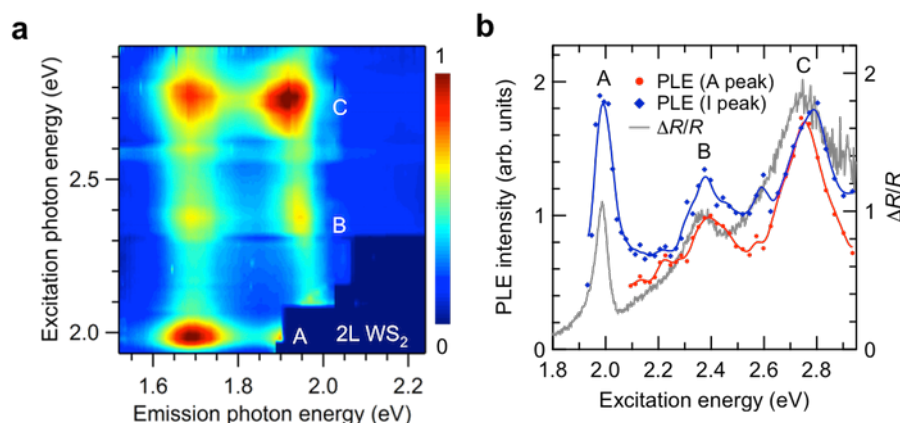


Figure 5.12 PLE spectra of bilayer WS₂. (a) PLE intensity map and (b) PLE spectra for bilayer WS₂. The PLE intensity is evaluated as an integrated intensity of A and I peak in the PL spectra at each excitation energy. The differential reflectance spectrum is also shown for comparison. The PLE of A peak is normalized by the B exciton peak of the differential reflectance and the PLE of I peak is multiplied by the same factor as the PLE of A.

5.10. Comparison of photoluminescence excitation properties with preparation methods

Monolayer MoS₂ flakes obtained by various preparation methods were studied to compare the relaxation process of photoexcited carriers. We measured PLE for mechanically exfoliated flakes of MoS₂ on quartz and MoS₂ on hexagonal boron nitride (hBN) substrates as well as chemical vapor deposition (CVD)-grown samples. Figure 5.13a displays PL spectra for the monolayer CVD-grown, exfoliated MoS₂ and MoS₂/hBN. The spectra of exfoliated MoS₂ on quartz and hBN substrates are multiplied by a factor of 40 and 2.5 for comparison. Relatively lower peak energy and broadening of PL for exfoliated MoS₂ suggests higher carrier doping level and showing charged exciton (trion) recombination.^{54, 60-62} Relatively small PL intensity can be attributed to low decay rate of radiative recombination. MoS₂ deposited on hBN is expected to show

strong PL due to change in the doping level and reduced non-radiative decay channels due to substrate defects.^{51,212} Figure 5.13 shows PLE map, spectra, and relative QY of emission for exfoliated monolayer MoS₂ on (b) quartz and (c) hBN substrates. In either case, weak enhancement in the emission intensity at the C peak excitation was observed, is similar to the case of CVD-grown MoS₂ discussed in Section 5.9. This result suggests that the effect of band nesting is intrinsic in MX₂. Some differences are, however, observed in the ratio of the emission QY for B peak and C peak excitation. This is possibly due to changes in the non-radiative recombination rate k_{nr}^i and intervalley scattering rate k_{iv} .

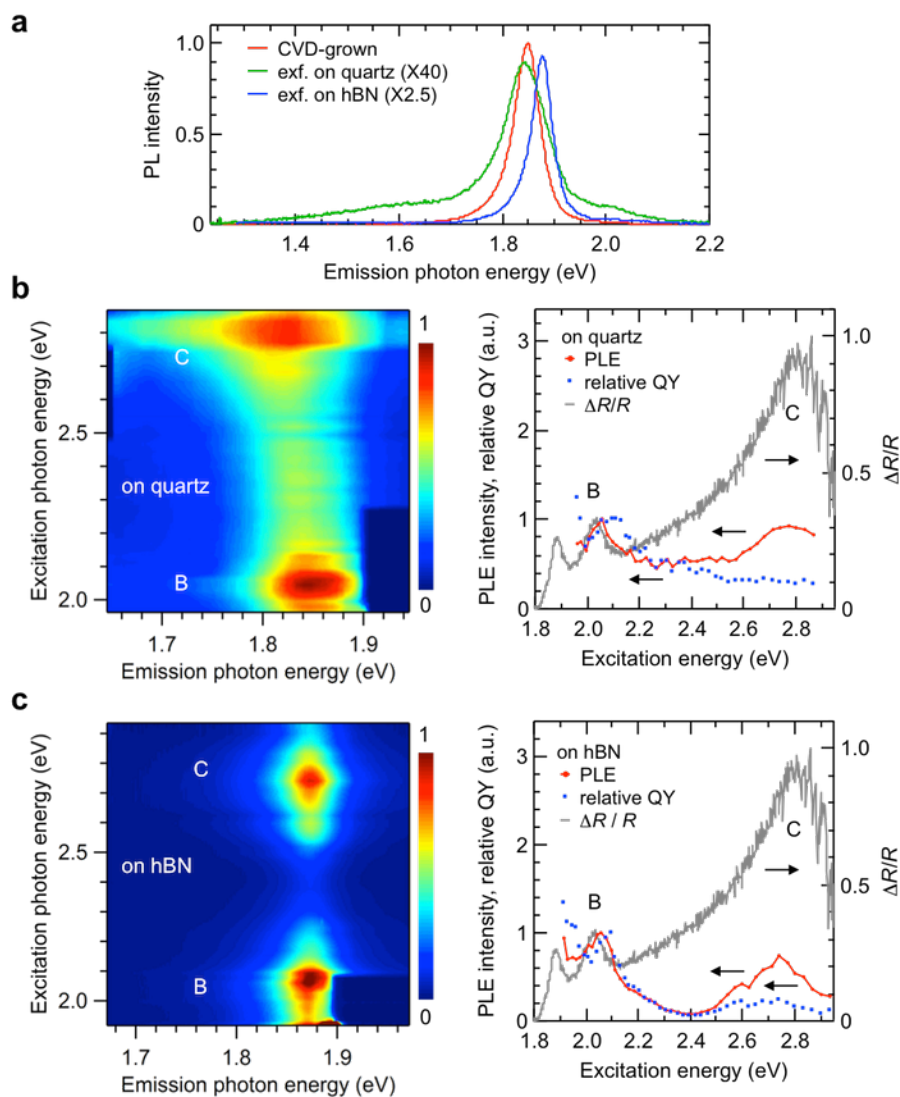


Figure 5.13 PL and PLE spectra of monolayer MoS₂. a, PL spectra for monolayer CVD-grown, exfoliated MoS₂ on quartz and hBN substrates. PLE intensity map (left panel), PLE spectra and relative quantum yield (QY) (right panel) for bandgap emission of exfoliated monolayer on (b) quartz and (c) hBN substrates.

5.11. Carrier relaxation pathway

5.11.1. Energy landscape

The photocarriers relax through a series of phonon scattering, and are subject to the selection rules imposed by energy and momentum conservation. In the approximation of weakly interacting electron and hole, the electron-phonon scattering time is given by the Fermi golden rule^{213, 214}

$$\tau^{-1} = \frac{2\pi}{\hbar} \sum_f \left| \langle \psi_i | \hat{V} | \psi_f \rangle \right|^2 \delta(\varepsilon_f - \varepsilon_i \mp \hbar\omega) \left(n_B(\hbar\omega, T) + \begin{cases} 1 \\ 0 \end{cases} \right), \quad (\text{Eq. 5.8})$$

where $|\psi_i\rangle$ and $|\psi_f\rangle$ are the initial and final states with momentum \mathbf{k}_i and $\mathbf{k}_f = \mathbf{k}_i - \mathbf{q}$ and energies ε_i and ε_f . \mathbf{q} is the scattering vector, \hat{V} is the interaction potential, and $n_B(\hbar\omega, T)$ is the Bose-Einstein distribution. The upper/lower elements correspond to phonon emission/absorption process.

Figure 5.14a shows the potential contour of the nesting region in the first Brillouin zone along with the potential map of the conduction and the valence bands. We have defined these regions using the criteria $|\nabla_k(E_c - E_v)| \ll 1 \text{ eV}/(2\pi/a)$,¹²⁵ where $2\pi/a$ is the modulus of the reciprocal lattice vector, E_c and E_v are the energy in the unoccupied states in the conduction band (c) and the occupied states in the valence band (v), respectively. This region is highlighted in white in Figure 5.14a. The arrows indicate the possible relaxation paths for electrons and holes after excitation in the nesting region. According to the DFT results, majority of the photocarriers are generated between Γ and Λ points. The electrons and holes are likely to relax into Λ and Γ points, respectively. Some photocarriers are also generated between Λ and K points, where weak nesting is observed. Since the nesting between Λ and K points is relatively close to the K point, most of the photocarrier relax to the K points, giving rise to direct exciton emission. Figure 5.14b shows the similar potential maps for bilayer MoS_2 . It

can be seen that the nesting region is extended around the Γ point for bilayer compared to the case of monolayer. Figure 5.15 shows calculated topology of the electron energy bands for monolayer WS_2 . Note that monolayer WS_2 exhibits energy landscape similar to that of monolayer MoS_2 .

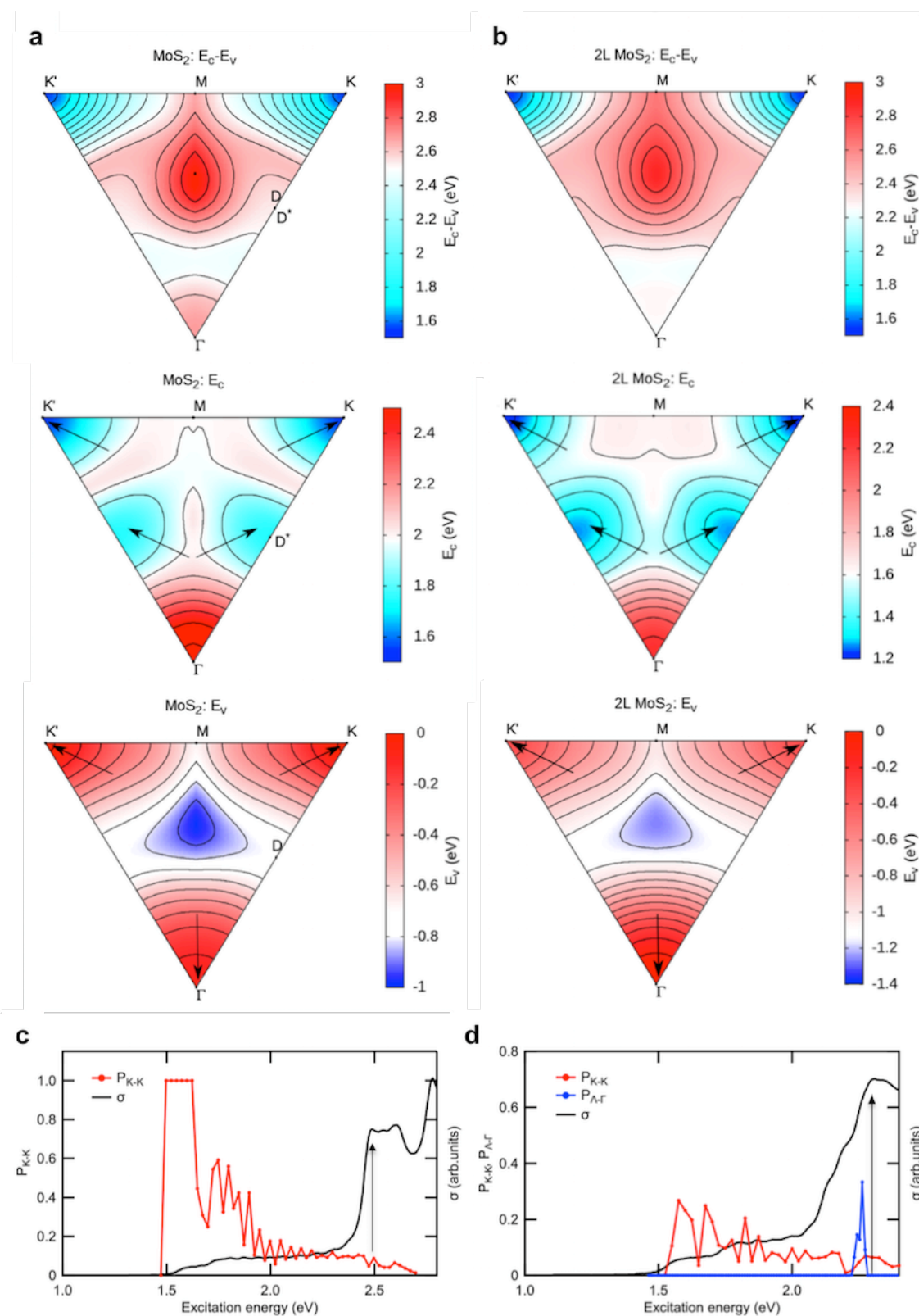


Figure 5.14 Calculated energy landscape and optical spectra for monolayer and bilayer MoS₂. (a, b) Energy map of $E_c - E_v$, E_c and E_v in the Brillouin zone for monolayer and

bilayer MoS₂. The arrows in E_c and E_v indicate possible relaxation pathways of carriers from the nesting region. (c, d) The fraction of electron-hole pairs that end the relaxation at the K point (P_{K-K} , red curve) and the optical conductivity (σ , black curve) for monolayer and bilayer MoS₂. For (d), the fraction of electron-hole pairs relaxing to Λ valley and Γ hill ($P_{\Lambda-\Gamma}$) is also shown (blue plot). The arrows in (c) and (d) indicate the position of the first peak due to band nesting.

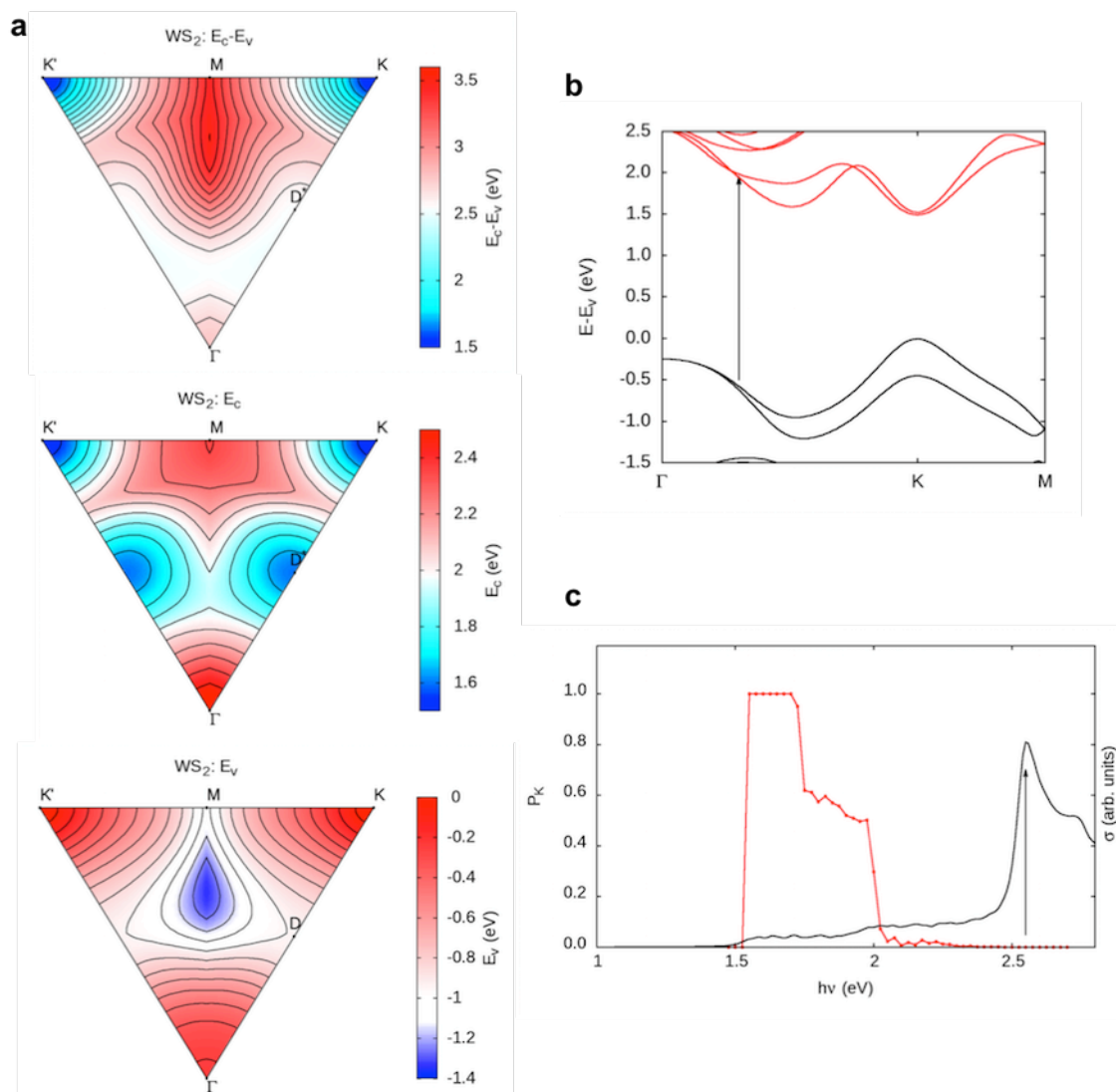


Figure 5.15 Calculated topology of the electron energy bands for monolayer WS₂. (a) Map on the Brillouin zone of E_c-E_v , E_c and E_v for monolayer WS₂. (b) The band

structure of monolayer WS₂. (c) The fraction of electron-hole pairs that end the relaxation at the K point (red curve, left axis) and the optical conductivity (black curve, right axis). The arrows in (d) and (e) signal the position of the first band-nesting peak.

It should be also noted that the Coulomb interaction between electron and hole is not considered in the calculated optical conductivity and the excitonic features are absent in the optical conductivity spectrum. However, our single-electron picture accounts for the presence of the absorption transitions corresponding to peaks A, B and C, and provides insight on the photocarrier relaxation, even though excitonic effects, e.g. the shift in the peak energies due to exciton binding, are not included in the model. This is supported by the work reported by Qiu *et al.*¹²⁹ They calculated the band structures of monolayer MoS₂ employing GW-Bethe-Salpeter equation, which takes into account excitonic effects. The region of the Brillouin Zone found to be responsible for peak ‘C’ agrees with our results. The main shortcoming of our approximation is the underestimation of the peak energy by about ~1 eV.

5.11.2. Monte-Carlo simulation of photocarrier relaxation

The Monte-Carlo simulations of the carrier relaxation paths were carried out using as input the topology of the two highest occupied bands and two lowest unoccupied bands calculated from first-principles (see Figure 5.14 and Figure 5.15), as described in Section 5.4. Excitonic effects were not taken into account. The phonon energies were obtained from Ref.²¹⁵. The phonon dispersion for the acoustic bands is considered to be approximately linear, whereas the optical phonon energy is considered to be independent on the phonon wavelength. The scattering probability is assumed to be the same for acoustic and optical phonons.²¹⁵ The relaxation is stopped when the carrier is within a capture radius R (taken to be $\sim 10^{-4} 2\pi/a$) of a minimum of E_c , maximum of E_v

or when there are no allowed phonon-emission transitions. The k-point grid interval was taken to be $0.01 \frac{2\pi}{a}$, where a is the lattice constant.

Figure 5.16 highlights the difference between the excitation with photons with an energy slightly above B, which in the calculations is located at about 1.7 eV for MoS₂, and an energy in the band-nesting region (close to the energy of the C peak). Firstly, it should be noticed that a larger area of the reciprocal space is excited in the second case (with energy 2.50 eV), for the same energy interval of 25 meV – thus the greatest optical conductivity. Photons with energy close to 1.90 eV produce electron-hole pairs in the vicinity of the K and K' points. Those electrons can only relax to the bottom of the conduction band of K point, and the respective electrons can relax to K/K' or Γ (where E_v , according to our calculation, is only about 80 meV below K), and therefore the subsequent intensity of the PL A transition is high. In contrast, for an excitation energy of 2.50 eV, a large fraction of the photo-excited electron-hole pairs is originally close to D or Γ than to K or K'. Thus, it is likely that a sizable fraction of the electron-hole pairs is dissociated and later recombines through the indirect transition D*- Γ .

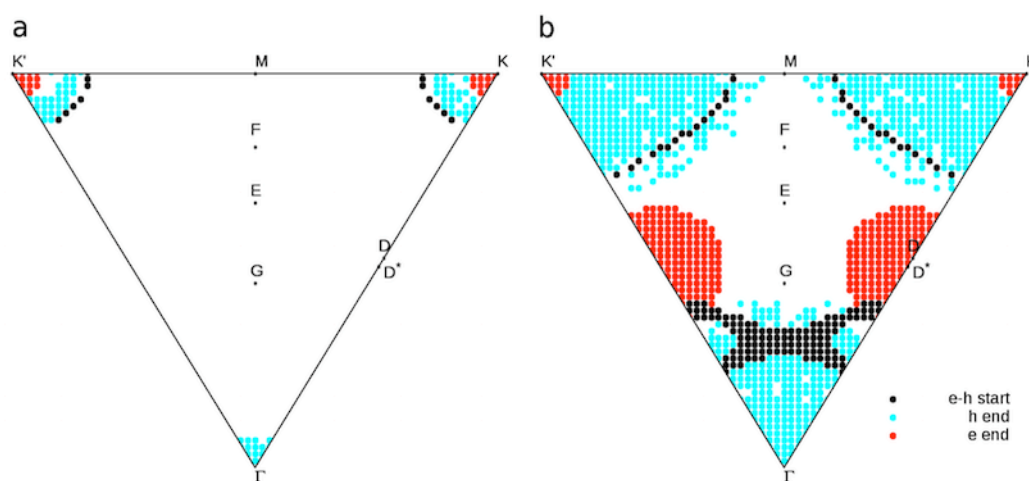


Figure 5.16 Calculated end points of the relaxation paths of photoexcited carriers for monolayer MoS₂, for excitation energies (a) 1.900 ± 0.025 eV and (b) 2.500 ± 0.025 eV.

The plot area represents 1/6th of the Brillouin zone. The K points where electron-hole pairs are generated for that particular excitation energy are marked in black (e-h start). The K points where the electrons and holes ended up after relaxation are shown in color.

We estimate the fraction of photocarriers reaching the conduction band minimum (CBM) and valence band maximum (VBM) at the K point after excitation at the nesting region for monolayer MoS₂. Both acoustic and optical/homopolar phonons can intervene in the carrier relaxation, the former mainly through deformation potential interaction, and the latter mainly through Fröhlich interaction. In MoS₂, the scattering rates have been calculated for both acoustic and optical phonons and were found to be comparable above the onset of optical phonon emission.²¹⁵ Further, both rates are approximately independent of q except for short wavelength acoustic phonons. Thus, we assume that all allowed phonon emission events are equally probable. The relaxation of the electron and hole were assumed to be independent and the process was stopped whenever the carrier was within a capture radius R (taken to be $\sim 10^{-4} 2\pi/a$) of a band extremum.

The fraction of electron-hole pairs that end the relaxation at the K point is shown as a function of the excitation energy in Figure 5.14c for monolayer MoS₂. Between the energies corresponding to peaks A and B, the probability of electron-hole pairs relaxing to K is unity. However, this fraction becomes considerably lower at ~ 2 eV. This trend reproduces well the decrease of the relative QY at the C peak (Figure 5.10a). From this energy onwards, the relaxation is mostly mediated by acoustic phonons. When the excitation energy is close to the C peak energy, a large fraction of the holes relax to the Γ point and electrons to the D* point (close to Λ). The energy of the first peak in the optical conductivity is due to nesting and is found at about 2.5 eV as indicated by the

arrow in Figure 5.14c. The population of relaxed carriers at the different stationary points of the Brillouin zone can be found in Figure 5.16.

For bilayers MoS₂, a similar trend is observed for the fraction of electron-hole pairs that reach the K point. The band nesting and corresponding divergence in the optical conductivity is observed at excitation energy of ~2.4 eV. At this energy, rapid increase in the population of electrons and holes that relax to the Λ valley and Γ hill is observed. This trend explains the experimentally observed increase in the indirect emission intensity at the C peak absorption in bilayer MoS₂ (Figure 5.11b).

5.12. Discussion on the relaxation pathways

We summarize in Figure 5.17 the possible relaxation pathways for monolayer and bilayer MX₂ when the excitation is in resonance with the band nesting energy corresponding to the C absorption band. The system is initially excited from the ground state (GS) to the band nesting excited state (BN). A large fraction of these excited states relaxes to another excited state (Λ/Γ), which represents the state where electrons occupy the Λ valley and holes are at the Γ hill. Radiative recombination from this state competes unfavorably with the non-radiative decay (k_{nr}^i), which is a fast process (2-4 ps),²⁰⁸ and intervalley scattering (k_{iv}) to the lowest excited state (K/K), where both electrons and holes occupy the K point. Thus, only a small fraction of the initial excited states are transferred to the K/K state, where radiative decay occurs with a moderate yield. In bilayer MX₂, a sizeable fraction of the initial excited states decay to the Λ/Γ state, where radiative indirect transition occurs with a modest yield. Note that this indirect emission does not compete with the intervalley scattering unlike the case of monolayer. Hot electron emission from the K/K state also occurs with non-negligible efficiency, partly due to intraband relaxation and intervalley scattering of hot carriers.

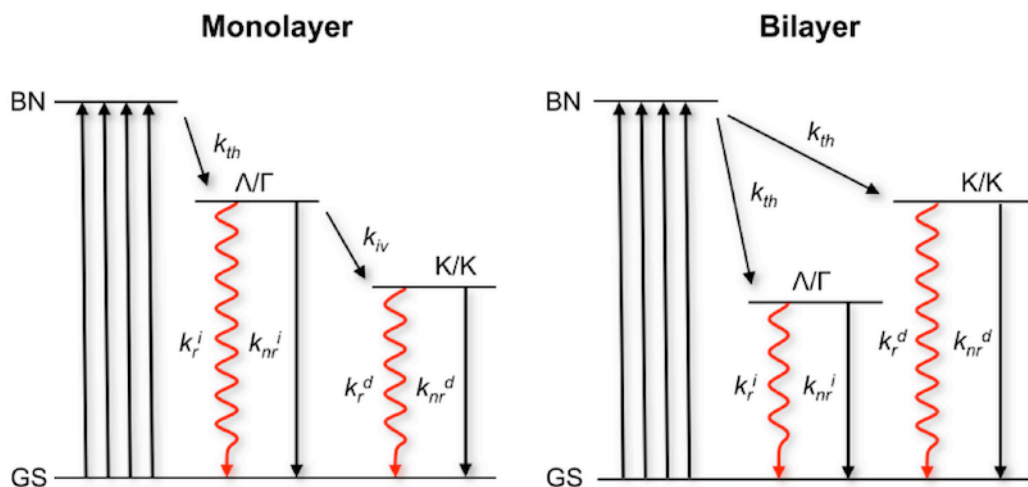


Figure 5.17 Excitation and relaxation pathways for photocarriers. Energy diagram representing photocarrier relaxation channels in monolayer and bilayer MX_2 , where the initial excitation is from the ground state (GS) to the band nesting (BN) energy. Nonradiative transition is indicated with a solid arrow. A rate constant k is associated with each transition. The subscripts indicate the types of transition: intravalley thermalization (th), intervalley scattering (iv), radiative (r) and nonradiative (nr). The superscripts (i) and (d) indicate indirect and direct transition, respectively.

The above qualitative model indicates that nonradiative decay rate k_{nr} plays a crucial role in the carrier relaxation channels and emission intensity. It is known that k_{nr} depends on the density of nonradiative decay centers, which may come from the trap states of the substrate, surface impurities, and intrinsic defects of the material.^{208, 211} We investigated the effects of nonradiative decay channels by arbitrarily reducing k_{nr} by using the hexagonal boron nitride as the substrate. We found that this leads not only to the overall enhancement in the PL intensity but also slight increase in the relative QY at the C absorption peak, supporting the validity of the above model (see Figure 5.13 and Section 5.10).

5.13. Effective collection of hot carriers

We have revealed the mechanisms of the giant light-matter interactions and photocarrier relaxation processes. This study shows which material is one of the most effective candidates ever to absorb light and convert it into electricity. The efficient hot carrier generation makes TMDs attractive. Utilizing photogenerated hot carriers leads to produce higher photovoltages or larger photocurrents, which translates into the efficient photoelectric conversion.^{216, 217} The results suggest that decreasing the non-radiative decay rate leads more efficient generation of hot carriers, which can be a guideline towards implementation of TMDs to the optoelectronic devices. According to the suggestion, the semiconducting 2D TMDs can be a prototype for ultra-sensitive photodetector and high performance flexible solar cells.

5.14. Chapter summary

We have examined the generation and relaxation processes of photoexcited carriers in mono- and bilayer MX_2 using PLE spectroscopy and *ab initio* DFT calculation. We show that the relaxation channel of the photoexcited carriers is strongly dependent on the excitation energy. The strong absorption at C peak corresponds to the optical transition around the region of the Brillouin zone where the valence and conduction bands are nested. The PLE intensity at the C absorption peak is suppressed or only weakly enhanced. The relative QY drops consistently for excitation energies above the B peak resonance. We attribute this behavior to the spontaneous separation of electron-hole pairs in the momentum space due to the band nesting. The band nesting also plays a crucial role of temporary suppression of their relaxation to the fundamental band edge, generating hot carriers efficiently. Our experimental results show an excellent agreement with the Monte-Carlo simulations of carrier relaxation. The findings provide insight into the unique dynamics of photocarrier relaxation pathways

and motivate studies on the hot electron behaviors in 2D materials and their potential for efficient hot carrier collection devices.

Chapter 6. Conclusions and outlook

6.1. Summary

In this thesis, the unique behavior of photocarrier in graphene oxide (GO) and transition metal dichalcogenides (TMDs) has been revealed. We have shown that GO and TMDs exhibit characteristic photocarrier generation and relaxation associated their electronic structures. We have revealed the attractive optical properties that evolve in from inhomogeneous atomic and electronic structures for GO and from the band nesting of the energy band structures for TMDs. These atomically thin 2D materials exhibit characteristic optical properties depending on the size of the optically active domains as summarized in Figure 6.1. The small sp^2 fragments of GO exhibit the quasi-molecular luminescence. With increasing the size of the sp^2 domains, GO becomes more like the semiconducting nano-structures and exhibits the excitonic luminescence from the GND states in GO. The 2D TMDs show the behavior of the semiconducting properties with the photocarrier generation and relaxation dictated by the characteristic energy band structures.

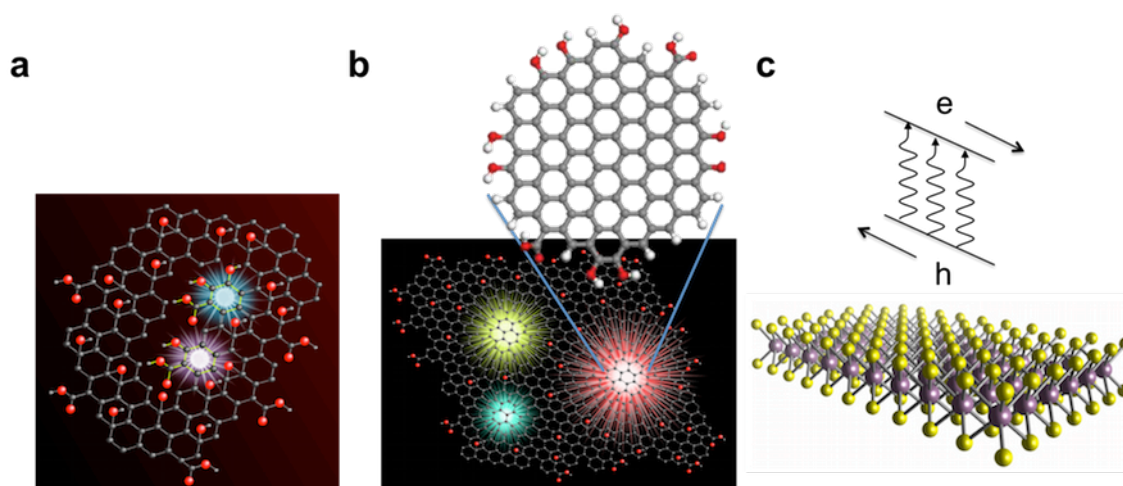


Figure 6.1 Summary of the characteristic optical properties of the atomically thin 2D materials studied in this thesis. (a) The quasi-molecular luminescence of GO, (b) the excitonic luminescence from the nanodisc states embedded in the sp^3 matrix of GO, and (c) 2D TMDs with the photocarrier relaxation along the nesting region of the electronic band structures.

The results based on static photoluminescence (PL) excitation spectroscopy, time-resolved PL spectroscopy, and first principle calculations have revealed the behavior of photoexcited carriers in GO and TMDs. We have shown the model of the luminescent mechanisms of GO to comprehensively understand the previously suggested models.^{39, 80, 141} The behavior of photocarriers in GO is found to be determined by a zero-dimensional property within graphene nanodisc (GND) states. Smaller GND states that consist of a few aromatic rings behave like isolated molecules (or quasi-molecular states), while larger GND states with a diameter of sub-nanometer to a few nanometer behave like quantum dots with many body effects among carriers. In the larger GND states, a characteristic photocarrier dynamics has been revealed. Energy transfers among the GND states is found to be the major relaxation process and can cause decrease the luminescent efficiency.

On the other hand, the behavior of photocarriers in TMDs is found to be determined by a two-dimensional property related with the energy band structure. Light absorption is enhanced in particular energy range because of the characteristic band structure called “band nesting”. We have unraveled the photocarrier relaxation pathways, which is generated by a higher energy excitation corresponding to the band nesting. The photoexcited electron-hole pairs in the nesting region spontaneously separate in momentum space, relaxing towards immediate band extrema with opposite momentum. We have also found the efficient hot carrier generation accompanied with the higher energy excitation in the nesting. The understanding of the characteristic photocarrier generation and relaxation mechanisms provides insight into the implementation of GO to tunable light-emitting devices and TMDs to efficient light-harvesting devices as well as progress of understanding fundamental optical properties of the atomically thin two-dimensional semiconductors.

We have demonstrated how photocarriers are generated and relaxed in the atomically thin 2D sheets of GO and TMDs. However, significant challenges still remain to implement them on light-harvesting and -emitting devices. Suggested future work will be presented in the following Section.

6.2. Future outlook

Towards the implementation of optoelectronic devices, the solution processability^{64, 72, 73, 77} of GO and TMDs is promising to integrate them on flexible substrates. Furthermore, the GO and TMDs cover the wide luminescent range in NIR-UV region and also exhibit good carrier-transporting properties compared to other counterpart organic materials, which make the materials useful as the light-emitting devices. In spite of the promising optoelectronic properties, the most significant challenge would lie on

improvement of PL QY for the 2D atomic sheets. Zhang and co-workers have reported that QY of GO is as high as 12.8% for blue PL.²¹⁸ This feature suggests that luminescence from GO could be promising for application to light emitting diodes. At the same time, there is still room for enhancing the luminescence based on our study. In Section 4.6, we described the dynamics that photocarrier relaxes through energy transfer from higher to lower potential nanodisc states. Photocarrier can finally relax to larger graphitic region with a zero gap, leading to quenching PL. This energy transfer can cause a decrease of QY. The suppression of the quenching process improves the light-emitting properties.

To improve the QY, it can be helpful to use chemical modification of the larger graphitic region to increase a portion of sp^2 carbon clusters that is able to emit light. Recently, Hersam and co-workers have developed that oxidation of graphene in atomic-precision by scanning tunneling microscopic technique.¹⁷⁷ This technique has a potential for preparing GO that can exhibit highly efficient luminescence, while this is limited scalability. It is expected that selective chemical modification for the graphitic region in a large scale will be developed for realizing GO-based optoelectronics. The same thing is true of TMDs. The measured QY of MoS_2 is so far up to 0.4% for monolayers.^{46, 50} One of the reasons could be an intrinsic doping and defects in MoS_2 which cause the low QY.^{54, 62, 140, 219} These doping and defects form trap states with non-radiative character. The quenching mechanisms of PL are expected to be further explored, although improvement of QY has been also observed in the suspended samples⁵⁰ and samples on hBN⁵¹ in contrast to on SiO_2 substrates. We have shown that hBN decrease the non-radiative decay rate in Section 5.10. Further clarifications of the quenching mechanisms and increasing the QY open the future for optoelectronics applications.

From the viewpoint of the light-absorbing materials, TMDs can be favorable materials for light-harvesting devices such as a photodetector and solar cell because of high photoresponsivity^{18, 220} and the giant light absorption that we have described in Chapter 5. We have also emphasized their promising potential of efficient hot carrier collection with the optical excitation in the nesting. The next challenge would be efficient extraction of the hot carriers in TMDs. Detailed time-resolved measurements using pump-probe technique is likely to be helpful to qualitatively understand the band nesting effect. To boost the light-matter interaction, it is also promising to take advantage of plasmonic enhancement of light absorption in the 2D atomic sheets with noble metal nano particles.^{66, 221} Further photocurrent measurement will provide an insight into the challenge associated with band nesting effect of TMDs. Overcoming the challenges accelerate realization of ultra-sensitive photodetector and high performance flexible solar cells based on the TMDs.

Bibliography

1. Van Noorden, R. *Nature* **2006**, 442, (7100), 228-229.
2. Mak, K. F.; Shan, J.; Heinz, T. F. *Phys. Rev. Lett.* **2011**, 106, (4), 046401.
3. Berger, C.; Song, Z.; Li, X.; Wu, X.; Brown, N.; Naud, C.; Mayou, D.; Li, T.; Hass, J.; Marchenkov, A. N. *Science* **2006**, 312, (5777), 1191-1196.
4. Pu, J.; Yomogida, Y.; Liu, K.-K.; Li, L.-J.; Iwasa, Y.; Takenobu, T. *Nano Lett.* **2012**, 12, (8), 4013-4017.
5. Novoselov, K. S.; Geim, A. K.; Morozov, S. V.; Jiang, D.; Zhang, Y.; Dubonos, S. V.; Grigorieva, I. V.; Firsov, A. A. *Science* **2004**, 306, (5696), 666-669.
6. Novoselov, K. S.; Jiang, D.; Schedin, F.; Booth, T. J.; Khotkevich, V. V.; Morozov, S. V.; Geim, A. K. *Proc. Natl. Acad. Sci. U. S. A.* **2005**, 102, (30), 10451-10453.
7. Eda, G.; Fanchini, G.; Chhowalla, M. *Nat. Nanotechnol.* **2008**, 3, (5), 270-274.
8. Kroto, H. W.; Heath, J. R.; O'Brien, S. C.; Curl, R. F.; Smalley, R. E. C. *Nature* **1985**, 318, 162-163.
9. Iijima, S. *Nature* **1991**, 354, (7), 56-58.
10. Stankovich, S.; Dikin, D. A.; Piner, R. D.; Kohlhaas, K. A.; Kleinhammes, A.; Jia, Y.; Wu, Y.; Nguyen, S. T.; Ruoff, R. S. *Carbon* **2007**, 45, (7), 1558-1565.
11. Vogt, P.; De Padova, P.; Quaresima, C.; Avila, J.; Frantzeskakis, E.; Asensio, M. C.; Resta, A.; Ealet, B.; Le Lay, G. *Phys. Rev. Lett.* **2012**, 108, (15), 155501.
12. Lee, G.-H.; Yu, Y.-J.; Lee, C.; Dean, C.; Shepard, K. L.; Kim, P.; Hone, J. *Appl. Phys. Lett.* **2011**, 99, (24), 243114.
13. Qiao, J.; Kong, X.; Hu, Z.-X.; Yang, F.; Ji, W. *Nat. Commun.* **2014**, 5, 4475.
14. Chhowalla, M.; Shin, H. S.; Eda, G.; Li, L. J.; Loh, K. P.; Zhang, H. *Nat.*

Chem. **2013**, 5, (4), 263-275.

15. Radisavljevic, B.; Radenovic, A.; Brivio, J.; Giacometti, V.; Kis, A. *Nat. Nanotechnol.* **2011**, 6, (3), 147-150.
16. Bolotin, K. I.; Sikes, K. J.; Jiang, Z.; Klima, M.; Fudenberg, G.; Hone, J.; Kim, P.; Stormer, H. L. *Solid State Commun.* **2008**, 146, (9-10), 351-355.
17. Song, J. C.; Rudner, M. S.; Marcus, C. M.; Levitov, L. S. *Nano Lett.* **2011**, 11, (11), 4688-4692.
18. Lopez-Sanchez, O.; Lembke, D.; Kayci, M.; Radenovic, A.; Kis, A. *Nat. Nanotechnol.* **2013**, 8, (7), 497-501.
19. Xia, F.; Mueller, T.; Lin, Y. M.; Valdes-Garcia, A.; Avouris, P. *Nat. Nanotechnol.* **2009**, 4, (12), 839-843.
20. Lee, C.; Wei, X.; Kysar, J. W.; Hone, J. *Science* **2008**, 321, (5887), 385-388.
21. Miller, J. R.; Outlaw, R. A.; Holloway, B. C. *Science* **2010**, 329, (5999), 1637-1639.
22. El-Kady, M. F.; Strong, V.; Dubin, S.; Kaner, R. B. *Science* **2012**, 335, (6074), 1326-1330.
23. Voiry, D.; Yamaguchi, H.; Li, J.; Silva, R.; Alves, D. C.; Fujita, T.; Chen, M.; Asefa, T.; Shenoy, V. B.; Eda, G. *Nat. Mater.* **2013**, 12, (9), 850-855.
24. Geim, A. K.; Novoselov, K. S. *Nat. Mater.* **2007**, 6, (3), 183-191.
25. Zhang, Y.; Tan, Y.-W.; Stormer, H. L.; Kim, P. *Nature* **2005**, 438, (7065), 201-204.
26. Stankovich, S.; Dikin, D. A.; Dommett, G. H.; Kohlhaas, K. M.; Zimney, E. J.; Stach, E. A.; Piner, R. D.; Nguyen, S. T.; Ruoff, R. S. *Nature* **2006**, 442, (7100), 282-286.
27. Kopelevich, Y.; Esquinazi, P. *Adv. Mater.* **2007**, 19, (24), 4559-4563.
28. Dikin, D. A.; Stankovich, S.; Zimney, E. J.; Piner, R. D.; Dommett, G. H.; Evmenenko, G.; Nguyen, S. T.; Ruoff, R. S. *Nature* **2007**, 448, (7152), 457-460.

29. Loh, K. P.; Bao, Q.; Eda, G.; Chhowalla, M. *Nat. Chem.* **2010**, *2*, (12), 1015-1024.
30. Yu, K.; Wang, P.; Lu, G.; Chen, K.-H.; Bo, Z.; Chen, J. *J. Phys. Chem. Lett.* **2011**, *2*, (6), 537-542.
31. Bonaccorso, F.; Sun, Z.; Hasan, T.; Ferrari, A. *Nat. Photonics* **2010**, *4*, (9), 611-622.
32. Eda, G.; Mattevi, C.; Yamaguchi, H.; Kim, H.; Chhowalla, M. *J. Phys. Chem. C* **2009**, *113*, (35), 15768-15771.
33. Yang, D.; Velamakanni, A.; Bozoklu, G.; Park, S.; Stoller, M.; Piner, R. D.; Stankovich, S.; Jung, I.; Field, D. A.; Ventrice Jr, C. A. *Carbon* **2009**, *47*, (1), 145-152.
34. Zhang, Y.; Tang, T.-T.; Girit, C.; Hao, Z.; Martin, M. C.; Zettl, A.; Crommie, M. F.; Shen, Y. R.; Wang, F. *Nature* **2009**, *459*, (7248), 820-823.
35. Robertson, J.; O'reilly, E. *Phys. Rev. B* **1987**, *35*, (6), 2946.
36. Chen, C.; Robertson, J. *J. Non-Cryst. Solids* **1998**, *227*, 602-606.
37. Mathioudakis, C.; Kopidakis, G.; Kelires, P.; Patsalas, P.; Gioti, M.; Logothetidis, S. *Thin Solid Films* **2005**, *482*, (1), 151-155.
38. Erickson, K.; Erni, R.; Lee, Z.; Alem, N.; Gannett, W.; Zettl, A. *Adv. Mater.* **2010**, *22*, (40), 4467-4472.
39. Eda, G.; Lin, Y. Y.; Mattevi, C.; Yamaguchi, H.; Chen, H. A.; Chen, I. S.; Chen, C. W.; Chhowalla, M. *Adv. Mater.* **2010**, *22*, (4), 505-509.
40. Sun, X.; Liu, Z.; Welsher, K.; Robinson, J. T.; Goodwin, A.; Zaric, S.; Dai, H. *Nano Res.* **2008**, *1*, (3), 203-212.
41. Luo, Z.; Vora, P. M.; Mele, E. J.; Johnson, A. T. C.; Kikkawa, J. M. *Appl. Phys. Lett.* **2009**, *94*, (11), 111909.
42. Liu, Z.-B.; Zhao, X.; Zhang, X.-L.; Yan, X.-Q.; Wu, Y.-P.; Chen, Y.-S.; Tian, J.-G. *J. Phys. Chem. Lett.* **2011**, *2*, (16), 1972-1977.
43. Exarhos, A. L.; Turk, M. E.; Kikkawa, J. M. *Nano Lett.* **2013**, *13*, (2),

344-349.

44. Liu, Z.; Robinson, J. T.; Sun, X.; Dai, H. *J. Am. Chem. Soc.* **2008**, 130, (33), 10876-10877.
45. Wilson, J.; Yoffe, A. *Adv. Phys.* **1969**, 18, (73), 193-335.
46. Wang, Q. H.; Kalantar-Zadeh, K.; Kis, A.; Coleman, J. N.; Strano, M. S. *Nat. Nanotechnol.* **2012**, 7, (11), 699-712.
47. Li, X.; Zhang, F.; Niu, Q. *Phys. Rev. Lett.* **2013**, 110, (6), 066803.
48. Eda, G.; Fujita, T.; Yamaguchi, H.; Voiry, D.; Chen, M.; Chhowalla, M. *ACS nano* **2012**, 6, (8), 7311-7317.
49. Splendiani, A.; Sun, L.; Zhang, Y.; Li, T.; Kim, J.; Chim, C. Y.; Galli, G.; Wang, F. *Nano Lett.* **2010**, 10, (4), 1271-1275.
50. Mak, K. F.; Lee, C.; Hone, J.; Shan, J.; Heinz, T. F. *Phys. Rev. Lett.* **2010**, 105, (13), 136805.
51. Mak, K. F.; He, K.; Shan, J.; Heinz, T. F. *Nat. Nanotechnol.* **2012**, 7, (8), 494-498.
52. Xiao, D.; Liu, G.-B.; Feng, W.; Xu, X.; Yao, W. *Phys. Rev. Lett.* **2012**, 108, (19), 196802.
53. Cao, T.; Wang, G.; Han, W.; Ye, H.; Zhu, C.; Shi, J.; Niu, Q.; Tan, P.; Wang, E.; Liu, B.; Feng, J. *Nat. Commun.* **2012**, 3, 887.
54. Mak, K. F.; He, K.; Lee, C.; Lee, G. H.; Hone, J.; Heinz, T. F.; Shan, J. *Nat. Mater.* **2013**, 12, (3), 207-211.
55. Ross, J. S.; Wu, S.; Yu, H.; Ghimire, N. J.; Jones, A. M.; Aivazian, G.; Yan, J.; Mandrus, D. G.; Xiao, D.; Yao, W.; Xu, X. *Nat. Commun.* **2013**, 4, 1474.
56. Kumar, N.; Najmaei, S.; Cui, Q.; Ceballos, F.; Ajayan, P.; Lou, J.; Zhao, H. *Phys. Rev. B* **2013**, 87, (16), 161403.
57. Zeng, H.; Liu, G. B.; Dai, J.; Yan, Y.; Zhu, B.; He, R.; Xie, L.; Xu, S.; Chen, X.; Yao, W.; Cui, X. *Sci. Rep.* **2013**, 3, 1608.

58. He, K.; Poole, C.; Mak, K. F.; Shan, J. *Nano Lett.* **2013**, 13, (6), 2931-2936.
59. Feng, J.; Qian, X.; Huang, C.-W.; Li, J. *Nat. Photonics* **2012**, 6, (12), 866-872.
60. Mouri, S.; Miyauchi, Y.; Matsuda, K. *Nano Lett.* **2013**, 13, (12), 5944-5948.
61. Tongay, S.; Suh, J.; Ataca, C.; Fan, W.; Luce, A.; Kang, J. S.; Liu, J.; Ko, C.; Raghunathan, R.; Zhou, J.; Ogletree, F.; Li, J.; Grossman, J. C.; Wu, J. *Sci. Rep.* **2013**, 3, 2657.
62. Tongay, S.; Zhou, J.; Ataca, C.; Liu, J.; Kang, J. S.; Matthews, T. S.; You, L.; Li, J.; Grossman, J. C.; Wu, J. *Nano Lett.* **2013**, 13, (6), 2831-2836.
63. Lee, Y. H.; Zhang, X. Q.; Zhang, W.; Chang, M. T.; Lin, C. T.; Chang, K. D.; Yu, Y. C.; Wang, J. T.; Chang, C. S.; Li, L. J.; Lin, T. W. *Adv. Mater.* **2012**, 24, (17), 2320-2325.
64. Eda, G.; Yamaguchi, H.; Voiry, D.; Fujita, T.; Chen, M.; Chhowalla, M. *Nano Lett.* **2011**, 11, (12), 5111-5116.
65. Britnell, L.; Ribeiro, R. M.; Eckmann, A.; Jalil, R.; Belle, B. D.; Mishchenko, A.; Kim, Y. J.; Gorbachev, R. V.; Georgiou, T.; Morozov, S. V.; Grigorenko, A. N.; Geim, A. K.; Casiraghi, C.; Castro Neto, A. H.; Novoselov, K. S. *Science* **2013**, 340, (6138), 1311-1314.
66. Eda, G.; Maier, S. A. *ACS nano* **2013**, 7, (7), 5660-5665.
67. Cherenack, K.; van Pieterson, L. *J. Appl. Phys.* **2012**, 112, (9), 091301.
68. Kaltenbrunner, M.; Sekitani, T.; Reeder, J.; Yokota, T.; Kuribara, K.; Tokuhara, T.; Drack, M.; Schwodiauer, R.; Graz, I.; Bauer-Gogonea, S.; Bauer, S.; Someya, T. *Nature* **2013**, 499, (7459), 458-463.
69. Gustafsson, G.; Cao, Y.; Treacy, G.; Klavetter, F.; Colaneri, N.; Heeger, A. *Nature* **1992**, 357, (6378), 477-479.
70. Krebs, F. C.; Gevorgyan, S. A.; Alstrup, J. *J. Mater. Chem.* **2009**, 19, (30), 5442-5451.

71. Forrest, S. R. *Nature* **2004**, 428, (6986), 911-918.
72. Li, S.-S.; Tu, K.-H.; Lin, C.-C.; Chen, C.-W.; Chhowalla, M. *ACS nano* **2010**, 4, (6), 3169-3174.
73. Yun, J. M.; Yeo, J. S.; Kim, J.; Jeong, H. G.; Kim, D. Y.; Noh, Y. J.; Kim, S. S.; Ku, B. C.; Na, S. I. *Adv. Mater.* **2011**, 23, (42), 4923-4928.
74. Bernardi, M.; Palumbo, M.; Grossman, J. C. *Nano Lett.* **2013**, 13, (8), 3664-3670.
75. Mak, K. F.; Sfeir, M. Y.; Wu, Y.; Lui, C. H.; Misewich, J. A.; Heinz, T. F. *Phys. Rev. Lett.* **2008**, 101, (19), 196405.
76. Nair, R. R.; Blake, P.; Grigorenko, A. N.; Novoselov, K. S.; Booth, T. J.; Stauber, T.; Peres, N. M. R.; Geim, A. K. *Science* **2008**, 320, (5881), 1308.
77. Eda, G.; Chhowalla, M. *Adv. Mater.* **2010**, 22, (22), 2392-2415.
78. Jung, I.; Dikin, D. A.; Piner, R. D.; Ruoff, R. S. *Nano Lett.* **2008**, 8, (12), 4283-4287.
79. Lee, D.; Seo, J.; Zhu, X.; Lee, J.; Shin, H. J.; Cole, J. M.; Shin, T.; Lee, J.; Lee, H.; Su, H. *Sci. Rep.* **2013**, 3, 2250.
80. Chien, C. T.; Li, S. S.; Lai, W. J.; Yeh, Y. C.; Chen, H. A.; Chen, I. S.; Chen, L. C.; Chen, K. H.; Nemoto, T.; Isoda, S.; Chen, M.; Fujita, T.; Eda, G.; Yamaguchi, H.; Chhowalla, M.; Chen, C. W. *Angew. Chem., Int. Ed. Engl.* **2012**, 51, (27), 6662-6666.
81. Fox, M., *Optical properties of solids*. OUP Oxford: 2010.
82. Dekker, C. *Physics today* **1999**, 52, 22-30.
83. Arakawa, Y. *Appl. Phys. Lett.* **1982**, 40, (11), 939-941.
84. Ohta, T.; Bostwick, A.; Seyller, T.; Horn, K.; Rotenberg, E. *Science* **2006**, 313, (5789), 951-954.
85. Castro, E. V.; Novoselov, K. S.; Morozov, S. V.; Peres, N. M. R.; Lopes dos Santos, J. M. B.; Nilsson, J.; Guinea, F.; Geim, A. K.; Castro Neto, A. H. *Phys. Rev.*

Lett. **2007**, 99, (21), 216802.

86. Lui, C. H.; Li, Z.; Mak, K. F.; Cappelluti, E.; Heinz, T. F. *Nat. Physics* **2011**, 7, (12), 944-947.

87. Brodie, B. C. *Phil. Trans. Roy. Soc.* **1859**, 149, 249-259.

88. Worsley, K. A.; Ramesh, P.; Mandal, S. K.; Niyogi, S.; Itkis, M. E.; Haddon, R. C. *Chem. Phys. Lett.* **2007**, 445, (1-3), 51-56.

89. Widenkvist, E.; Boukhvalov, D.; Rubino, S.; Akhtar, S.; Lu, J.; Quinlan, R.; Katsnelson, M. I.; Leifer, K.; Grennberg, H.; Jansson, U. *J. Phys. D: Appl. Phys.* **2009**, 42, (11), 112003.

90. Luo, Z.; Lu, Y.; Somers, L. A.; Johnson, A. C. *J. Am. Chem. Soc.* **2009**, 131, (3), 898-899.

91. Hummers Jr, W. S.; Offeman, R. E. *J. Am. Chem. Soc.* **1958**, 80, (6), 1339-1339.

92. Bagri, A.; Mattevi, C.; Acik, M.; Chabal, Y. J.; Chhowalla, M.; Shenoy, V. B. *Nat. Chem.* **2010**, 2, (7), 581-587.

93. He, H.; Klinowski, J.; Forster, M.; Lerf, A. *Chem. Phys. Lett.* **1998**, 287, (1), 53-56.

94. Gomez-Navarro, C.; Meyer, J. C.; Sundaram, R. S.; Chuvilin, A.; Kurasch, S.; Burghard, M.; Kern, K.; Kaiser, U. *Nano Lett.* **2010**, 10, (4), 1144-1148.

95. Lerf, A.; He, H.; Forster, M.; Klinowski, J. *J. Phys. Chem. B* **1998**, 102, (23), 4477-4482.

96. Wilson, J. A.; Di Salvo, F.; Mahajan, S. *Adv. Phys.* **1975**, 24, (2), 117-201.

97. Suzuki, R.; Sakano, M.; Zhang, Y. J.; Akashi, R.; Morikawa, D.; Harasawa, A.; Yaji, K.; Kuroda, K.; Miyamoto, K.; Okuda, T.; Ishizaka, K.; Arita, R.; Iwasa, Y. *Nat. Nanotechnol.* **2014**, 9, (8), 611-7.

98. Title, R. S.; Shafer, M. W. *Phys. Rev. B* **1973**, 8, (2), 615-620.

99. Ataca, C.; Topsakal, M.; Aktürk, E.; Ciraci, S. *J. Phys. Chem. C* **2011**, 115,

(33), 16354-16361.

100. Jorio, A.; Dresselhaus, M. S.; Saito, R.; Dresselhaus, G., *Raman spectroscopy in graphene related systems*. John Wiley & Sons: 2010.
101. Saito, R.; Dresselhaus, G.; Dresselhaus, M. *Phys. Rev. B* **2000**, 61, (4), 2981-2990.
102. Novoselov, K.; Geim, A. K.; Morozov, S.; Jiang, D.; Grigorieva, M. K. I.; Dubonos, S.; Firsov, A. *Nature* **2005**, 438, (7065), 197-200.
103. Castro Neto, A. H.; Peres, N. M. R.; Novoselov, K. S.; Geim, A. K. *Rev. Mod. Phys.* **2009**, 81, (1), 109-162.
104. Mattheiss, L. *Phys. Rev. B* **1973**, 8, (8), 3719-3740.
105. Kang, J.; Tongay, S.; Zhou, J.; Li, J.; Wu, J. *Appl. Phys. Lett.* **2013**, 102, (1), 012111.
106. Shi, H.; Pan, H.; Zhang, Y.-W.; Yakobson, B. *Phys. Rev. B* **2013**, 87, (15), 155304.
107. Kobayashi, K.; Yamauchi, J. *Phys. Rev. B* **1995**, 51, (23), 17085-17095.
108. Li, T.; Galli, G. *J. Phys. Chem. C* **2007**, 111, (44), 16192-16196.
109. Kuc, A.; Zibouche, N.; Heine, T. *Phys. Rev. B* **2011**, 83, (24), 245213.
110. Zhu, Z. Y.; Cheng, Y. C.; Schwingenschlögl, U. *Phys. Rev. B* **2011**, 84, (15), 153402.
111. Koroteev, Y.; Bihlmayer, G.; Gayone, J.; Chulkov, E.; Blügel, S.; Echenique, P.; Hofmann, P. *Phys. Rev. Lett.* **2004**, 93, (4), 046403.
112. LaShell, S.; McDougall, B. A.; Jensen, E. *Phys. Rev. Lett.* **1996**, 77, (16), 3419-3422.
113. Yang, H.; Feng, X.; Wang, Q.; Huang, H.; Chen, W.; Wee, A. T.; Ji, W. *Nano Lett.* **2011**, 11, (7), 2622-2627.
114. Zhu, L.; Kim, C.; Yoshita, M.; Chen, S.; Sato, S.; Mochizuki, T.; Akiyama, H.; Kanemitsu, Y. *Appl. Phys. Lett.* **2014**, 104, (3), 031118.

115. Chernikov, A.; Berkelbach, T. C.; Hill, H. M.; Rigosi, A.; Li, Y.; Aslan, O. B.; Reichman, D. R.; Hybertsen, M. S.; Heinz, T. F. *Phys. Rev. Lett.* **2014**, 113, (7), 076802.
116. Ando, T.; Zheng, Y.; Suzuura, H. *J. Phys. Soc. Jpn.* **2002**, 71, (5), 1318-1324.
117. Gusynin, V.; Sharapov, S.; Carbotte, J. *Phys. Rev. Lett.* **2006**, 96, (25), 256802.
118. Peres, N.; Guinea, F.; Castro Neto, A. *Phys. Rev. B* **2006**, 73, (12).
119. Liu, C. H.; Chang, Y. C.; Norris, T. B.; Zhong, Z. *Nat. Nanotechnol.* **2014**, 9, (4), 273-278.
120. Kim, C. O.; Kim, S.; Shin, D. H.; Kang, S. S.; Kim, J. M.; Jang, C. W.; Joo, S. S.; Lee, J. S.; Kim, J. H.; Choi, S. H.; Hwang, E. *Nat. Commun.* **2014**, 5, 3249.
121. Essig, S.; Marquardt, C. W.; Vijayaraghavan, A.; Ganzhorn, M.; Dehm, S.; Hennrich, F.; Ou, F.; Green, A. A.; Sciascia, C.; Bonaccorso, F.; Bohnen, K. P.; Lohneysen, H.; Kappes, M. M.; Ajayan, P. M.; Hersam, M. C.; Ferrari, A. C.; Krupke, R. *Nano Lett.* **2010**, 10, (5), 1589-1594.
122. Koyama, T.; Ito, Y.; Yoshida, K.; Tsuji, M.; Ago, H.; Kishida, H.; Nakamura, A. *ACS nano* **2013**, 7, (3), 2335-2343.
123. Fan, F.-R. F.; Park, S.; Zhu, Y.; Ruoff, R. S.; Bard, A. J. *J. Am. Chem. Soc.* **2008**, 131, (3), 937-939.
124. Shang, J.; Ma, L.; Li, J.; Ai, W.; Yu, T.; Gurzadyan, G. G. *Sci. Rep.* **2012**, 2, 792.
125. Carvalho, A.; Ribeiro, R. M.; Castro Neto, A. H. *Phys. Rev. B* **2013**, 88, (11), 115205.
126. Ramasubramaniam, A. *Phys. Rev. B* **2012**, 86, (11).
127. Cheiwchanchamnangij, T.; Lambrecht, W. R. L. *Phys. Rev. B* **2012**, 85, (20).
128. Komsa, H.-P.; Krasheninnikov, A. V. *Phys. Rev. B* **2012**, 86, (24), 241201.
129. Qiu, D. Y.; da Jornada, F. H.; Louie, S. G. *Phys. Rev. Lett.* **2013**, 111, (21),

216805.

130. Xia, F.; Farmer, D. B.; Lin, Y. M.; Avouris, P. *Nano Lett.* **2010**, 10, (2), 715-718.

131. Sze, S. M.; Ng, K. K., *Physics of Semiconductor Devices*. third ed.; Wiley: 2006.

132. Elias, D. C.; Gorbachev, R. V.; Mayorov, A. S.; Morozov, S. V.; Zhukov, A. A.; Blake, P.; Ponomarenko, L. A.; Grigorieva, I. V.; Novoselov, K. S.; Guinea, F.; Geim, A. K. *Nat. Physics* **2011**, 7, (9), 701-704.

133. Gómez-Navarro, C.; Weitz, R. T.; Bittner, A. M.; Scolari, M.; Mews, A.; Burghard, M.; Kern, K. *Nano Lett.* **2007**, 7, (11), 3499-3503.

134. Wang, S.; Ang, P. K.; Wang, Z.; Tang, A. L.; Thong, J. T.; Loh, K. P. *Nano Lett.* **2010**, 10, (1), 92-98.

135. Mattevi, C.; Eda, G.; Agnoli, S.; Miller, S.; Mkhoyan, K. A.; Celik, O.; Mastrogiovanni, D.; Granozzi, G.; Garfunkel, E.; Chhowalla, M. *Adv. Funct. Mater.* **2009**, 19, (16), 2577-2583.

136. Kaiser, A. B.; Gómez-Navarro, C.; Sundaram, R. S.; Burghard, M.; Kern, K. *Nano Lett.* **2009**, 9, (5), 1787-1792.

137. Grisdale, R. O. *J. Appl. Phys.* **1953**, 24, (10), 1288-1296.

138. Pike, G.; Seager, C. *Phys. Rev. B* **1974**, 10, (4), 1421-1434.

139. Baugher, B. W.; Churchill, H. O.; Yang, Y.; Jarillo-Herrero, P. *Nano Lett.* **2013**, 13, (9), 4212-4216.

140. Schmidt, H.; Wang, S.; Chu, L.; Toh, M.; Kumar, R.; Zhao, W.; Neto, A. H.; Martin, J.; Adam, S.; Ozyilmaz, B.; Eda, G. *Nano Lett.* **2014**, 14, (4), 1909-1913.

141. Galande, C.; Mohite, A. D.; Naumov, A. V.; Gao, W.; Ci, L.; Ajayan, A.; Gao, H.; Srivastava, A.; Weisman, R. B.; Ajayan, P. M. *Sci. Rep.* **2011**, 1, 85.

142. Rusli; Robertson, J.; Amaratunga, G. A. J. *J. Appl. Phys.* **1996**, 80, (5), 2998.

143. Kozawa, D.; Miyauchi, Y.; Mouri, S.; Matsuda, K. *Phys. Status Solidi C* **2013**,

10, (11), 1600-1603.

144. Matsumoto, Y.; Koinuma, M.; Kim, S. Y.; Watanabe, Y.; Taniguchi, T.; Hatakeyama, K.; Tateishi, H.; Ida, S. *ACS Appl. Mater. Interfaces* **2010**, *2*, (12), 3461-3466.

145. Dresselhaus, M. S.; Jorio, A.; Hofmann, M.; Dresselhaus, G.; Saito, R. *Nano Lett.* **2010**, *10*, (3), 751-758.

146. Cong, C.; Yu, T.; Sato, K.; Shang, J.; Saito, R.; Dresselhaus, G. F.; Dresselhaus, M. S. *ACS nano* **2011**, *5*, (11), 8760-8768.

147. Saito, R.; Grüneis, A.; Samsonidze, G. G.; Brar, V.; Dresselhaus, G.; Dresselhaus, M.; Jorio, A.; Cançado, L.; Fantini, C.; Pimenta, M. *New J. Phys.* **2003**, *5*, (1), 157.

148. Zhang, X.-F.; Shao, X.; Liu, S. *J. Phys. Chem. A* **2012**, *116*, (27), 7308-7313.

149. Toda, Y.; Moriwaki, O.; Nishioka, M.; Arakawa, Y. *Phys. Rev. Lett.* **1999**, *82*, (20), 4114-4117.

150. Norris, D. J.; Bawendi, M. G. *Phys. Rev. B* **1996**, *53*, (24), 338-346.

151. Peng, J.; Gao, W.; Gupta, B. K.; Liu, Z.; Romero-Aburto, R.; Ge, L.; Song, L.; Alemany, L. B.; Zhan, X.; Gao, G. *Nano Lett.* **2012**, *12*, (2), 844-849.

152. Fuyuno, N.; Kozawa, D.; Miyauchi, Y.; Mouri, S.; Kitaura, R.; Shinohara, H.; Yasuda, T.; Komatsu, N.; Matsuda, K. *Adv. Opt. Mater.* **2014**, *2*, (10), 983-989.

153. Zhu, X.; Su, H. *ACS nano* **2014**, *8*, (2), 1284-1289.

154. Johari, P.; Shenoy, V. B. *ACS nano* **2011**, *5*, (9), 7640-7647.

155. Kumar, P. V.; Bernardi, M.; Grossman, J. C. *ACS nano* **2013**, *7*, (2), 1638-1645.

156. Dreyer, D. R.; Park, S.; Bielawski, C. W.; Ruoff, R. S. *Chem. Soc. Rev.* **2010**, *39*, (1), 228-240.

157. Van Duuren, B. L. *Chem. Rev.* **1963**, *63*, (4), 325-354.

158. Thommes, G. A.; Leininger, E. *Talanta* **1960**, *5*, (3), 260-263.

159. Berlman, I. B., *Handbook of fluorescence spectra of aromatic molecules*. Academic Press: New York, U.S., 1971.
160. Martin, R.; Clarke, G. A. *J. Phys. Chem.* **1978**, 82, (1), 81-86.
161. Hosoya, H.; Tanaka, J.; Nagakura, S. *J. Mol. Spectrosc.* **1962**, 8, (1), 257-275.
162. Underberg, W. J.; Schulman, S. G. *Anal. Chim. Acta* **1979**, 105, 311-317.
163. Thommes, G. A.; Leininger, E. *Anal. Chem.* **1958**, 30, (8), 1361-1363.
164. Koinuma, M.; Ogata, C.; Kamei, Y.; Hatakeyama, K.; Tateishi, H.; Watanabe, Y.; Taniguchi, T.; Gezuhara, K.; Hayami, S.; Funatsu, A. *J. Phys. Chem. C* **2012**, 116, (37), 19822-19827.
165. Marzzacco, C. J.; Deckey, G.; Halpern, A. M. *J. Phys. Chem.* **1982**, 86, (25), 4937-4941.
166. Tozuka, Y.; Sasaoka, S.; Nagae, A.; Moribe, K.; Oguchi, T.; Yamamoto, K. *J. Colloid Interface Sci.* **2005**, 291, (2), 471-476.
167. Ofran, M.; Feitelson, J. *Chem. Phys. Lett.* **1973**, 19, (3), 427-431.
168. Szabó, T.; Berkesi, O.; Forgó, P.; Josepovits, K.; Sanakis, Y.; Petridis, D.; Dékány, I. *Chem. Mater.* **2006**, 18, (11), 2740-2749.
169. Cai, W.; Piner, R. D.; Stadermann, F. J.; Park, S.; Shaibat, M. A.; Ishii, Y.; Yang, D.; Velamakanni, A.; An, S. J.; Stoller, M. *Science* **2008**, 321, (5897), 1815-1817.
170. Gan, Z.; Xiong, S.; Wu, X.; Xu, T.; Zhu, X.; Gan, X.; Guo, J.; Shen, J.; Sun, L.; Chu, P. K. *Adv. Opt. Mater.* **2013**, 1, (12), 926-932.
171. McDonald, M. P.; Eltom, A.; Vietmeyer, F.; Thapa, J.; Morozov, Y. V.; Sokolov, D. A.; Hodak, J. H.; Vinodgopal, K.; Kamat, P. V.; Kuno, M. *Nano Lett.* **2013**, 13, (12), 5777-5784.
172. Tsuchiya, T.; Terabe, K.; Aono, M. *Adv. Mater.* **2014**, 26, (7), 1087-1091.
173. Ekiz, O. O.; Urel, M.; Guner, H.; Mizrak, A. K.; Dâna, A. *ACS nano* **2011**, 5, (4), 2475-2482.

174. Gokus, T.; Nair, R.; Bonetti, A.; Bohmler, M.; Lombardo, A.; Novoselov, K.; Geim, A.; Ferrari, A.; Hartschuh, A. *ACS nano* **2009**, 3, (12), 3963-3968.
175. Kozawa, D.; Miyauchi, Y.; Mouri, S.; Matsuda, K. *J. Phys. Chem. Lett.* **2013**, 4, (12), 2035-2040.
176. Thomas, H. R.; Vallés, C.; Young, R. J.; Kinloch, I. A.; Wilson, N. R.; Rourke, J. P. *J. Mater. Chem. C* **2013**, 1, (2), 338.
177. Hossain, M. Z.; Johns, J. E.; Bevan, K. H.; Karmel, H. J.; Liang, Y. T.; Yoshimoto, S.; Mukai, K.; Koitaya, T.; Yoshinobu, J.; Kawai, M.; Lear, A. M.; Kesmodel, L. L.; Tait, S. L.; Hersam, M. C. *Nat. Chem.* **2012**, 4, (4), 305-309.
178. Lakowicz, J. R., *Principles of Fluorescence Spectroscopy*. third ed.; Springer: Berlin, Germany, 2007.
179. Gonze, X.; Beuken, J.-M.; Caracas, R.; Detraux, F.; Fuchs, M.; Rignanese, G.-M.; Sindic, L.; Verstraete, M.; Zerah, G.; Jollet, F. *Comput. Phys. Sci.* **2002**, 25, (3), 478-492.
180. Godby, R.; Needs, R. *Phys. Rev. Lett.* **1989**, 62, (10), 1169.
181. Zhu, X.; Su, H. *J. Phys. Chem. C* **2010**, 114, (41), 17257-17262.
182. Zhu, X.; Su, H. *J. Phys. Chem. A* **2011**, 115, (43), 11998-12003.
183. Siegel, D. A.; Park, C.-H.; Hwang, C.; Deslippe, J.; Fedorov, A. V.; Louie, S. G.; Lanzara, A. *Proc. Natl. Acad. Sci. U. S. A.* **2011**, 108, (28), 11365-11369.
184. Miyazaki, J.; Kinoshita, S. *J. Phys. Soc. Jpn.* **2012**, 81, 074708.
185. Miyazaki, J.; Kinoshita, S. *Phys. Rev. B* **2012**, 86, 035303.
186. Crooker, S. A.; Hollingsworth, J. A.; Tretiak, S.; Klimov, V. I. *Phys. Rev. Lett.* **2002**, 89, 186802.
187. Scholes, G. D.; Andrews, D. L. *Phys. Rev. B* **2005**, 72, 125331.
188. Ruzicka, B. A.; Kumar, N.; Wang, S.; Ping Loh, K.; Zhao, H. *J. Appl. Phys.* **2011**, 109, (8), 084322.
189. Chen, Q.; Zhang, C.; Xue, F.; Zhou, Y.; Li, W.; Wang, Y.; Tu, W.; Zou, Z.;

- Wang, X.; Xiao, M. *Sci. Rep.* **2013**, *3*, 2315.
190. Mukamel, S., *Principles of Nonlinear Optical Spectroscopy*. Oxford University Press: New York, U.K., 1995.
191. Dimiev, A. M.; Alemany, L. B.; Tour, J. M. *ACS nano* **2012**, *7*, (1), 576-588.
192. Bassani, F.; Parravicini, G. P., *Electronic states and optical transitions in solids*. Oxford, U.K., 1975.
193. Zhao, W.; Ghorannevis, Z.; Chu, L.; Toh, M.; Kloc, C.; Tan, P.-H.; Eda, G. *ACS nano* **2013**, *7*, (1), 791-797.
194. Coehoorn, R.; Haas, C.; De Groot, R. *Phys. Rev. B* **1987**, *35*, (12), 6203.
195. Giannozzi, P.; Baroni, S.; Bonini, N.; Calandra, M.; Car, R.; Cavazzoni, C.; Ceresoli, D.; Chiarotti, G. L.; Cococcioni, M.; Dabo, I. *J. Phys.: Condens. Matter* **2009**, *21*, (39), 395502.
196. Perdew, J. P.; Burke, K.; Ernzerhof, M. *Phys. Rev. Lett.* **1996**, *77*, (18), 3865.
197. Monkhorst, H. J.; Pack, J. D. *Phys. Rev. B* **1976**, *13*, (12), 5188-5192.
198. Molina-Sánchez, A.; Wirtz, L. *Phys. Rev. B* **2011**, *84*, (15), 155413.
199. Li, H.; Zhang, Q.; Yap, C. C. R.; Tay, B. K.; Edwin, T. H. T.; Olivier, A.; Baillargeat, D. *Adv. Funct. Mater.* **2012**, *22*, (7), 1385-1390.
200. Wieting, T.; Verble, J. *Phys. Rev. B* **1971**, *3*, (12), 4286-4292.
201. Tongay, S.; Zhou, J.; Ataca, C.; Lo, K.; Matthews, T. S.; Li, J.; Grossman, J. C.; Wu, J. *Nano Lett.* **2012**, *12*, (11), 5576-5580.
202. Zhao, W.; Ghorannevis, Z.; Amara, K. K.; Pang, J. R.; Toh, M.; Zhang, X.; Kloc, C.; Tan, P. H.; Eda, G. *Nanoscale* **2013**, *5*, (20), 9677-9683.
203. Li, Y.; Rao, Y.; Mak, K. F.; You, Y.; Wang, S.; Dean, C. R.; Heinz, T. F. *Nano Lett.* **2013**, *13*, (7), 3329-3333.
204. Jiang, H. *J. Phys. Chem. C* **2012**, *116*, (14), 7664-7671.
205. Zhao, W.; Ribeiro, R. M.; Toh, M.; Carvalho, A.; Kloc, C.; Castro Neto, A. H.; Eda, G. *Nano Lett.* **2013**, *13*, (11), 5627-5634.

206. Beal, A.; Knights, J.; Liang, W. *J. Phys. C: Solid State Phys.* **1972**, *5*, (24), 3540.
207. Hecht, E., *Optics*. Addison-Wesley: 2002.
208. Shi, H.; Yan, R.; Bertolazzi, S.; Brivio, J.; Gao, B.; Kis, A.; Jena, D.; Xing, H. G.; Huang, L. *ACS nano* **2013**, *7*, (2), 1072-1080.
209. Sim, S.; Park, J.; Song, J.-G.; In, C.; Lee, Y.-S.; Kim, H.; Choi, H. *Phys. Rev. B* **2013**, *88*, (7), 075434.
210. Wang, R.; Ruzicka, B. A.; Kumar, N.; Bellus, M. Z.; Chiu, H.-Y.; Zhao, H. *Phys. Rev. B* **2012**, *86*, (4), 045406.
211. Kumar, N.; He, J.; He, D.; Wang, Y.; Zhao, H. *J. Appl. Phys.* **2013**, *113*, (13), 133702.
212. Buscema, M.; Steele, G. A.; van der Zant, H. S. J.; Castellanos-Gomez, A. *Nano Res.* **2014**, *7*, (4), 1-11.
213. Kittel, C., *Quantum Theory of Solids*. Wiley: New York, U.S., 1987.
214. Bockelmann, U. *Phys. Rev. B* **1990**, *42*, (14), 8947-8951.
215. Kaasbjerg, K.; Thygesen, K. S.; Jacobsen, K. W. *Phys. Rev. B* **2012**, *85*, (11), 115317.
216. Nozik, A. J. *Phys. E* **2002**, *14*, (1), 115-120.
217. Saeed, S.; de Jong, E. M.; Dohnalova, K.; Gregorkiewicz, T. *Nat. Commun.* **2014**, *5*, 4665.
218. Pan, D.; Zhang, J.; Li, Z.; Wu, M. *Adv. Mater.* **2010**, *22*, (6), 734-738.
219. van der Zande, A. M.; Huang, P. Y.; Chenet, D. A.; Berkelbach, T. C.; You, Y.; Lee, G.-H.; Heinz, T. F.; Reichman, D. R.; Muller, D. A.; Hone, J. C. *Nat. Mater.* **2013**, *12*, (6), 554-561.
220. Zhang, W.; Chuu, C. P.; Huang, J. K.; Chen, C. H.; Tsai, M. L.; Chang, Y. H.; Liang, C. T.; Chen, Y. Z.; Chueh, Y. L.; He, J. H.; Chou, M. Y.; Li, L. J. *Sci. Rep.* **2014**, *4*, 3826.

221. Sobhani, A.; Lauchner, A.; Najmaei, S.; Ayala-Orozco, C.; Wen, F.; Lou, J.; Halas, N. J. *Appl. Phys. Lett.* **2014**, 104, (3), 031112.
222. Sie, E. J.; Lee, Y.-H.; Frenzel, A. J.; Kong, J.; Gedik, N. *arXiv preprint arXiv:1312.2918* **2013**.
223. Lagarde, D.; Bouet, L.; Marie, X.; Zhu, C.; Liu, B.; Amand, T.; Tan, P.; Urbaszek, B. *Phys. Rev. Lett.* **2014**, 112, (4), 047401.
224. Kumar, N.; Cui, Q.; Ceballos, F.; He, D.; Wang, Y.; Zhao, H. *Phys. Rev. B* **2014**, 89, (12), 125427.
225. Korn, T.; Heydrich, S.; Hirmer, M.; Schmutzler, J.; Schüller, C. *Appl. Phys. Lett.* **2011**, 99, (10), 102109.
226. Mai, C.; Barrette, A.; Yu, Y.; Semenov, Y. G.; Kim, K. W.; Cao, L.; Gundogdu, K. *Nano Lett.* **2014**, 14, (1), 202-206.

Scientific contributions

The name of the author is underlined.

Peer-reviewed articles

1. Feijiu Wang, Daichi Kozawa, Yuhei Miyauchi, Kazushi Hiraoka, Shinichiro Mouri, Yutaka Ohno, and Kazunari Matsuda, “Considerably improved photovoltaic performance of carbon nanotube-based solar cells using metal oxide layers”, *Nature Communications* **2015**, 6, 6305.
2. Daichi Kozawa, Rajeev Kumar, Alexandra Carvalho, Kiran Kumar Amara, Weijie Zhao, Shunfeng Wang, Minglin Toh, Ricardo M. Ribeiro, Antonio Castro Neto, Kazunari Matsuda, and Goki Eda, “Photocarrier relaxation pathway in two-dimensional semiconducting transition metal dichalcogenides”, *Nature Communications* **2014**, 5, 4543.
3. Tetsuo Sakka, Daichi Kozawa, Kiyoto Tsuchiya, Nao Sugiman, Gisle Øye, Kazuhiro Fukami, Naoya Nishi, and Yukio H. Ogata, “Two-dimensional array of particles originating from dipole–dipole interaction as evidenced by potential curve measurements at vertical oil/water interfaces”, *Physical Chemistry Chemical Physics* **2014**, 16, (32), 16976-16984.
4. Naoto Fuyuno, Daichi Kozawa, Yuhei Miyauchi, Shinichiro Mouri, Ryo Kitaura, Hisanori Shinohara, Toku Yasuda, Naoki Komatsu, and Kazunari Matsuda, “Drastic change in photoluminescence properties of graphene quantum dots by chromatographic separation”, *Advanced Optical Materials* **2014**, 2, (10), 983-989.
5. Daichi Kozawa, Yuhei Miyauchi, Shinichiro Mouri, Masao Ichida, and Kazunari Matsuda, “Excitonic photoluminescence from nanodisc states in graphene oxides”, *The Journal of Physical Chemistry Letters* **2014**, 5, (10), 1754-1759.
6. Feijiu Wang, Daichi Kozawa, Yuhei Miyauchi, Kazushi Hiraoka, Shinichiro Mouri,

- Yutaka Ohno, and Kazunari Matsuda, “Fabrication of single-walled carbon nanotube/Si heterojunction solar cell with high photovoltaic conversion efficiency and stability”, *ACS Photonics* **2014**, 1, (4), 360-364.
7. Daichi Kozawa, Yuhei Miyauchi, Shinichiro Mouri, and Kazunari Matsuda, “Changing photoluminescence spectra of graphene oxide by centrifugation treatments”, *physica status solidi (c)* **10**, 11, 1600-1603 (2013).
 8. Feijiu Wang, Daichi Kozawa, Yuhei Miyauchi, Kazushi Hiraoka, Shinichiro Mouri, and Kazunari Matsuda, “Enhancement mechanism of the photovoltaic conversion efficiency of single-walled carbon nanotube/Si solar cells by HNO₃ doping”, *Applied Physics Express* **2013**, 6, (10), 102301.
 9. Daichi Kozawa, Yuhei Miyauchi, Shinichiro Mouri, and Kazunari Matsuda, “Exploring the origin of blue and ultraviolet fluorescence in graphene oxide”, *The Journal of Physical Chemistry Letters* **2013**, 4, (12), 2035-2040.
 10. Daichi Kozawa, Kazushi Hiraoka, Yuhei Miyauchi, Shinichiro Mouri, and Kazunari Matsuda, “Analysis of the photovoltaic properties of single-walled carbon nanotube/silicon heterojunction solar cells”, *Applied Physics Express* **2012**, 5, (4), 042304.

Review article

1. 小澤大知, 松田一成, “グラフェンナノリボンを用いた赤外光領域におけるプラズモニクス”, *分光研究 トピックス* **2013**, 62, (4) 183-184.

Conference contributions

International conference

1. Daichi Kozawa, Rajeev Kumar, Alexandra Carvalho, Kiran Kumar Amara, Weijie

- Zhao, Shunfeng Wang, Minglin Toh, Ricardo M. Ribeiro, A. H. Castro Neto, Kazunari Matsuda, Goki Eda, “Strong Light-matter Interaction and Photocarrier Relaxation in Two-dimensional Transition Metal Dichalcogenides”, The 1st international conference on two-dimensional layered materials, B-O-25, Zhejiang Hotel, Hangzhou, China, 15 Oct, 2014 (Oral).
2. Daichi Kozawa, Yuhei Miyauchi, Shinichiro Mouri, Kazunari Matsuda, “Origin of Photoluminescence in Graphene Oxides Studied by Static and Time-resolved Photoluminescence Spectroscopy”, The 40th International Symposium on Compound Semiconductors, TuB2-3, Kobe Convention Center, Kobe, Japan, 19-23 May, 2013 (Oral).
 3. Daichi Kozawa, Yuhei Miyauchi, Shinichiro Mouri, Kazunari Matsuda, “Size-dependent photoluminescence properties of graphene oxides”, International Winterschool on Electronic Properties of Novel Materials 2013, the Hotel Sonnalp, Kirchberg in Tirol, Austria, 2-9 Mar, 2013 (Poster).
 4. Daichi Kozawa, Yuhei Miyauchi, Shinichiro Mouri, Kazunari Matsuda, “Photovoltaic Properties of Single-Walled Carbon Nanotube/Silicon Heterojunction Solar Cells”, 2nd Japanese-German Workshop on Energy Materials Science, The Karlsruhe Institute of Technology, Karlsruhe, Germany, 12 Dec, 2012 (Oral).

Local conference

1. 小澤大知, Rajeev Kumar, Alexandra Carvalho, Kiran Kumar Amara, Weijie Zhao, Shunfeng Wang, Minglin Toh, Ricardo M. Ribeiro, A. H. Castro Neto, 松田一成, Goki Eda, “原子層遷移金属ダイカルコゲナイドにおける巨大光吸収と光キャリア緩和機構”, 第25回光物性研究会, III B-107, 神戸大学 百年記念会館, 兵庫県神戸市, 2014年12月13日(ポスター).
2. 小澤大知, Alexandra Carvalho, Rajeev Sharma Kumar, Amara Kiran Kumar,

- Weijie Zhao, Minglin Toh, A. H. Castro Neto, 松田一成, 江田剛輝, “遷移金属ダイカルコゲナイドのバンドネスティングの効果”, 日本物理学会第 69 回年次大会, 29pAK-6, 東海大学 湘南キャンパス, 神奈川県平塚市, 2014 年 3 月 29 日 (口頭).
3. 小澤大知, 宮内雄平, 毛利真一郎, 市田正夫, 松田一成, “Mechanisms of Near-Infrared Photoluminescence from Graphene Oxides”, 第 46 回 フラールン・ナノチューブ・グラフェン 総合シンポジウム, 2P-47, 東京大学 伊藤国際学術研究センター 伊藤謝恩ホール, 東京都文京区, 2014 年 3 月 4 日(ポスター).
 4. Daichi Kozawa, Rajeev Kumar, Alexandra Carvalho, Amara Kiran Kumar, Weijie Zhao, Minglin Toh, Ricardo M. Ribeiro, A. H. Castro Neto, Kazunari Matsuda, and Goki Eda, “Effect of Band Nesting on Optical Properties in Two-dimensional Transition Metal Dichalcogenides”, 第 46 回 フラールン・ナノチューブ・グラフェン 総合シンポジウム, 1-8, 東京大学 伊藤国際学術研究センター 伊藤謝恩ホール, 東京都文京区, 2014 年 3 月 3 日 (口頭).
 5. 小澤大知, 宮内雄平, 毛利真一郎, 市田正夫, 松田一成, “酸化グラフェンの近赤外発光機構”, 応用物理学会関西支部 平成 25 年度第 3 回講演会, P-029, 大阪大学 吹田キャンパス フォトニクスセンター, 大阪府吹田市, 2014 年 2 月 28 日(ポスター).
 6. 小澤大知, 宮内雄平, 毛利真一郎, 松田一成, “酸化グラフェンの吸収・発光特性とその起源”, 日本物理学会 第 68 回年次大会, 29aXP-9, 広島大学 東広島キャンパス, 広島県東広島市, 2013 年 3 月 29 日 (口頭).
 7. 小澤大知, 宮内雄平, 毛利真一郎, 松田一成, “酸化グラフェンの層数に依存した発光特性”, 第 23 回光物性研究会, III B100, 大阪市立大学 杉本キャンパス, 大阪府大阪市, 2012 年 12 月 8 日 (ポスター).
 8. 小澤大知, 市田正夫, 宮内雄平, 毛利真一郎, 松田一成, “酸化グラフェンにおける共鳴励起発光と時間分解発光分光”, 日本物理学会 2012 年秋季大

- 会、19aEC-11、横浜国立大学 常盤台キャンパス、神奈川県横浜市、2012年9月19日 (口頭).
9. 小澤大知、市田正夫、宮内雄平、毛利真一郎、松田一成, “酸化グラフェンの発光スペクトル構造の起源”、2012年 秋季 第73回応用物理学会学術講演会、12p-C2-13、愛媛大学 城北地区、愛媛県松山市、2012年9月12日 (口頭).
 10. 小澤大知、平岡和志、宮内雄平、毛利真一郎、松田一成, “Photovoltaic Properties of Single-Walled Carbon Nanotube/Silicon Heterojunction Solar Cells”、第43回フラーレン・ナノチューブ・グラフェン総合シンポジウム、2P-20、東北大学 百周年記念会館 川内萩ホール、宮城県仙台市、2012年9月6日 (ポスター).
 11. 小澤大知、平岡和志、宮内雄平、毛利真一郎、松田一成、”単層カーボンナノチューブ-シリコンヘテロ接合太陽電池の光電変換機構の解明”、2012年 春季 第59回応用物理学関係連合講演会、18a-B2-1、早稲田大学、東京都新宿区、2012年3月18日 (口頭).

Awards

1. President Award, Kyoto University, March 16, 2015.
2. Poster Award (第25回光物性研究会 奨励賞) “原子層遷移金属ダイカルコゲナイドにおける巨大光吸収と光キャリア緩和機構”, 光物性研究会, December 13, 2014.
3. Poster Award (第46回フラーレン・ナノチューブ・グラフェン総合シンポジウム 若手奨励賞) “Mechanisms of Near-Infrared Photoluminescence from Graphene Oxides”, The 46th Fullerenes-Nanotubes-Graphene General Symposium, The Fullerenes, Nanotubes and Graphene Research Society, March 4, 2014.
4. Student Award (平成25年度 京都大学エネルギー理工学研究所 学生賞) “酸

化グラフェンの光学特性に関する研究”, Institute of Advanced Energy, Kyoto University, March 7, 2014.

Appendix

Dynamics of photocarrier in MoS₂

Table A Summary of previously reported lifetime for various processes for MoS₂. A part of these lifetimes are considered for the interpretation of the excitation and relaxation pathways.

Ref.	Process	Life time	Material	Configuration
222	Hot exciton gas during the cooling process	1-2 ps	CVD-grown MoS ₂ on sapphire	Transient absorption spectroscopy with 3.16 eV excitation at 10 K by pump-probe (measuring the change in reflectivity or transmittance)
	Formation of biexciton	2 ps		
	All excitons have relaxed to the lowest excited state (A exciton)	4 ps		
223	Polarization lifetime	4.5 ps	Exfoliated monolayer MoS ₂ on SiO ₂ /Si	Time-resolved PL spectroscopy with quasi-resonant excitation of the A-exciton transitions at 4 K-300 K
	PL lifetime (non-radiative recombination)	5 ps		Time-resolved PL exciting highly non-resonantly allowing both free carrier and exciton

	of excitons)			generation at 4 K
	Localized exciton emission decay	125 ps		Time-resolved PL spectroscopy with quasi-resonant excitation of the A-exciton transitions at 4 K
211	Intervalley (K- Γ) transfer time	0.35 ps	Bulk MoS ₂ crystal	Transient absorption spectroscopy pumping at the B or C (2.23 eV), probing at A (1.88 eV) peak at room temperature (measuring the change in reflectivity)
	Energy relaxation time of hot carriers	50 ps		
	Carrier lifetime	180 ps \pm 20ps		
209	Exciton-exciton scattering	500 fs	4-5 L MoS ₂ synthesized with a hot-wall furnace type system	Transient absorption spectroscopy pumping at B (2.04 eV) or C (3.10 eV), probing at A or B peak (1.70-2.21 eV) at room temperature (measuring the change in transmittance)
208	Defect assisted scattering from C to A	< 500 fs	Si ₃ N ₄ substrate-suspended	Transient absorption spectroscopy pumping at 3.2 eV at room temperature (measuring the change in transmittance)
	Carrier-phonon scattering from A to GS	80 ps	monolayer MoS ₂	

	Relaxation to trap states from A	2-4 ps		
	Direct recombination from A to GS	800 ps		
	Carrier-carrier scattering from C to A	2 ps	Bulk MoS ₂ crystal ~150 layers	
	Carrier-phonon scattering from C to A	20 ps		
	Intervalley scattering from A to indirect states	2.6 ns		
	Indirect recombination to GS	> 2.6 ns		
224	Exciton-exciton annihilation	< 50 ps	Exfoliated monolayer	Transient absorption spectroscopy pumping at 1.65 eV and probing at the A (1.51-1.57 eV) peak at room temperature (measuring the change in reflectivity)
	Exciton lifetime	> 150 ps	MoSe ₂ on SiO ₂ /Si	
	Indirect bandgap transition (no exciton-exciton)	300-400 ps	Bulk monolayer	

	annihilation)			
225	Photocarrier recombination	5 ps	Exfoliated monolayer	Time-resolved PL spectroscopy at 4.5 K
	Exciton-phonon scattering	70 ps	MoS ₂ on SiO ₂ /Si	Time-resolved PL spectroscopy at room temperature
226	Valley polarization decay time	10 ps	CVD-grown monolayer MoS ₂	Transient absorption spectroscopy pumping at 1.88 eV and probing continuum pulses at 74 K (measuring the change in transmittance)
210	Carrier lifetime	100 ± 10 ps	Exfoliated few-layer MoS ₂ on SiO ₂ /Si	Transient absorption spectroscopy pumping at the C (3.18 eV) and probing at A (1.88 eV) peak at room temperature (measuring the change in reflectivity)
226	Phonon-related process	7.1 ps, 61.3 ps	Exfoliated monolayer MoS ₂ on SiO ₂ /Si	Transient absorption spectroscopy pumping at 1.96 eV and probing at 1.91 eV at 78 K (measuring the change in reflectivity)
51	Exciton lifetime	> 50 ps	Exfoliated MoS ₂ on hBN	Estimated from steady-state PL and quantum yields exciting with 1.96 eV continuous wave at 14 K
	Hole valley-spin	> 1 ns		Polarization-resolved PL

	lifetime			exciting with 1.96 eV
	Hole spin lifetime	Few hundred s of fs	Bilayer MoS ₂ on hBN	continuous wave at 14 K